



University of Dundee

Mitotic CDK Promotes Replisome Disassembly, Fork Breakage, and Complex DNA Rearrangements

Deng, Lin; Wu, R. Alex; Sonnevile, Remi; Kochenova, Olga V.; Labib, Karim; Pellman, David

Published in:
Molecular Cell

DOI:
[10.1016/j.molcel.2018.12.021](https://doi.org/10.1016/j.molcel.2018.12.021)

Publication date:
2019

Document Version
Peer reviewed version

[Link to publication in Discovery Research Portal](#)

Citation for published version (APA):

Deng, L., Wu, R. A., Sonnevile, R., Kochenova, O. V., Labib, K., Pellman, D., & Walter, J. C. (2019). Mitotic CDK Promotes Replisome Disassembly, Fork Breakage, and Complex DNA Rearrangements. *Molecular Cell*, 73(5), 915-929.e6. <https://doi.org/10.1016/j.molcel.2018.12.021>

General rights

Copyright and moral rights for the publications made accessible in Discovery Research Portal are retained by the authors and/or other copyright owners and it is a condition of accessing publications that users recognise and abide by the legal requirements associated with these rights.

- Users may download and print one copy of any publication from Discovery Research Portal for the purpose of private study or research.
- You may not further distribute the material or use it for any profit-making activity or commercial gain.
- You may freely distribute the URL identifying the publication in the public portal.

Take down policy

If you believe that this document breaches copyright please contact us providing details, and we will remove access to the work immediately and investigate your claim.

1
2
3
4
5
6
7
8
9
10
11
12
13
14
15
16
17
18
19
20
21
22
23

Mitotic CDK promotes replisome disassembly, fork breakage, and complex DNA rearrangements

Lin Deng^{1,2,3}, R. Alex. Wu³, Remi Sonnevile⁴, Olga V. Kochenova³, Karim Labib⁴,
David Pellman^{1,2,5,6,7}, and Johannes C. Walter^{3,6,7,8}

¹Department of Pediatric Oncology, Dana-Farber Cancer Institute, Boston, MA 02215, USA

²Department of Cell Biology, Harvard Medical School, Boston, MA 02115, USA

³Department of Biological Chemistry and Molecular Pharmacology, Harvard Medical School,
Boston, MA 02115, USA

⁴MRC Protein Phosphorylation and Ubiquitylation Unit, Sir James Black Centre, School of Life
Sciences, University of Dundee, Dow Street, Dundee DD1 5EH, UK

⁵Broad Institute of MIT and Harvard, Cambridge, MA 02142, USA

⁶Howard Hughes Medical Institute, Boston, MA 02115, USA

⁷These authors contributed equally to this work

⁸Lead Contact

*Correspondence: David_Pellman@dfci.harvard.edu (D.P.),
Johannes_Walter@hms.harvard.edu (J.C.W.)

24 **Summary**

25 DNA replication errors generate complex chromosomal rearrangements and thereby
26 contribute to tumorigenesis and other human diseases. One mechanism that triggers
27 these errors is mitotic entry before the completion of DNA replication. To address how
28 mitosis impacts DNA replication, we used *Xenopus* egg extracts. When mitotic CDK
29 (Cyclin B1-CDK1) is used to drive these extracts into a mitotic state, the replicative
30 CMG (CDC45/MCM2-7/GINS) helicase undergoes ubiquitylation on its MCM7 subunit,
31 dependent on the E3 ubiquitin ligase TRAIP. Whether replisomes have stalled or
32 undergone termination, CMG ubiquitylation is followed by its extraction from chromatin
33 by the CDC48/p97 ATPase. TRAIP-dependent CMG unloading during mitosis is also
34 seen in *C. elegans* early embryos. At stalled forks, CMG removal results in fork
35 breakage and end joining events involving deletions and templated insertions. Our
36 results identify a novel pathway of global replisome disassembly in mitosis that can
37 trigger replication fork collapse and DNA rearrangements.

38

39 **HIGHLIGHTS**

- 40 1. Replication fork collapse is triggered by mitotic CDK-dependent CMG unloading
- 41 2. Unloading of CMGs in mitosis involves the E3 ubiquitin ligase TRAIP and the p97
42 ATPase
- 43 3. New model for the mitotic processing of stalled forks that enables high-fidelity
44 chromosome segregation
- 45 4. New model for the generation of complex chromosome rearrangements

46 **INTRODUCTION**

47 Genome evolution occurs through the gradual accrual of genetic changes or in a
48 saltatory manner, with bursts of chromosomal alterations originating from single
49 catastrophic events (Holland and Cleveland, 2012; Leibowitz et al., 2015; Liu et al.,
50 2011; Stephens et al., 2011). Many chromosomal alterations can be traced to DNA
51 breaks that arise during DNA replication (Hills and Diffley, 2014; Mankouri et al., 2013;
52 Techer et al., 2017). However, there is an ongoing debate about when and how
53 replication fork breakage is triggered (Toledo et al., 2017).

54 In normal cells, multiple cell cycle regulatory controls and error correction
55 mechanisms prevent DNA replication errors (Hills and Diffley, 2014). Cells prepare for
56 DNA replication in the G1 phase of the cell cycle, when pairs of MCM2-7 ATPases are
57 recruited to each origin (“licensing”). In S phase, cyclin-dependent kinase (CDK)
58 promotes the association of CDC45 and GINS with MCM2-7, leading to formation of the
59 replicative CMG helicase complex (CDC45-MCM2-7-GINS) (“initiation”). CMG
60 unwinding of the origin nucleates the assembly of two DNA replication forks that travel
61 away from the origin, copying DNA as they go (“elongation”). When converging forks
62 from adjacent origins meet, the replisome is disassembled (“termination”). Replisome
63 disassembly during S phase in metazoa requires the E3 ubiquitin ligase, CRL2^{Lrr1},
64 which ubiquitylates the MCM7 subunit of CMG, leading to CMG’s extraction from
65 chromatin by the p97 ATPase (Dewar et al., 2017; Sonnevile et al., 2017). In the
66 absence of CRL2^{Lrr1}, CMGs persist on chromatin until mitosis, but are then removed by
67 a secondary, p97-dependent pathway that is controlled by an unknown E3 ubiquitin
68 ligase (Sonneville et al., 2017). Re-replication is inhibited because *de novo* licensing of
69 origins is suppressed in the S and G2 phases of the cell cycle. Thus, faithful DNA

70 replication requires the seamless integration of replication licensing, initiation,
71 elongation, and termination. Errors in the process are detected by the DNA damage
72 response, which activates repair mechanisms and prevents entry into mitosis in the
73 setting of incomplete or abnormal replication.

74 DNA replication forks become stressed in a variety of circumstances, including
75 the activation of oncogenes, collision with DNA lesions and other obstacles, and
76 nucleotide starvation (Cortez, 2015; Hills and Diffley, 2014; Saldivar et al., 2017).
77 Replication stress, especially when combined with inhibition of checkpoint kinases, can
78 cause replication fork “collapse”, an irreversible state from which replication cannot be
79 restarted (Cortez, 2015; Hills and Diffley, 2014; Pasero and Vindigni, 2017; Saldivar et
80 al., 2017; Toledo et al., 2017). Despite its central importance to the maintenance of
81 genome stability, much remains to be learned about the mechanisms leading to
82 replication fork collapse and the relationship between fork collapse and breakage.
83 Whether “fork collapse” occurs through multiple independent mechanisms or whether
84 different insults converge on a single irreversible event is not clear. Numerous
85 experiments indicated that fork collapse involves replisome disassembly—an appealing
86 mechanism to explain the irreversibility of “collapse” (Cortez, 2015). However, these
87 studies did not establish a causal relationship between replisome disassembly and
88 collapse. Moreover, some experiments suggest that fork collapse may not involve
89 replisome disassembly (De Piccoli et al., 2012; Dungrawala et al., 2015).

90 Replication fork collapse is strongly enhanced by inhibition of the checkpoint
91 kinase ataxia telangiectasia and RAD3 related (ATR), a phenomenon for which there
92 are multiple proposed mechanisms (Toledo et al., 2017). ATR may stabilize stressed

93 forks through the phosphorylation of specific proteins at the fork (e.g. SMARCAL1,
94 WRN). However, the available evidence suggests that these phosphorylation events are
95 not sufficient to explain ATR-mediated fork stabilization (Ammazzalorso et al., 2010;
96 Couch et al., 2013). A further possibility is that excessive origin firing upon ATR
97 inhibition leads to exhaustion of the nuclear pool of RPA, followed by fork breakage and
98 replisome collapse (Toledo et al., 2013). Finally, ATR might prevent fork collapse by
99 restraining the activation of mitotic kinases such as CDK1 and PLK1 until the
100 completion of replication (Ragland et al., 2013; Saldivar et al., 2018). Mitotic kinases
101 induce fork breakage by promoting the assembly of a MUS81-containing nuclease
102 complex (Duda et al., 2016) or by triggering nuclear envelope breakdown, exposes
103 replication forks to the normally cytoplasmic GEN1 nuclease (West and Chan, 2018). A
104 key role for ATR in restraining mitotic kinases is underscored by recent studies. First,
105 the lethality of ATR inhibition in mammals can be overcome by suppressing Cyclin B-
106 CDK1 activity (Ruiz et al., 2016). Second, even in the absence of exogenous stress,
107 ATR suppresses genome instability by preventing premature accumulation of Cyclin B-
108 CDK1 activity in S phase (Saldivar et al., 2018). Despite this progress, the molecular
109 basis of replication fork collapse and how this process is regulated by ATR remain
110 incompletely understood.

111 Although replication fork breakage is generally viewed as a source of gross
112 chromosomal rearrangements, there are circumstances in which breakage may
113 preserve genome integrity (Bhowmick and Hickson, 2017). A prominent example
114 involves common fragile sites (CFS), which are among the most frequently rearranged
115 genomic loci in cancer genomes (Glover et al., 2017). CFS are difficult to replicate

116 because they either contain large genes with long transcripts and/or have few origins of
117 replication (Glover et al., 2017). Common fragile site “expression,” the appearance of
118 cytologically visible breaks and gaps, is promoted by low doses of aphidicolin because
119 this drug delays duplication of these already late-replicating loci. Unreplicated DNA at
120 CFS forms ultrafine DNA bridges between anaphase chromosomes (Baumann et al.,
121 2007; Chan et al., 2007), and severance of these bridges by MUS81 is thought to allow
122 chromosome segregation. Aberrant processing of expressed CFS leads to the formation
123 of “53BP1 bodies” (Naim et al., 2013; Ying et al., 2013), structures thought to protect
124 damaged DNA in the next interphase (Harrigan et al., 2011; Lukas et al., 2011).
125 Collectively, the data suggest that when cells enter mitosis with incompletely replicated
126 DNA, MUS81 breakage of stalled replication forks enables chromosome segregation.
127 However, random breakage of the fork would yield deleterious outcomes such as the
128 generation of acentric or iso-chromosomes. So far, no mechanism has emerged that
129 explains how such outcomes are avoided.

130 Although breakage of a few stressed forks may be be beneficial, concurrent
131 breakage of many forks generates catastrophic chromosomal rearrangements. Several
132 lines of evidence implicate mitotic entry as one potential cause of extensive fork
133 breakage. Cell fusion experiments (Johnson and Rao, 1970) and experiments on cells
134 with micronuclei (Kato and Sandberg, 1968) showed that S phase chromosomes
135 undergo “pulverization” upon exposure to mitotic cytoplasm. Although there was early
136 disagreement about whether chromosome pulverization reflects discontinuous
137 condensation or actual DNA breakage (Rao et al., 1982), recent work indicates that
138 fragmentation does occur. First, premature mitotic entry triggered by inhibition of the

139 WEE1 kinase causes extensive fork breakage in a manner that depends on the
140 formation of an active MUS81 complex (Dominguez-Kelly et al., 2011; Duda et al.,
141 2016). Second, chromothripsis, a mutational process involving extensive chromosome
142 fragmentation and rearrangement, may involve entry into mitosis of micronuclei
143 undergoing DNA replication (Crasta et al., 2012; Leibowitz et al., 2015). Extensive fork
144 breakage during mitosis is especially problematic as both homologous recombination
145 and classical non-homologous end joining are suppressed at this stage of the cell cycle
146 (Hustedt and Durocher, 2016). In summary, it has become apparent that genome
147 instability in a variety of contexts is linked to mitotic replication fork breakage. However,
148 why forks are so fragile in mitosis is incompletely understood.

149 Here, we used *Xenopus* egg extracts to explore the relationship between DNA
150 replication and mitosis. We find that in egg extracts supplemented with the mitotic
151 kinase Cyclin B1-CDK1, the CMG helicase is ubiquitylated on its MCM7 subunit.
152 Ubiquitylation requires the RING E3 ubiquitin ligase TRAIP, which is mutated in
153 primordial dwarfism. Ubiquitylated CMG is subsequently extracted from chromatin by
154 the CDC48/p97 ATPase. TRAIP-dependent CMG ubiquitylation and unloading is
155 observed at stalled replisomes and replisomes that have undergone termination,
156 indicating that TRAIP removes all CMGs from chromatin, regardless of their
157 configuration on DNA. At stalled forks, CMG unloading leads to fork breakage and end
158 joining events that likely involve DNA polymerase θ (Pol θ). Unlike Cyclin B1-CDK1
159 treatment, ATR inhibition does not lead to fork breakage. Together, our results identify
160 TRAIP-dependent replisome disassembly as a crucial step in mitotic replication fork
161 collapse and breakage. We propose that breakage of a few converging forks (e.g. at

162 CFS) that have failed to complete DNA synthesis before mitosis helps to maintain
163 chromosome integrity whereas breakage of many forks (e.g. in micronuclei) leads to
164 catastrophic genomic instability.

165

166

167 **RESULTS**

168 **Mitotic CDK triggers aberrant processing of stressed DNA replication forks**

169 To examine the effect of mitotic CDK on DNA replication and fork stability, we used
170 *Xenopus* egg extracts, which can recapitulate S phase or mitosis. For S phase, plasmid
171 DNA was first incubated in a high-speed supernatant (HSS) of *Xenopus* egg lysate.
172 HSS promotes the assembly onto DNA of pre-replication complexes (pre-RCs)
173 containing double hexamers of the MCM2-7 ATPase (Figure 1A). The subsequent
174 addition of a nucleoplasmic extract (NPE) leads to the association of CDC45 and GINS
175 with each MCM2-7 hexamer to form two active CMG DNA helicases, which unwind
176 DNA, promoting a single, complete round of DNA replication, manifested as the
177 appearance of supercoiled (SC) daughter molecules (Figure 1B, lanes 1-6) (Walter et
178 al., 1998). To achieve replication in a mitotic state, we added Cyclin B1-CDK1 (B1-
179 CDK1) after pre-RC formation because this kinase inhibits licensing (Hendrickson et al.,
180 1996; Prokhorova et al., 2003)(Figure 1A). We confirmed that B1-CDK1 induced
181 chromosome condensation (Figures S1A-S1C) and condensin recruitment (Figures
182 S1D-E). As we showed previously (Prokhorova et al., 2003), B1-CDK1 increased the
183 rate of DNA replication in NPE (Figure 1B, compare lanes 1-6 and 13-18), due in part to
184 increased origin firing (Figure S1F). However, in the absence of other perturbations, all

185 replication products were open circular or supercoiled species (Figure 1B, lanes 13-18),
186 indicating that B1-CDK1-induced chromatin condensation does not cause aberrant DNA
187 replication.

188 Given the evidence that stressed DNA replication forks undergo breakage during
189 mitosis (e.g. at common fragile sites, see introduction), we added a low concentration of
190 the replicative DNA polymerase inhibitor aphidicolin (APH; 2.2 μ M) to slow fork
191 progression (Figure 1B, lanes 7-12). Interestingly, the combination of B1-CDK1 and
192 APH (Figure 1B, lanes 19-24) led to the appearance of a new replication product that
193 migrated at the very top of the gel. This aberrant replication product (ARP) comprised
194 ~6% of total replication for a 3 kb plasmid and up to 30% for a 9 kb plasmid (data not
195 shown), presumably because the larger plasmid hosts more replication forks. ARPs
196 recovered from extract were not resolved by Topoisomerase I or Topoisomerase II
197 treatment, indicating they are not plasmid topoisomers (data not shown). Thus, in the
198 presence of replication stress, mitotic CDK induces aberrant DNA replication.

199 To examine the effect of B1-CDK1 on replication forks that have stalled at a
200 defined location, we replicated a plasmid containing an array of 48 *lacO* sites (*p[lacO₄₈]*)
201 bound by the *lac* repressor (LacR) (Figure 1C). As expected (Dewar et al., 2015),
202 replication forks stalled at the outer edges of the LacR array, generating a “theta” (θ)
203 structure (Figures 1C and 1D, lanes 11-15). In the presence of B1-CDK1, the theta
204 molecules disappeared and ARPs accumulated (Figure 1D, lanes 16-20). ARPs were
205 not generated when LacR-mediated fork stalling was prevented with IPTG (Figure 1E),
206 or in the presence of the CDK1 inhibitor (CDK1-i) RO-3306 (Figure S1G). Furthermore,
207 addition of Cyclin E-CDK2 or Cyclin A2 (which preferentially associates with

208 endogenous CDK1; (Strausfeld et al., 1996)), did not strongly induce ARPs, although
209 their addition accelerated DNA replication as expected (Figure S1H). Second, we
210 induced replication fork stalling with covalent DNA-protein crosslinks (DPCs). We
211 replicated a plasmid substrate (pDPC), which contains two site-specific DPCs on each
212 leading strand template (Figure 1F). As expected (Duxin et al., 2014), in the absence of
213 B1-CDK1, replication of pDPC first yielded theta structures when forks transiently
214 paused at the DPC. Plasmids then resolved into open circular (OC) species that
215 persisted due to slow translesion synthesis past the peptide adduct generated by DPC
216 proteolysis (Figure 1F, upper arrow and Figure 1G, lanes 13-18). In the presence of B1-
217 CDK1, we again observed a substantial accumulation of ARPs (Figure 1G, lanes 19-
218 24). In summary, mitotic CDK caused aberrant processing of replication forks stalled by
219 aphidicolin, non-covalent nucleoprotein complexes, and DPCs.

220

221 **Mitotic processing of stalled replication forks leads to complex chromosomal**
222 **rearrangements**

223 To determine the structure of mitotic ARPs, we replicated the 4.6 kb LacR plasmid in
224 the presence and absence of B1-CDK1 and digested the replication products with AlwNI
225 and AflII, which cuts the plasmid into a 1.9 kb fragment and a 2.7 kb fragment
226 encompassing the *lacO* repeats (Figure 2A). In the absence of B1-CDK1, fully
227 replicated 1.9 kb fragments quickly accumulated, whereas the rest of the plasmid
228 migrated as a double-Y structure that gradually increased in size due to slow
229 progression of forks through the LacR array (Figure 2B, middle panel, lanes 1-7 and
230 Figure 2C, “Buffer”; (Dewar et al., 2015)). In the presence of B1-CDK1, the 1.9 kb

231 fragment again accumulated quickly and persisted, demonstrating that this *lacO*-free
232 region was replicated efficiently (Figure 2B, middle panel, lanes 8-14). However, the
233 double-Y structure containing the *lacO* array rapidly disappeared. Thus, in the presence
234 of B1-CDK1, aberrant DNA processing occurs specifically on molecules containing
235 stalled forks.

236 When the replication products were digested only with AlwNI, we observed B1-
237 CDK1-dependent disappearance of the now larger double-Y structure (Figure 2B,
238 bottom panel, lanes 8-14). In addition, we detected a new series of species migrating
239 between ~3 and ~4 kb (Figure 2B, bottom panel; smear). We hypothesized that when
240 replication forks enter the array and slow down or stall, B1-CDK1 promotes their
241 collapse and breakage. The resulting double-strand breaks (DSBs) subsequently
242 undergo joining with DSBs from broken forks on other plasmids, generating ARPs
243 (Figures 2C, “B1-CDK1” and S2A). If replication forks collapse at the outer edges of the
244 array, the size of the end joining product after AlwNI digestion is close to 3.1 kb
245 because most of the 1.5 kb *lacO* array is lost; collapse further into to the array
246 generates larger products, accounting for the 3-4 kb range of products observed (Figure
247 S2B). To test this hypothesis, the 3-4 kb species were cloned and sequenced using
248 primers immediately flanking the *lacO* array (Figure S2C). In contrast to control clones
249 (generated from replication in the absence of LacR), all of which contained 48 *lacO*
250 repeats, the 24 clones from the 3-4 kb smear contained fewer than 48 *lacO* repeats
251 (Figure 2D, products a-n). This result confirms that replication forks collapsed within the
252 *lacO* array and then underwent end joining with loss of *lacO* repeats. Seventeen of
253 these products (a-g) involved only deletions of the *lacO* repeats. This suggests that the

254 deletions might occur via single strand annealing (SSA) (Bhargava et al., 2016), which
255 generates deletions between homologous sequences. The remaining 7 clones
256 contained complex rearrangements, with microhomology at the junction or insertions that
257 likely arose from replication template-switching events (Figure 2D; product h-n). For
258 example, product h appears to have arisen from fork collapse at the 5th repeat, followed
259 by two successive microhomology-mediated strand invasion and copying events,
260 followed by joining to a second fork that broke at the 15th repeat (Figure 2E). Together,
261 the sequencing data strongly suggest that stressed replication forks collapse in the
262 presence of B1-CDK1, generating DSBs that subsequently undergo end joining (Figures
263 2C and S2A), sometimes after repeated template-switching (Figure 2E).

264

265 **Immunodepletion of DNA Pol θ reduces mitotic ARPs**

266 We next addressed the mechanism of end joining after mitotic CDK-induced fork
267 collapse. As expected (Peterson et al., 2011), RAD51, which is essential for
268 homologous recombination (HR), did not bind chromatin in the presence of B1-CDK1
269 (Figure S3A). Accordingly, immunodepletion of RAD51 from egg extracts had no effect
270 on B1-CDK1-induced ARP formation (Figures S3B and S3C), nor did inhibition of
271 RAD51 with a BRC peptide derived from BRCA2 (Figure S3D) (Long et al., 2011).
272 Further, classical non-homologous end joining (NHEJ), which is also normally inhibited
273 during mitosis (Hustedt and Durocher, 2016), was not required for ARP formation
274 (Figure S3E). The structures of the mitotic ARPs (Figures 2C-E) suggested that MMEJ
275 (microhomology-mediated end joining, also called alternative end joining) and/or SSA
276 might be responsible for mitotic DSB repair. Indeed, immunodepletion of DNA

277 polymerase Pol θ (Figure 3A), a major mediator of MMEJ known to make errors due to
278 replicative template-switching (Wyatt et al., 2016), decreased ARPs during replication of
279 LacR plasmid (Figures 3B and S3F) and pDPC (Figures 3C and S3G). Additionally,
280 Pol θ depletion resulted in overall lower amounts of replication products (Figures S3F-
281 G), probably due to resection of unligated nascent strands. Moreover, Pol θ depletion
282 virtually eliminated ARPs containing complex rearrangements (Figures 3D-3E). Thus, in
283 mitotic extracts where HR and NHEJ are inactive, MMEJ appears to become a major
284 pathway that mediates joining of DNA ends after fork breakage.

285

286 **Condensin is dispensible for mitotic CDK-induced fork instability**

287 Chromatin condensation, a central event in mitosis, has long been proposed to cause
288 DNA damage in under-replicated regions (El Achkar et al., 2005; Lukas et al., 2011).
289 We therefore investigated the role of chromatin condensation on mitotic fork collapse in
290 egg extracts. Although immunodepletion of the condensin subunit SMC2 inhibited B1-
291 CDK1-induced chromosome condensation (Figures S4A-B), it did not affect the
292 formation of ARPs (Figures S4C-D). These results are consistent with our finding that
293 condensin recruitment did not induce DNA damage in the absence of replication stress
294 (Figures 1B, 1D, 1G and S1C-S1E). Therefore, chromatin condensation, *per se*, is
295 neither necessary nor sufficient for fork instability in mitotic egg extracts.

296

297 **CMG unloading at stalled forks initiates mitotic fork breakage**

298 When replication forks stall on either side of a DNA inter-strand crosslink (ICL) in
299 interphase egg extracts, CMGs are ubiquitylated and unloaded from chromatin by the
300 CDC48/p97 ATPase (Fullbright et al., 2016; Semlow et al., 2016). The loss of CMGs
301 from the stalled forks enables XPF-dependent ICL incision (Klein Douwel et al., 2014),
302 which unhooks the lesion, leading to the formation of a double-stranded DNA break that
303 is subsequently repaired via homologous recombination (Long et al., 2014). Inspired by
304 this mechanism, we asked whether B1-CDK1-induced fork breakage at single stalled
305 forks is caused by CMG unloading.

306 As shown previously (Dewar et al., 2015), CMGs that stalled at a LacR array did
307 not dissociate from chromatin in interphase extracts (Figure 4A, lane 1). In contrast, in
308 the presence of B1-CDK1, CMGs were unloaded efficiently (Figure 4A, lane 5). Addition
309 of the p97 inhibitor NMS-873 (p97-i) prevented B1-CDK1-triggered CMG unloading and
310 revealed a ladder of MCM7 species (Figure 4A, lane 7, red bracket) that was collapsed
311 by USP21, a non-specific deubiquitylating enzyme (Figure 4A, lane 8). Therefore, B1-
312 CDK1 induces MCM7 ubiquitylation and CMG unloading at single stalled forks,
313 demonstrating that in mitotic conditions, fork convergence is not required for CMG
314 unloading. Strikingly, p97-i suppressed the formation of ARPs on the LacR plasmid
315 (Figure 4B), strongly suggesting that B1-CDK1-induced CMG unloading triggers
316 replication fork breakage. Consistent with this interpretation, CMG unloading normally
317 preceded replication fork breakage (Figure S4E). Interestingly, in the presence of p97-i,
318 theta structures were converted to mature replication products (OC and SC) more
319 efficiently in the presence of B1-CDK1 than in its absence (Figure 4B, compare lanes
320 16-20 and 6-10), suggesting that B1-CDK1 may promote fork progression through the

321 array when CMG unloading is prevented. Treatment with p97-i also reduced the mitotic
322 CDK-induced γ -H2AX signal, consistent with inhibition of DSB formation (Figure S4F,
323 compare lanes 13-18 and 19-24). As seen for LacR plasmid, p97-i also prevented ARP
324 formation on pDPC (Figures 4C and S4G). Our data demonstrate that breakage of
325 stalled forks in the presence of mitotic CDK requires p97 activity.

326

327 **B1-CDK1-induced fork breakage requires PLK1 and AURKA, but not inhibition of**
328 **ATR signaling**

329 In dividing mammalian cells, inhibition of ATR signalling leads to fork breakage and
330 chromosomal fragmentation that depends on the protein kinases CDK1, PLK1, and
331 AURKA (Aurora kinase A) (Brown and Baltimore, 2000; Ragland et al., 2013). We
332 therefore examined how these kinases affect fork breakage in egg extracts. As shown in
333 Figure 4D, a potent ATR inhibitor (ATR-i, ETP-46464) did not induce breakage of forks
334 stalled at a LacR array in the absence of B1-CDK1 (measured by ARP formation), even
335 though the ATR-i abolished p-CHK1 (S345) and H2AX phosphorylation (lanes 7-12).
336 Conversely, the fork breakage observed in the presence of B1-CDK1 occurred even
337 though ATR signaling was active, as seen from p-CHK1 (Figure 4D, lanes 13-18), and
338 ATR-i did not further enhance breakage in this setting (Figure 4D, lanes 19-24).
339 Therefore, in interphase egg extract, ATR inhibition is insufficient to cause fork
340 breakage, and in mitotic extract, B1-CDK1 induces fork breakage even in the presence
341 of ATR activity. Strikingly, B1-CDK1-induced CMG ubiquitylation, CMG unloading, and
342 fork breakage were all suppressed by selective inhibitors of PLK1 or AURKA (Figures
343 4E-G). We conclude that in egg extracts that are arrested in a mitotic state, ATR is

344 unable to suppress fork breakage, whereas breakage depends on PLK1 and AURKA,
345 consistent with findings in mammalian cells (Ragland et al., 2013).

346

347 **B1-CDK1 induces replication fork collapse**

348 Replication fork collapse is defined as a state from which replication cannot restart, and
349 we wanted to determine whether B1-CDK1 induces such a state in egg extracts. As we
350 showed previously (Dewar et al., 2015), replication forks stalled at a LacR array are
351 able to resume synthesis upon addition of IPTG, leading to mature, supercoiled
352 replication products (Figure S4H, lanes 7-12). In the presence of B1-CDK1, IPTG did
353 not generate mature replication products (Figure S4H, lanes 19-24), presumably
354 because forks broke and underwent end-joining. However, when p97i was included with
355 B1-CDK1, mature replication products were fully recovered after IPTG addition (Figure
356 S4H, lanes 31-36). Thus, B1-CDK1 induces collapse of stalled replication forks and
357 inhibition of p97-dependent CMG unloading is sufficient to prevent this collapse.

358

359 **TRAIP promotes B1-CDK1-induced CMG unloading at stalled forks**

360 We next sought to identify the E3 ubiquitin ligase responsible for B1-CDK1-dependent
361 CMG unloading. CRL2^{Lrr1} promotes CMG unloading during replication termination
362 (Dewar et al., 2017), and it was possible that B1-CDK1 might target CRL2^{Lrr1} to stalled
363 CMGs. However, while the Cullin inhibitor MLN-4924 (Cul-i) blocked CMG unloading
364 during replication termination in interphase (Figure S5A, compare lanes 1 and 4)
365 (Dewar et al., 2017), it had almost no effect on mitotic CMG unloading from stalled forks

366 (Figure S5A, compare lanes 3 and 6), indicating the latter process does not involve
367 CRL2^{Lrr1}. Therefore, a Cullin-independent E3 ubiquitin ligase is responsible for MCM7
368 ubiquitylation upon premature mitotic entry.

369 The E3 ubiquitin ligase TRAIIP counteracts replication stress to maintain genome
370 integrity (Feng et al., 2016; Harley et al., 2016; Hoffmann et al., 2016; Soo Lee et al.,
371 2016), and we recently found that it is bound to replication forks that have stalled at a
372 LacR array (Dewar et al., 2017). Strikingly, immunodepletion of TRAIIP from egg extract
373 (Figure 5A) prevented B1-CDK1-induced CMG unloading at stalled forks (Figure 5B,
374 compare lanes 2 and 6), and it eliminated the polyubiquitylation of MCM7 detected in
375 the presence of p97-i (Figure 5B, compare lanes 4 and 8). Furthermore, TRAIIP
376 depletion abolished the formation of ARPs during replication of LacR plasmid (Figure
377 5C, compare lanes 7-12 and 19-24) and pDPC (Figure S5B). Re-addition of
378 recombinant wild TRAIIP (TRAIIP^{WT}) purified from bacteria (Wu et al., in revision,
379 manuscript enclosed) to TRAIIP-depleted egg extracts rescued the formation of mitotic
380 ARPs (Figure 5D; and Figures S5C-S5E). We also added back rTRAIIP^{R18C}, a point
381 mutant of TRAIIP that was identified in a human patient with primordial dwarfism (Harley
382 et al., 2016) and that exhibits severely reduced E3 ligase activity (Wu et al., in revision,
383 manuscript enclosed). Unlike rTRAIIP^{WT}, rTRAIIP^{R18C} supported only low levels of ARP
384 formation on LacR plasmid (Figure 5D, compare lanes 19-24 and 13-18). rTRAIIP^{ΔPIP}
385 lacking its C-terminal PCNA interaction motif (PIP box, amino acid 460-469) induced
386 mitotic ARPs as efficiently as rTRAIIP^{WT} (Figure S5F), indicating that TRAIIP's interaction
387 with PCNA is dispensible for CMG unloading. Accordingly, TRAIIP's PIP box is not
388 essential for the suppression of genome instability phenotypes in mammalian cells

389 (Hoffmann et al., 2016). We conclude that in the context of stalled forks, TRAIP is
390 essential for mitotic CDK-induced CMG unloading and fork collapse.

391

392 **Chromatin recruitment of TRAIP is not regulated by B1-CDK1**

393 To understand how TRAIP is regulated, we monitored its binding to chromatin. As we
394 showed previously (Dewar et al., 2017), in interphase egg extract TRAIP is associated
395 with replisomes that have stalled at a LacR array (Figure 5B, lane 1). Therefore, TRAIP
396 is present at forks before they are exposed to B1-CDK1. Upon addition of B1-CDK1,
397 TRAIP was lost from the chromatin, but not when CMG unloading was inhibited with
398 p97-i (Figure 5B, compare lanes 2 and 4). Interestingly, chromatin-bound TRAIP did not
399 increase in the presence of B1-CDK1 and p97-i compared to the level observed before
400 B1-CDK1 addition (Figure 5B, compare lanes 1 and 4). These data suggest that mitotic
401 CDK activates TRAIP in a manner that does not involve its *de novo* recruitment to the
402 fork.

403

404 **Fork breakage in mitotic extracts is distinct from programmed incisions during** 405 **ICL repair**

406 The breakage of single stalled forks in mitotic egg extracts shown here is reminiscent
407 of breakage at forks that have converged on cisplatin ICLs in interphase egg extracts in
408 that both events require TRAIP-dependent CMG unloading (Figure 5 and Wu *et al.*, in
409 revision). We therefore asked whether B1-CDK-induced breakage at single forks also
410 requires FANCI-FANCD2, XPF-ERCC1, or SLX1-SLX4, which promote DNA incisions

411 during ICL repair. Immunodepletion of FANCI-FANCD2 did not prevent mitotic ARP
412 formation on LacR plasmid (Figures S5G-H), nor did depletion of SLX4, XPF, or MUS81
413 (data not shown). We speculate that there might be redundancy among SLX1, XPF, and
414 MUS81 for mitotic fork breakage, or that other nucleases are involved. Our results
415 indicate that while ICL incisions and B1-CDK1-dependent replication fork collapse both
416 require TRAIP-dependent CMG unloading, these processes are otherwise
417 mechanistically distinct.

418

419 **TRAIP promotes CMG unloading from terminated replisomes in mitosis**

420 In *C. elegans* early embryos lacking $CUL2^{LRR-1}$, CMGs persist on chromatin until late
421 prophase, when they are unloaded from chromatin by p97 (Sonneville et al., 2017). This
422 observation indicated that an alternative ubiquitylation pathway acts to unload
423 terminated CMGs in mitosis, but the relevant E3 ubiquitin ligase has not been identified.
424 To determine whether TRAIP is involved in this pathway, we first addressed whether
425 *Xenopus* egg extracts recapitulate mitotic unloading of CMGs that have undergone
426 replication termination. To this end, we replicated a plasmid in interphase egg extracts
427 in the presence of Cul-i. In this condition, DNA synthesis went to completion (Figure
428 S6A), but CMG unloading was blocked due to inhibition of $CRL2^{Lrr1}$ (Figure 6A, compare
429 lanes 1 and 2; (Dewar et al., 2017)). Importantly, upon addition of B1-CDK1, CMG was
430 unloaded despite the presence of Cul-i (Figure 6A, lane 6), and this unloading was
431 blocked by p97-i (Figure 6A, lane 8). Therefore, as seen in worms, mitotic frog egg
432 extracts support $CRL2^{Lrr1}$ -independent unloading of terminated CMGs. Interestingly, in
433 the presence of p97-i, MCM7 was ubiquitylated even more extensively than in

434 interphase extract (Figure 6A, compare lanes 7-8 and 3-4 and Figure S6B, compare
435 lanes 5-6 and 1-2). This hyper-ubiquitylation was unaffected by Cul-i (Figure 6A, lane
436 8), indicating that it is CRL2^{Lrr1}-independent. Importantly, TRAIP depletion inhibited B1-
437 CDK1-induced CMG unloading from terminated forks (Figure 6B, compare lanes 1 and
438 4, and Figure S6C, compare lanes 1 and 4) and MCM7 hyper-ubiquitylation in the
439 presence of p97-i (Figure 6B, compare lanes 2 and 5 as well as lanes 3 and 6). These
440 defects were reversed by rTRAIP^{WT} but not rTRAIP^{R18C} (Figures 6B and S6C).
441 Therefore, in the absence of CRL2^{Lrr1} activity, TRAIP promotes an alternative pathway
442 to unload terminated CMGs in mitotic egg extract.

443 We next asked whether the *C. elegans* orthologue of TRAIP, which we called
444 TRUL-1 (Traip Ubiquitin Ligase 1, encoded by the previously uncharacterised *C.*
445 *elegans* gene B0432.13), controls removal of CMG from chromatin in mitosis of the first
446 embryonic cell cycle (Figure 6C). On its own, RNAi depletion of TRUL-1 had no impact
447 on CMG disassembly. However, simultaneous depletion of TRUL-1 and LRR-1 led to
448 the persistence of the PSF-1 and CDC-45 subunits of CMG on mitotic chromatin
449 (Figures 6D and S6D), indicating that *C. elegans* TRAIP is required for the removal of
450 CMG from mitotic chromatin in animals. Moreover, compared to single depletion of
451 TRUL-1 or LRR-1, double depletion led to the accumulation of CMG complexes
452 containing unmodified MCM7 (Figure 6E, lane 7). This contrasts with the persistence of
453 ubiquitylated CMGs observed upon depletion of p97's cofactor NPL-4 (Figures 6E and
454 6F, lane 8) (Sonneville et al., 2017). Thus, unloading of terminated CMGs in mitosis is a
455 conserved function of TRAIP in metazoans. Moreover, our results suggest that in
456 mitosis, TRAIP removes all forms of CMG from chromatin, whether they have

457 terminated or stalled (Figure S6E). In the latter case, CMG unloading triggers fork
458 breakage and complex end joining events (Figure 7).

459

460 **DISCUSSION**

461 When cells enter mitosis before DNA replication is complete, replication forks break.
462 However, the molecular events underlying breakage and how breakage affects genome
463 stability have remained unclear. Here, we show that in mitotic egg extracts, the E3
464 ubiquitin ligase TRAIP promotes p97-dependent replisome disassembly, followed by
465 replication fork breakage and end joining events involving SSA and MMEJ. As
466 discussed below, we propose that TRAIP-dependent fork breakage can be beneficial or
467 detrimental, primarily depending on the burden of stressed forks at mitotic entry.

468 TRAIP's regulation of CMG ubiquitylation is critically dependent on cell-cycle
469 status. In the presence of B1-CDK1, TRAIP targets stalled CMGs, which encircle
470 ssDNA, and terminated CMGs, which probably encircle dsDNA (Figure S6Ei and ii;
471 (Dewar et al., 2015)). In contrast, TRAIP's action in interphase extracts is more
472 selective. In this setting, TRAIP promotes the ubiquitylation of CMGs that have
473 converged on an ICL, leading to activation of two distinct mechanisms of ICL repair (Wu
474 et al., in revision; Figure S6Eiii). However, it does not target terminated CMGs, a
475 function performed by CRL2^{Lrr1} in S phase (Figure S6Div; (Dewar et al., 2017;
476 Sonnevile et al., 2017)), nor does TRAIP appear to target CMG at single moving or
477 stalled forks, which would cause premature fork collapse. In summary, TRAIP is specific
478 for converged CMGs in interphase whereas in the presence of B1-CDK1, it appears to
479 target any CMG, regardless of its configuration on DNA. Future work will be required to
480 understand how TRAIP's selectivity is modulated by phosphorylation.

481 It has been widely proposed that replisome disassembly causes fork collapse
482 (Cortez, 2015; Toledo et al., 2017), but in the absence of a mechanism for disassembly,

483 testing this idea has been impossible. Here, we identify such a mechanism. We show
484 that B1-CDK1 induces TRAIIP-dependent CMG ubiquitylation, p97-dependent CMG
485 unloading, fork breakage, and fork collapse. This cascade is inhibited via multiple
486 independent manipulations (CDK1-i, PLK1-i, p97-i, TRAIIP depletion) that all target the
487 replisome disassembly step. Thus, our data establish a firm relationship between
488 replisome disassembly, fork breakage, and collapse. Whether the inability to restart the
489 fork (collapse) results from replisome disassembly *per se* or a downstream event such
490 as fork breakage is presently unclear. Moreover, without active recombinant MCM2-7,
491 we cannot make ubiquitylation site mutations that would directly test whether CMG is the
492 relevant TRAIIP substrate responsible for fork breakage. Nevertheless, multiple lines of
493 evidence point to CMG as the most likely target. First, TRAIIP associates with stalled
494 and terminated replication forks (Dewar et al., 2017; Hoffmann et al., 2016), ideally
495 positioning TRAIIP for CMG ubiquitylation. Second, prior to fork collapse, B1-CDK1
496 induces rapid and quantitative ubiquitylation of MCM7, the same protein that is
497 ubiquitylated when CMG is unloaded during replication termination. Finally, CMG is
498 unique among replisome components in that it cannot be reloaded *de novo* in S phase
499 (Deegan and Diffley, 2016). Thus, loss of CMG provides a simple explanation for the
500 irreversibility of fork collapse. It will be interesting to determine how this pathway relates
501 to the depletion of RPA at the fork, which has also been proposed to trigger fork
502 collapse and breakage (Toledo et al., 2013).

503 After stressed forks undergo breakage in mitotic extracts, the newly formed DNA
504 breaks undergo two classes of joining events, as revealed by DNA sequencing. The first
505 class involves deletions of *lacO* repeats. These products are most readily explained by

506 single-strand annealing, and they are probably favored by the highly repetitive nature of
507 the *lacO* array. SSA is usually RAD52 dependent (Bhargava et al., 2016), and RAD52
508 has recently been shown to mediate DNA repair synthesis during mitosis (Bhowmick et
509 al., 2016). However, we have not been able to test the involvement of RAD52 due to an
510 inability to raise antibodies against *Xenopus* RAD52. The second class of end joining
511 products is mediated by micro-homology, sometimes with multiple template-switching
512 events, indicative of DNA Pol theta (Pol θ)-mediated end joining (MMEJ, (Wyatt et al.,
513 2016)). Consistent with this idea, aberrant replication products were reduced and
514 complex rearrangements were eliminated in Pol θ -depleted extracts. Our observation
515 that broken forks appear to be processed primarily by SSA and MMEJ is consistent with
516 the findings that HR and NHEJ are inhibited in mitosis (Figure S3A and (Hustedt and
517 Durocher, 2016; Ochs et al., 2016; Peterson et al., 2011)) and that inhibition of these
518 processes had no effect on the formation of aberrant replication products (Figures S3B-
519 S3E). Notably, we detected only short-tract template switches typical of MMEJ. If
520 template-switching events mediated by Pol θ or other factors were followed by more
521 processive DNA synthesis that is templated near the break, duplications could result
522 that resemble copy number alterations observed in human cancer and congenital
523 disease (Carvalho and Lupski, 2016; Leibowitz et al., 2015).

524 We envision at least two beneficial effects of TRAP1-dependent replisome
525 disassembly in mitosis. One arises when converging forks are unable to complete DNA
526 replication by anaphase, as seen at common fragile sites (CFS) (West and Chan,
527 2018). We propose that TRAP1-dependent CMG unloading leads to preferential
528 breakage on the two leading strand templates because these are normally protected by

529 CMG (Fu et al., 2011) and therefore exposed after CMG dissociation (Figure S7). In this
530 scenario, one intact daughter chromosome would immediately be restored by gap filling,
531 and the other could be regenerated via joining of the two broken ends, albeit with sister
532 chromatid exchange and at the cost of of a deletion (Figure S7, left branch). Importantly,
533 this mechanism avoids the formation of acentric and dicentric chromosomes that would
534 result if the forks underwent random breakage (Figure S7, right branch) and thus biases
535 breakage at CFS towards more beneficial outcomes. Strikingly, CFS expression
536 induces chromosomal alterations that exhibit key features expected of our model,
537 including submicroscopic deletions covering the CFS locus, microhomologies at the
538 breakpoint junctions, and a very high frequency of sister chromatid exchanges (Glover
539 et al., 2017) (Figure S7, left branch). Unlike our biased breakage and end joining model,
540 break-induced replication models of CFS expression (Bhowmick et al., 2016;
541 Minocherhomji et al., 2015) do not readily account for the high incidence of sister
542 chromatid exchanges at CFS, and they would not be beneficial at CFS located distant
543 from chromosome ends.

544 A second possible benefit of TRAIIP activity in mitosis is to disassemble
545 terminated CMGs that evaded the action of $CRL2^{Lrr1}$ in the previous S phase. In
546 principle, such CMGs might interfere with transcription or replication in the next cell
547 cycle. However, MCM2-7 complexes that are newly-loaded during mitotic exit, which
548 also encircle dsDNA, do not appear to interfere with these processes. Therefore, a
549 negative impact on transcription or replication would have to be specific to the full CMG
550 complex. In the absence of an obvious mechanism that explains strong detrimental
551 effects of residual CMGs, we favor the idea that TRAIIP's primary function in mitosis is to

552 resolve unreplicated loci.

553 In addition to its beneficial effects, we propose that TRAIIP-dependent CMG
554 unloading contributes to various genome instability phenomena that were previously
555 linked to mitotic DNA replication. These include: chromosome breakage that occurs
556 when S and M phase cells are fused (Duelli et al., 2007; Johnson and Rao, 1970; Rao
557 et al., 1982) or when mitotic CDK is prematurely activated in S phase by WEE1
558 inhibition (Dominguez-Kelly et al., 2011; Duda et al., 2016); and chromothripsis in
559 micronuclei that are still engaged in replication when they enter mitosis (Crasta et al.,
560 2012; Leibowitz et al., 2015; Ly et al., 2017). In these cases, massive chromosomal
561 breakage leads to genome instability or cell death. Notably, chromosome fragmentation
562 in the presence of WEE1 inhibitor and common fragile site expression are both MUS81-
563 dependent (Dominguez-Kelly et al., 2011; Duda et al., 2016; Naim et al., 2013; Ying et
564 al., 2013). In contrast, fork breakage in our experiments was not inhibited by MUS81
565 depletion. Whether this reflects a real difference in these processes, incomplete MUS81
566 depletion in extracts, or greater redundancy with other nucleases in extracts remains to
567 be determined. In the future, it will be interesting to determine whether TRAIIP underlies
568 different genome instability phenomena caused by premature mitotic entry.

569 Much work towards understanding fork collapse focuses on its regulation by ATR.
570 While ATR-dependent phosphorylation of SMARCAL1 and WRN regulates fork stability,
571 these ATR substrates do not appear to account for ATR's essential role in preventing
572 fork collapse (Cortez, 2015; Pasero and Vindigni, 2017; Saldivar et al., 2017). Instead, a
573 growing body of evidence suggests that ATR affects fork stability indirectly (Toledo et al.,
574 2017). For example, ATR inhibition of late origin firing prevents exhaustion of the

575 nuclear RPA pool, causing fork deprotection and breakage (Toledo et al., 2013).
576 However, given the concentration of RPA in egg extracts (~10 μ M; (Walter et al., 1998;
577 Wuhr et al., 2015)), and the concentration of DNA in our experiments, RPA cannot be
578 exhausted in our experiments. Another hypothesis to explain the effect of ATR on fork
579 stability involves the suppression of mitotic kinases. In cells treated with Aphidicolin and
580 ATRi, replication fork collapse depends on B1-CDK1, AURKA, and PLK1 (Eykelboom
581 et al., 2013; Ragland et al., 2013; Ruiz et al., 2016). Even in the absence of exogenous
582 replication stress, ATR prevents the premature accumulation of Cyclin B and PLK1 in S
583 phase, which is critical to suppress replication fork collapse and genome instability (Ruiz
584 et al., 2016; Saldivar et al., 2018). Thus, replication fork collapse in interphase can be
585 due to premature activation of mitotic kinases. Consistent with the central importance of
586 ATR in restraining B-CDK1, ATR is not required to stabilize stalled DNA replication forks
587 in egg extracts that are permanently arrested in interphase (Figure 4D; (Luciani et al.,
588 2004)). Conversely, when stressed forks are exposed to B1-CDK1, forks break, even in
589 the presence of ATR activity. Based on these observations, we propose that in many
590 studies where ATR suppresses replication fork collapse, this is due to suppression of
591 B1-CDK1 activity and the prevention of TRAIP-dependent replisome disassembly.

592 In summary, our data suggest that when TRAIP is activated by mitotic CDK, a
593 short temporal window opens in which replication forks can finish replication and
594 terminate. The window closes when CMGs are ubiquitylated and extracted from
595 chromatin. In the presence of a few unreplicated loci (e.g. fragile sites), CMG unloading
596 and fork breakage promotes chromosome segregation and genome integrity, but when
597 many forks are present (e.g. micronuclei, premature CDK1 activation in S phase),

598 massive DNA fragmentation results, leading to cell death or transformation. Whether the
599 dwarfism phenotype observed in patients with TRAIP mutations results from defects in
600 the resolution of unreplicated loci, persistence of terminated CMGs, defective ICL
601 repair (Wu et al., in revision), or defects in other TRAIP-dependent processes remains
602 to be established.

603

604

605 **ACKNOWLEDGMENTS**

606 We thank James Dewar, Emily Low, Justin Sparks, Kyle Vrtis, Daniel Finley, Puck
607 Knipscheer, and Jan-Michael Peters for experimental protocols or reagents. We thank
608 Alan D'Andrea, Randy King, Ralph Scully, and members of the Pellman and Walter
609 laboratories for helpful discussion and critical reading of the manuscript. R.A.W. was
610 supported by postdoctoral fellowship 131415-PF-17-168-01-DMC from the American
611 Cancer Society. D.P. was supported by NIH grant CA213404. J.C.W. was supported by
612 NIH grants GM080676 and HL098316. D.P. and J.C.W. are investigators of the Howard
613 Hughes Medical Institute.

614

615 **AUTHOR CONTRIBUTIONS**

616 D.P. initiated the project. L.D., D.P., and J.C.W. designed the experiments, interpreted
617 the results, and prepared the manuscript. R.A.W. contributed recombinant TRAIP
618 proteins and obtained initial evidence that TRAIP is required for CMG unloading. R.S.
619 performed and K.L. directed experiments in worms (Figures 6C-6F and S6D). O.V.K.

620 contributed Figures 6A-B and S6A-C; L.D. designed and performed all other
621 experiments.

622

623 **DECLARATION OF INTERESTS**

624 The authors declare no competing interests.

625 **REFERENCES**

- 626 Ammazalorso, F., Pirzio, L.M., Bignami, M., Franchitto, A., and Pichierri, P. (2010). ATR and ATM differently
627 regulate WRN to prevent DSBs at stalled replication forks and promote replication fork recovery. *EMBO J* 29,
628 3156-3169.
- 629 Baumann, C., Korner, R., Hofmann, K., and Nigg, E.A. (2007). PICH, a centromere-associated SNF2 family
630 ATPase, is regulated by Plk1 and required for the spindle checkpoint. *Cell* 128, 101-114.
- 631 Bhargava, R., Onyango, D.O., and Stark, J.M. (2016). Regulation of Single-Strand Annealing and its Role in
632 Genome Maintenance. *Trends Genet* 32, 566-575.
- 633 Bhowmick, R., and Hickson, I.D. (2017). The "enemies within": regions of the genome that are inherently difficult
634 to replicate. *F1000Res* 6, 666.
- 635 Bhowmick, R., Minocherhomji, S., and Hickson, I.D. (2016). RAD52 Facilitates Mitotic DNA Synthesis Following
636 Replication Stress. *Mol Cell* 64, 1117-1126.
- 637 Blow, J.J., and Laskey, R.A. (1986). Initiation of DNA replication in nuclei and purified DNA by a cell-free extract
638 of *Xenopus* eggs. *Cell* 47, 577-587.
- 639 Brenner, S. (1974). The genetics of *Caenorhabditis elegans*. *Genetics* 77, 71-94.
- 640 Brown, E.J., and Baltimore, D. (2000). ATR disruption leads to chromosomal fragmentation and early embryonic
641 lethality. *Genes Dev* 14, 397-402.
- 642 Budzowska, M., Graham, T.G., Soback, A., Waga, S., and Walter, J.C. (2015). Regulation of the Rev1-pol zeta
643 complex during bypass of a DNA interstrand cross-link. *EMBO J* 34, 1971-1985.
- 644 Carvalho, C.M., and Lupski, J.R. (2016). Mechanisms underlying structural variant formation in genomic disorders.
645 *Nat Rev Genet* 17, 224-238.
- 646 Chan, K.L., North, P.S., and Hickson, I.D. (2007). BLM is required for faithful chromosome segregation and its
647 localization defines a class of ultrafine anaphase bridges. *EMBO J* 26, 3397-3409.
- 648 Cortez, D. (2015). Preventing replication fork collapse to maintain genome integrity. *DNA Repair (Amst)* 32, 149-
649 157.
- 650 Couch, F.B., Bansbach, C.E., Driscoll, R., Luzwick, J.W., Glick, G.G., Betous, R., Carroll, C.M., Jung, S.Y., Qin, J.,
651 Cimprich, K.A., *et al.* (2013). ATR phosphorylates SMARCAL1 to prevent replication fork collapse. *Genes Dev* 27,
652 1610-1623.
- 653 Crasta, K., Ganem, N.J., Dagher, R., Lantermann, A.B., Ivanova, E.V., Pan, Y., Nezi, L., Protopopov, A.,
654 Chowdhury, D., and Pellman, D. (2012). DNA breaks and chromosome pulverization from errors in mitosis. *Nature*
655 482, 53-58.
- 656 De Piccoli, G., Katou, Y., Itoh, T., Nakato, R., Shirahige, K., and Labib, K. (2012). Replisome stability at defective
657 DNA replication forks is independent of S phase checkpoint kinases. *Mol Cell* 45, 696-704.
- 658 Deegan, T.D., and Diffley, J.F. (2016). MCM: one ring to rule them all. *Curr Opin Struct Biol* 37, 145-151.
- 659 Dewar, J.M., Budzowska, M., and Walter, J.C. (2015). The mechanism of DNA replication termination in
660 vertebrates. *Nature* 525, 345-350.
- 661 Dewar, J.M., Low, E., Mann, M., Raschle, M., and Walter, J.C. (2017). CRL2Lrr1 promotes unloading of the
662 vertebrate replisome from chromatin during replication termination. *Genes Dev* 31, 275-290.
- 663 Dominguez-Kelly, R., Martin, Y., Koundrioukoff, S., Tanenbaum, M.E., Smits, V.A., Medema, R.H., Debatisse, M.,
664 and Freire, R. (2011). Wee1 controls genomic stability during replication by regulating the Mus81-Eme1
665 endonuclease. *J Cell Biol* 194, 567-579.
- 666 Duda, H., Arter, M., Gloggnitzer, J., Teloni, F., Wild, P., Blanco, M.G., Altmeyer, M., and Matos, J. (2016). A
667 Mechanism for Controlled Breakage of Under-replicated Chromosomes during Mitosis. *Dev Cell* 39, 740-755.
- 668 Duelli, D.M., Padilla-Nash, H.M., Berman, D., Murphy, K.M., Ried, T., and Lazebnik, Y. (2007). A virus causes
669 cancer by inducing massive chromosomal instability through cell fusion. *Curr Biol* 17, 431-437.
- 670 Dungrawala, H., Rose, K.L., Bhat, K.P., Mohni, K.N., Glick, G.G., Couch, F.B., and Cortez, D. (2015). The
671 Replication Checkpoint Prevents Two Types of Fork Collapse without Regulating Replisome Stability. *Mol Cell* 59,
672 998-1010.
- 673 Duxin, J.P., Dewar, J.M., Yardimci, H., and Walter, J.C. (2014). Repair of a DNA-protein crosslink by replication-
674 coupled proteolysis. *Cell* 159, 346-357.
- 675 El Achkar, E., Gerbault-Seureau, M., Muleris, M., Dutrillaux, B., and Debatisse, M. (2005). Premature condensation
676 induces breaks at the interface of early and late replicating chromosome bands bearing common fragile sites. *Proc*
677 *Natl Acad Sci U S A* 102, 18069-18074.

678 Eykelenboom, J.K., Harte, E.C., Canavan, L., Pastor-Peidro, A., Calvo-Asensio, I., Llorens-Agost, M., and Lowndes,
679 N.F. (2013). ATR activates the S-M checkpoint during unperturbed growth to ensure sufficient replication prior to
680 mitotic onset. *Cell Rep* 5, 1095-1107.

681 Feng, W., Guo, Y., Huang, J., Deng, Y., Zang, J., and Huen, M.S. (2016). TRAIIP regulates replication fork recovery
682 and progression via PCNA. *Cell Discov* 2, 16016.

683 Fu, Y.V., Yardimci, H., Long, D.T., Ho, T.V., Guainazzi, A., Bermudez, V.P., Hurwitz, J., van Oijen, A., Scharer,
684 O.D., and Walter, J.C. (2011). Selective bypass of a lagging strand roadblock by the eukaryotic replicative DNA
685 helicase. *Cell* 146, 931-941.

686 Fullbright, G., Rycenga, H.B., Gruber, J.D., and Long, D.T. (2016). p97 Promotes a Conserved Mechanism of
687 Helicase Unloading during DNA Cross-Link Repair. *Mol Cell Biol* 36, 2983-2994.

688 Glover, T.W., Wilson, T.E., and Arlt, M.F. (2017). Fragile sites in cancer: more than meets the eye. *Nat Rev Cancer*
689 17, 489-501.

690 Harley, M.E., Murina, O., Leitch, A., Higgs, M.R., Bicknell, L.S., Yigit, G., Blackford, A.N., Zlatanou, A.,
691 Mackenzie, K.J., Reddy, K., *et al.* (2016). TRAIIP promotes DNA damage response during genome replication and is
692 mutated in primordial dwarfism. *Nat Genet* 48, 36-43.

693 Harrigan, J.A., Belotserkovskaya, R., Coates, J., Dimitrova, D.S., Polo, S.E., Bradshaw, C.R., Fraser, P., and
694 Jackson, S.P. (2011). Replication stress induces 53BP1-containing OPT domains in G1 cells. *J Cell Biol* 193, 97-
695 108.

696 Hendrickson, M., Madine, M., Dalton, S., and Gautier, J. (1996). Phosphorylation of MCM4 by cdc2 protein kinase
697 inhibits the activity of the minichromosome maintenance complex. *Proc Natl Acad Sci U S A* 93, 12223-12228.

698 Hills, S.A., and Diffley, J.F. (2014). DNA replication and oncogene-induced replicative stress. *Curr Biol* 24, R435-
699 444.

700 Hoffmann, S., Smedegaard, S., Nakamura, K., Mortuza, G.B., Raschle, M., Ibanez de Opakua, A., Oka, Y., Feng, Y.,
701 Blanco, F.J., Mann, M., *et al.* (2016). TRAIIP is a PCNA-binding ubiquitin ligase that protects genome stability after
702 replication stress. *J Cell Biol* 212, 63-75.

703 Holland, A.J., and Cleveland, D.W. (2012). Chromoanagenesis and cancer: mechanisms and consequences of
704 localized, complex chromosomal rearrangements. *Nat Med* 18, 1630-1638.

705 Hustedt, N., and Durocher, D. (2016). The control of DNA repair by the cell cycle. *Nat Cell Biol* 19, 1-9.

706 Johnson, R.T., and Rao, P.N. (1970). Mammalian cell fusion: induction of premature chromosome condensation in
707 interphase nuclei. *Nature* 226, 717-722.

708 Kato, H., and Sandberg, A.A. (1968). Chromosome pulverization in human cells with micronuclei. *J Natl Cancer*
709 *Inst* 40, 165-179.

710 Klein Douwel, D., Boonen, R.A., Long, D.T., Szybowska, A.A., Raschle, M., Walter, J.C., and Knipscheer, P.
711 (2014). XPF-ERCC1 acts in Unhooking DNA interstrand crosslinks in cooperation with FANCD2 and
712 FANCP/SLX4. *Mol Cell* 54, 460-471.

713 Knipscheer, P., Raschle, M., Smogorzewska, A., Enoiu, M., Ho, T.V., Scharer, O.D., Elledge, S.J., and Walter, J.C.
714 (2009). The Fanconi anemia pathway promotes replication-dependent DNA interstrand cross-link repair. *Science*
715 326, 1698-1701.

716 Lebofsky, R., Takahashi, T., and Walter, J.C. (2009). DNA replication in nucleus-free *Xenopus* egg extracts.
717 *Methods Mol Biol* 521, 229-252.

718 Leibowitz, M.L., Zhang, C.Z., and Pellman, D. (2015). Chromothripsis: A New Mechanism for Rapid Karyotype
719 Evolution. *Annu Rev Genet* 49, 183-211.

720 Liu, P., Erez, A., Nagamani, S.C., Dhar, S.U., Kolodziejska, K.E., Dharmadhikari, A.V., Cooper, M.L.,
721 Wiszniewska, J., Zhang, F., Withers, M.A., *et al.* (2011). Chromosome catastrophes involve replication mechanisms
722 generating complex genomic rearrangements. *Cell* 146, 889-903.

723 Long, D.T., Joukov, V., Budzowska, M., and Walter, J.C. (2014). BRCA1 promotes unloading of the CMG helicase
724 from a stalled DNA replication fork. *Mol Cell* 56, 174-185.

725 Long, D.T., Raschle, M., Joukov, V., and Walter, J.C. (2011). Mechanism of RAD51-dependent DNA interstrand
726 cross-link repair. *Science* 333, 84-87.

727 Luciani, M.G., Oehlmann, M., and Blow, J.J. (2004). Characterization of a novel ATR-dependent, Chk1-
728 independent, intra-S-phase checkpoint that suppresses initiation of replication in *Xenopus*. *J Cell Sci* 117, 6019-
729 6030.

730 Lukas, C., Savic, V., Bekker-Jensen, S., Doil, C., Neumann, B., Pedersen, R.S., Grofte, M., Chan, K.L., Hickson,
731 I.D., Bartek, J., *et al.* (2011). 53BP1 nuclear bodies form around DNA lesions generated by mitotic transmission of
732 chromosomes under replication stress. *Nat Cell Biol* 13, 243-253.

733 Ly, P., Teitz, L.S., Kim, D.H., Shoshani, O., Skaletsky, H., Fachinetti, D., Page, D.C., and Cleveland, D.W. (2017).
 734 Selective Y centromere inactivation triggers chromosome shattering in micronuclei and repair by non-homologous
 735 end joining. *Nat Cell Biol* *19*, 68-75.
 736 Mankouri, H.W., Huttner, D., and Hickson, I.D. (2013). How unfinished business from S-phase affects mitosis and
 737 beyond. *EMBO J* *32*, 2661-2671.
 738 Minocherhomji, S., Ying, S., Bjerregaard, V.A., Bursomanno, S., Aleliunaite, A., Wu, W., Mankouri, H.W., Shen,
 739 H., Liu, Y., and Hickson, I.D. (2015). Replication stress activates DNA repair synthesis in mitosis. *Nature*.
 740 Naim, V., Wilhelm, T., Debatisse, M., and Rosselli, F. (2013). ERCC1 and MUS81-EME1 promote sister chromatid
 741 separation by processing late replication intermediates at common fragile sites during mitosis. *Nat Cell Biol* *15*,
 742 1008-1015.
 743 Ochs, F., Somyajit, K., Altmeyer, M., Rask, M.B., Lukas, J., and Lukas, C. (2016). 53BP1 fosters fidelity of
 744 homology-directed DNA repair. *Nat Struct Mol Biol* *23*, 714-721.
 745 Pasero, P., and Vindigni, A. (2017). Nucleases Acting at Stalled Forks: How to Reboot the Replication Program
 746 with a Few Shortcuts. *Annu Rev Genet* *51*, 477-499.
 747 Peterson, S.E., Li, Y., Chait, B.T., Gottesman, M.E., Baer, R., and Gautier, J. (2011). Cdk1 uncouples CtIP-
 748 dependent resection and Rad51 filament formation during M-phase double-strand break repair. *J Cell Biol* *194*, 705-
 749 720.
 750 Prokhorova, T.A., Mowrer, K., Gilbert, C.H., and Walter, J.C. (2003). DNA replication of mitotic chromatin in
 751 *Xenopus* egg extracts. *Proc Natl Acad Sci U S A* *100*, 13241-13246.
 752 Ragland, R.L., Patel, S., Rivard, R.S., Smith, K., Peters, A.A., Bielinsky, A.K., and Brown, E.J. (2013). RNF4 and
 753 PLK1 are required for replication fork collapse in ATR-deficient cells. *Genes Dev* *27*, 2259-2273.
 754 Rao, P.N., Johnson, R.T., and Sperling, K. (1982). *Premature Chromosome Condensation: Application in*
 755 *Basic, Clinical, and Mutation Research* (New York: Academic Press).
 756 Raschle, M., Knipscheer, P., Enoiu, M., Angelov, T., Sun, J., Griffith, J.D., Ellenberger, T.E., Scharer, O.D., and
 757 Walter, J.C. (2008). Mechanism of replication-coupled DNA interstrand crosslink repair. *Cell* *134*, 969-980.
 758 Raschle, M., Smeenk, G., Hansen, R.K., Temu, T., Oka, Y., Hein, M.Y., Nagaraj, N., Long, D.T., Walter, J.C.,
 759 Hofmann, K., *et al.* (2015). DNA repair. Proteomics reveals dynamic assembly of repair complexes during bypass of
 760 DNA cross-links. *Science* *348*, 1253671.
 761 Ruiz, S., Mayor-Ruiz, C., Lafarga, V., Murga, M., Vega-Sendino, M., Ortega, S., and Fernandez-Capetillo, O.
 762 (2016). A Genome-wide CRISPR Screen Identifies CDC25A as a Determinant of Sensitivity to ATR Inhibitors. *Mol*
 763 *Cell* *62*, 307-313.
 764 Saldivar, J.C., Cortez, D., and Cimprich, K.A. (2017). The essential kinase ATR: ensuring faithful duplication of a
 765 challenging genome. *Nat Rev Mol Cell Biol* *18*, 622-636.
 766 Saldivar, J.C., Hamperl, S., Bocek, M.J., Chung, M., Bass, T.E., Cisneros-Soberanis, F., Samejima, K., Xie, L.,
 767 Paulson, J.R., Earnshaw, W.C., *et al.* (2018). An intrinsic S/G2 checkpoint enforced by ATR. *Science* *361*, 806-810.
 768 Semlow, D.R., Zhang, J., Budzowska, M., Drohat, A.C., and Walter, J.C. (2016). Replication-Dependent Unhooking
 769 of DNA Interstrand Cross-Links by the NEIL3 Glycosylase. *Cell* *167*, 498-511 e414.
 770 Sonnevile, R., Moreno, S.P., Knebel, A., Johnson, C., Hastie, C.J., Gartner, A., Gambus, A., and Labib, K. (2017).
 771 CUL-2LRR-1 and UBXN-3 drive replisome disassembly during DNA replication termination and mitosis. *Nat Cell*
 772 *Biol* *19*, 468-479.
 773 Soo Lee, N., Jin Chung, H., Kim, H.J., Yun Lee, S., Ji, J.H., Seo, Y., Hun Han, S., Choi, M., Yun, M., Lee, S.G., *et*
 774 *al.* (2016). TRAI/RNF206 is required for recruitment of RAP80 to sites of DNA damage. *Nat Commun* *7*, 10463.
 775 Stephens, P.J., Greenman, C.D., Fu, B., Yang, F., Bignell, G.R., Mudie, L.J., Pleasance, E.D., Lau, K.W., Beare, D.,
 776 Stebbings, L.A., *et al.* (2011). Massive genomic rearrangement acquired in a single catastrophic event during cancer
 777 development. *Cell* *144*, 27-40.
 778 Strausfeld, U.P., Howell, M., Descombes, P., Chevalier, S., Rempel, R.E., Adamczewski, J., Maller, J.L., Hunt, T.,
 779 and Blow, J.J. (1996). Both cyclin A and cyclin E have S-phase promoting (SPF) activity in *Xenopus* egg extracts. *J*
 780 *Cell Sci* *109*, 1555-1563.
 781 Techer, H., Koundrioukoff, S., Nicolas, A., and Debatisse, M. (2017). The impact of replication stress on replication
 782 dynamics and DNA damage in vertebrate cells. *Nat Rev Genet* *18*, 535-550.
 783 Timmons, L., and Fire, A. (1998). Specific interference by ingested dsRNA. *Nature* *395*, 854.
 784 Toledo, L., Neelsen, K.J., and Lukas, J. (2017). Replication Catastrophe: When a Checkpoint Fails because of
 785 Exhaustion. *Mol Cell* *66*, 735-749.
 786 Toledo, L.I., Altmeyer, M., Rask, M.B., Lukas, C., Larsen, D.H., Povlsen, L.K., Bekker-Jensen, S., Mailand, N.,
 787 Bartek, J., and Lukas, J. (2013). ATR prohibits replication catastrophe by preventing global exhaustion of RPA. *Cell*
 788 *155*, 1088-1103.

789 Walter, J., and Newport, J. (2000). Initiation of eukaryotic DNA replication: origin unwinding and sequential
790 chromatin association of Cdc45, RPA, and DNA polymerase alpha. *Mol Cell* 5, 617-627.
791 Walter, J., Sun, L., and Newport, J. (1998). Regulated chromosomal DNA replication in the absence of a nucleus.
792 *Mol Cell* 1, 519-529.
793 West, S.C., and Chan, Y.W. (2018). Genome Instability as a Consequence of Defects in the Resolution of
794 Recombination Intermediates. *Cold Spring Harb Symp Quant Biol*.
795 Wuhr, M., Guttler, T., Peshkin, L., McAlister, G.C., Sonnett, M., Ishihara, K., Groen, A.C., Presler, M., Erickson,
796 B.K., Mitchison, T.J., *et al.* (2015). The Nuclear Proteome of a Vertebrate. *Curr Biol* 25, 2663-2671.
797 Wyatt, D.W., Feng, W., Conlin, M.P., Yousefzadeh, M.J., Roberts, S.A., Mieczkowski, P., Wood, R.D., Gupta, G.P.,
798 and Ramsden, D.A. (2016). Essential Roles for Polymerase theta-Mediated End Joining in the Repair of
799 Chromosome Breaks. *Mol Cell* 63, 662-673.
800 Ying, S., Minocherhomji, S., Chan, K.L., Palmai-Pallag, T., Chu, W.K., Wass, T., Mankouri, H.W., Liu, Y., and
801 Hickson, I.D. (2013). MUS81 promotes common fragile site expression. *Nat Cell Biol* 15, 1001-1007.

802

803 **FIGURE LEGENDS**

804 **Figure 1. Mitotic CDK triggers aberrant processing of stalled DNA replication**
805 **forks in *Xenopus* egg extracts**

806 **(A)** Schematic of experimental approach to test effect of B1-CDK1 on DNA replication.
807 APH, DNA polymerase inhibitor aphidicolin.

808 **(B)** A 3 kb pBlueScript plasmid was replicated according to (A) and products were
809 separated on a native agarose gel followed by autoradiography. Unless stated
810 otherwise, the '0 minute' time point refers to NPE addition.

811 **(C)** Schematic of DNA replication for LacR-bound p[*lacO*₄₈] plasmid.

812 **(D)** p[*lacO*₄₈] was replicated according to (C) under the indicated conditions.

813 **(E)** p[*lacO*₄₈] was replicated according to (C) in the absence or presence of LacR and
814 IPTG (10 mM, 15 min incubation in NPE before mixing with "licensing" mixture), as
815 indicated.

816 **(F)** Schematic of replication for pDPC, containing four 46 kDa M.HpaII DNA
817 methyltransferases at the indicated positions. Products formed in the presence and
818 absence of B1-CDK1 are indicated.

819 **(G)** pControl or pDPC was replicated according to (F) using the indicated conditions.

820 From (A) to (G), B1-CDK1 was added to "licensing" mixture at a concentration of 50
821 ng/μL and its final concentration in the overall reaction is 16.7 ng/μL (see method). RI,
822 replication intermediate; OC, open circle; SC: supercoil; θ, theta structure; ARP,
823 aberrant replication product.

824 See also **Figure S1**.

825

826 **Figure 2. Mitotic processing of stalled replication forks leads to complex DNA**
827 **rearrangements**

828 **(A)** Structure of the 4.6 kb p[*lacO*₄₈] plasmid. Numbers mark the length of the indicated
829 DNA segments in kilo-basepairs (kb).

830 **(B)** p[*lacO*₄₈] was replicated in the presence of Buffer or B1-CDK1. At the indicated time
831 points, replication products were isolated and digested with AlwNI and AflII, or AlwNI, as
832 indicated. Numbers label the size of linear fragments in kb; Y, double-Y or single-Y
833 structure (see panel C).

834 **(C)** Model explaining the restriction products observed in (B). Although the model favors
835 fork breakage on the leading strand, the possibility of fork breakage on the lagging
836 strand has not been excluded. A more detailed model is presented in Figure S2A.

837 **(D)** The smear of ~3-4 kb mitotic DNA replication products generated after AlwNI
838 digestion in (B) was self-ligated, cloned and sequenced. The controls are replication
839 products of the same plasmid from a mitotic reaction lacking LacR. The *lacO* repeats,
840 shown as white boxes, are separated by four unique spacers shown in different colors.
841 Inset, DNA sequences of the *lacO* repeat and four spacers. The detailed structure of the
842 entire *lacO* array is shown in Figure S2C.

843 **(E)** A model for the generation of product h in (D) from multiple template-switching
844 events.

845 See also **Figure S2**.

846

847 **Figure 3. Depletion of DNA polymerase θ disrupts the generation of aberrant**
848 **replication product in the presence of mitotic CDK**

849 (A) Mock-depleted and Polθ-depleted *Xenopus* egg extracts were blotted for Polθ and
850 MCM7, alongside a serial dilution of mock-depleted extracts. Asterisk, background
851 band.

852 (B) LacR-bound p[*lacO*₄₈] was replicated in mock-depleted or Polθ-depleted extracts
853 with or without B1-CDK1 treatment. Total DNA replication and ARP were quantified in
854 Figure S3F.

855 (C) pDPC was replicated in mock-depleted or Polθ-depleted egg extracts with or without
856 B1-CDK1 treatment. Total DNA replication and ARP were quantified in Figure S3G.

857 (D) Structure of clones derived from mitotic ARPs in mock- or Polθ-depleted extracts.
858 LacR-bound p[*lacO*₄₈] was replicated in mock- or Polθ-depleted extracts with B1-CDK1
859 treatment. The smear of ~3-4 kb mitotic DNA replication products generated after AlwNI
860 digestion was self-ligated, cloned and sequenced. Elements in the box at the bottom
861 show the sequences of *lacO* and spacers.

862 (E) Comparison of mitotic ARP-derived clones in the presence or absence of Polθ.
863 Mock depletion (Figure 2D) and Polθ depletion (Figure S3H) in experiment 1 (Exp. 1)
864 were performed independently whereas they were performed side by side (Figure 3D) in
865 experiment 2 (Exp. 2). The shown *p*-value was from unpaired two-tailed Student's *t*-test.
866 In (B) and (C), OC, open circle; SC, supercoil; θ, theta structure; ARP, aberrant
867 replication product.

868 See also **Figure S3**.

869

870 **Figure 4. Mitotic CDK-induced fork collapse requires p97-dependent CMG**
871 **unloading**

872 **(A)** LacR-bound p[*lacO*₄₈] plasmid was replicated and treated as schemed. Chromatin-
873 bound proteins were recovered and blotted with the indicated antibodies. Red bracket,
874 ubiquitylated MCM7. Histone H3 served as loading control. Note that the MCM7
875 antibody cross-reacts with USP21.

876 **(B)** LacR-bound p[*lacO*₄₈] was replicated in the presence or absence of p97-i and B1-
877 CDK1, as indicated. OC, open circle; SC: supercoil; θ , theta structure; ARP, aberrant
878 replication product.

879 **(C)** pDPC was replicated in the presence or absence of p97-i and B1-CDK1, as
880 indicated. ARP, OC+SC and overall DNA replication were quantified in Figure S4G.

881 **(D)** Effect of ATR inhibition on stalled replication forks. LacR-bound p[*lacO*₄₈] plasmid
882 was replicated as schemed. Final concentration of ATR inhibitor (ATR-i; ETP-46464) in
883 the reactions was 200 μ M. Extracts with [α -³²P]-dATP were sampled to track DNA
884 replication while extracts without [α -³²P]-dATP were sampled in parallel to track CHK1-
885 S345 phosphorylation (CHK1-pS345), γ -H2AX. Histon H3 was included as loading
886 control.

887 **(E)** LacR-bound p[*lacO*₄₈] plasmid was replicated and treated as in (A). The final
888 concentrations of PLK1 inhibitor (PLK1-i, BI-2536) and Aurora kinase A inhibitor
889 (AURKA-i, MLN-8237) were 50 μ M and 10 μ M, respectively. DMSO and p97-i
890 treatments were included as controls. Chromatin-bound proteins were recovered and
891 blotted with the indicated antibodies.

892 **(F)** LacR-bound p[*lacO*₄₈] was replicated as schemed. PLK1-i was added 10 minutes
893 before B1-CDK1 treatment, with a final concentration of 50 μ M in the overall reaction.

894 **(G)** LacR-bound p[*lacO*₄₈] was replicated in the presence of PLK1-i or AURKA-i, as
895 schemed in (F). The final concentrations of PLK1-i and AURKA-i were 50 μM and 10
896 μM, respectively.

897 See also **Figure S4**.

898

899 **Figure 5. E3 ubiquitin ligase TRAIIP promotes mitotic CMG unloading from a**
900 **stalled replication fork**

901 **(A)** Mock-depleted and TRAIIP-depleted egg extracts were blotted for TRAIIP and MCM7
902 alongside a serial dilution of mock-depleted extracts.

903 **(B)** LacR-bound p[*lacO*₄₈] plasmid was replicated in mock-depleted or TRAIIP-depleted
904 egg extracts and treated as schemed. Chromatin-bound proteins were recovered and
905 blotted with the indicated antibodies.

906 **(C)** LacR-bound p[*lacO*₄₈] was replicated in mock-depleted or TRAIIP-depleted extracts
907 with or without B1-CDK1 treatment.

908 **(D)** LacR-bound p[*lacO*₄₈] was replicated in mitotic mock-depleted or TRAIIP-depleted
909 egg extracts with or without recombinant wildtype TRAIIP (rTRAIIP^{WT}) or R18C mutant
910 (rTRAIIP^{R18C}), as indicated. rTRAIIP^{WT} and rTRAIIP^{R18C} were added to NPE at a
911 concentration of 21 ng/μL (~7-fold over endogenous TRAIIP, see quantification in Figure
912 S5C). Matched buffer without recombinant protein was added to control reactions.
913 Addition of rTRAIIP^{WT} at endogenous level (S5C) into TRAIIP-depleted extracts also led
914 to substantial rescue of mitotic ARPs (Figures S5D and S5E).

915 See also **Figure S5**.

916

917 **Figure 6. TRAIP mediates unloading of terminated CMGs in mitosis**

918 **(A)** p[*lacO*₄₈] plasmid, in the absence of LacR, was replicated and treated as schemed.
919 Chromatin-bound proteins were recovered and blotted with the indicated antibodies.
920 Red brackets indicate the levels of MCM7 ubiquitylation.

921 **(B)** p[*lacO*₄₈] plasmid, in the absence of LacR, was replicated in mock-depleted or
922 TRAIP-depleted egg extracts supplemented with or without rTRAIP^{WT} (~4-fold of
923 endogenous TRAIP), or rTRAIP^{R18C} (~9-fold of endogenous TRAIP), followed by
924 indicated treatments. Chromatin-bound proteins were recovered and blotted with the
925 indicated antibodies.

926 **(C)** Illustration of the first cell cycle of the *C. elegans* embryo. Following S-phase, the
927 female and male pronuclei migrate towards each other and chromosomes condense
928 during prophase. Subsequently, the two sets of chromosomes intermingle during
929 metaphase.

930 **(D)** Timelapse video microscopy of the first embryonic mitosis, in embryos exposed to
931 the indicated RNAi and expressing GFP-PSF-1 and mCherry-HistoneH2B. The female
932 pronucleus is shown during early prophase, before convergence with the male
933 pronucleus (mid and late prophase). The arrows indicate examples of persistence of
934 GFP-PSF-1 on condensed chromatin during mitosis. Scale bar, 5 μ m.

935 **(E-F)** Worms in which the PSF-1 subunit of the CMG helicase was tagged with GFP
936 were subjected to the indicated RNAi treatment. GFP-PSF-1 was recovered by
937 immunoprecipitation, and the association of the indicated proteins was then monitored
938 by immunoblotting against the indicated proteins (E) or ubiquitin (F).

939 See also **Figure S6**.

940

941 **Figure 7. Model of CMG unloading, fork breakage and complex DNA**
942 **rearrangements upon premature mitotic entry**

943 When a replication fork encounters a replication barrier (indicated as a red hexagonal
944 STOP sign), the replisome containing CMG and TRAIP is stably stalled during
945 interphase. With the increase of mitotic CDK activity, E3 ubiquitin ligase TRAIP is
946 activated (directly or indirectly) to cause CMG ubiquitylation on MCM7 subunit, which in
947 turn triggers CMG unloading from chromatin by CDC48/p97 ATPase. Loss of CMG
948 leads to incision by so far unknown DNA nuclease(s), followed by error-prone double-
949 strand repair by MMEJ and/or SSA, which results in DNA rearrangements such as
950 deletions and insertions from template-switching events.

951 See also **Figure S7**.

952 **METHODS**

953 No statistical methods were used to predetermine sample size. All experiments were
954 performed at least twice independently using separate preparations of *Xenopus* egg
955 extracts. A representative result is shown.

956

957 **Protein purification.** To purify biotinylated LacR, the LacR-Avi expressing plasmid
958 pET11a[LacR-Avi] (Avidity, Denver, CO) and biotin ligase expressing plasmid pBirAcm
959 (Avidity, Denver, CO) were co-transformed into T7 Express cells (New England
960 Biolabs). Cultures were supplemented with 50 mM biotin (Research Organics,
961 Cleveland, OH). Expression of LacR-Avi and the biotin ligase was induced by addition
962 of IPTG (Isopropyl β -D-thiogalactoside, Sigma, St. Louis, MO) to a final concentration of
963 1 mM. Biotinylated LacR-Avi was then purified as described (Dewar et al., 2015). BRC
964 (a ~35 amino acid peptide derived from BRCA2 that binds RAD51) and BRC*** (BRC
965 peptide with mutations at RAD51 binding sites), a gift of K. Vrtis, were purified as
966 reported (Long et al., 2011). rTRAIP and rTRAIP-R18C were expressed from a 6xHis-
967 SUMO plasmid in bacteria and purified as described (Wu et al. in revision). Other
968 proteins used in this study were Cyclin B1-CDK1 (Life Technologies Cat #PR4768C and
969 EMD Millipore Cat #14-450M), Cyclin A2 (Creative Biomart, Cat #CCNA2-6798H) and
970 Cyclin E-CDK2 (EMD Millipore Cat #14-475). USP21 was a gift from D. Finley.

971

972 **DNA constructs.** The 4.6 kb p[*lacO*₄₈] plasmid (a generous gift of K. Vrtis) contains an
973 array of 48 *lacO* sites which can be bound by the *lac* repressor (LacR) to form
974 replication barriers. The pDPC plasmid (4.3 kb), a generous gift of J. Sparks, was

975 constructed based on a previous protocol (Duxin et al., 2014). Control plasmid (pControl)
976 used in Figure 1G has the same DNA sequence as pDPC, but lacks crosslinks.

977

978 ***Xenopus* egg extracts and DNA replication.** Egg extracts were prepared using
979 *Xenopus laevis* (Nasco Cat #LM0053MX). All experiments involving animals were
980 approved by the Harvard Medical School Institutional Animal Care and use Committee
981 (IACUC) and conform to relevant regulatory standards. *Xenopus* egg extracts including
982 Low Speed Supernatant (LSS), High Speed Supernatant (HSS), and Nucleoplasmic
983 egg extract (NPE) were prepared as described (Blow and Laskey, 1986; Lebofsky et al.,
984 2009).

985 To assess the effects of mitotic cyclins, demembranated sperm chromatin from
986 *Xenopus laevis* males was incubated in LSS (4,000 sperms/ μ L LSS) for 40 minutes at
987 room temperature to form nuclei. The reactions were subsequently incubated with a
988 range of concentrations of mitotic B1-CDK1. Nuclear envelope integrity and chromatin
989 condensation were monitored by microscopy after Hoechst staining (see below). The
990 concentration (50 ng/ μ L) that triggered nuclear envelopment breakdown and
991 chromosome condensation was chosen to trigger mitotic entry in subsequent
992 experiments.

993 For interphase DNA replication, sperm chromatin or plasmid DNA was first
994 incubated in HSS (final concentration of 7.5-15.0 ng DNA/ μ L HSS) for 30 minutes at
995 room temperature to license the DNA for replication (“licensing”), followed by the
996 addition of 2 volumes of NPE to initiate CDK2-dependent replication. To radiolabel the
997 nascent strands during replication, NPE was supplemented with trace amounts of [α -

998 ³²P]-dATP. Mitotic DNA replication was performed essentially as described (Prokhorova
999 et al., 2003). Briefly, after 30 minutes, 0.9 volumes of licensing reaction was incubated
1000 with 0.1 volumes of mitotic B1-CDK1 for 30 minutes at room temperature, followed by
1001 addition of 2 volumes of NPE. In the “licensing” mixture, the concentration of B1-CDK1
1002 was 50 ng/μL, and its concentration in the final replication reaction was 16.7 ng/μL.
1003 Unless stated otherwise, the ‘0 minute’ time point refers to the moment of NPE addition.
1004 2 μL aliquots of replication reaction were stopped with 5 μl of stop solution A (5% SDS,
1005 80 mM Tris pH8.0, 0.13% phosphoric acid, 10% Ficoll) supplemented with 1 μl 20
1006 mg/ml Proteinase K (Roche, Nutley, NJ). Samples were incubated for 1 hour at 37°C
1007 prior to electrophoresis on a 0.9% native agarose gel. Gels were dried and radioactivity
1008 was detected using a phosphorimager (Lebofsky et al., 2009).

1009 To induce replication fork stalling using LacR, one volume of p[*lacO*₄₈] (200
1010 ng/μL) was incubated with one volume of recombinant LacR (36 μM) for 45-60 minutes
1011 at room temperature. Next, 0.1 volumes of the mixture was combined with 0.9 volumes
1012 of HSS for licensing, followed by addition of 2 volumes of NPE for initiation of
1013 replication. To inhibit the binding of LacR to the *lacO* array, IPTG was added to NPE to
1014 a final concentration of 10 mM and incubated for 15 minutes prior to use in replication
1015 (Figure 1E) or added into replication reactions after fork stalling (Figures S4H and S6C)
1016 at the indicated time.

1017 For replication assays with inhibitors, NPE was supplemented with inhibitors for
1018 15 minutes at room temperature before addition to the licensing mixture. Inhibitors were
1019 used at the following final concentrations in replication reaction: Aphidicolin (Sigma Cat
1020 #A0781-5MG), 2.2 μM or 0.97 μM, as indicated; CDC7 inhibitor PHA-767491 (Sigma

1021 Cat #PZ0178), 266 μ M; p97 inhibitor NMS-873 (Sigma Cat #SML1128-5MG), 266 μ M;
1022 DNA-PKcs inhibitor NU-7441, 133 μ M; BRC or BRC^{***}, 1 μ g/ μ L; Cullin inhibitor MLN-
1023 4924 (Active Biochem Cat #A-1139), 266 μ M; PLK1 kinase inhibitor BI-2536 (Adooq Cat
1024 #A10134, 50 μ M; Aurora A kinase inhibitor MK-5108 (Selleck Cat #S2770), 10 μ M and
1025 ATR inhibitor (ETP-46464; Sigma Cat #SML1321) , 200 μ M. For the CDK1 inhibition
1026 assay in Figure S1G, CDK1 inhibitor RO-3306 (EMD Millipore Cat #217699-5MG) was
1027 incubated with the replication reaction containing stalled replication forks for 5 minutes
1028 before the addition of B1-CDK1.

1029

1030 **Immunodepletion and Western blotting.** Immunodepletions using antibodies against
1031 *Xenopus laevis* FANCD2 (Knipscheer et al., 2009), FANCI (Duxin et al., 2014), SMC2
1032 (antigen: Ac-CSKTKERRNRMEVDK-OH, New England Peptide), TRAIIP (antigen: Ac-
1033 CTSSLANQPRLEDFLK-OH, New England Peptide), Pol θ (antigen: residues 1212 to
1034 1506, Abgent), and RAD51 (Long et al., 2011) were performed as described previously
1035 (Budzowska et al., 2015). Briefly, Protein A Sepharose Fast Flow beads (GE
1036 Healthcare) were incubated with antibodies at 4°C overnight. For mock depletion, an
1037 equivalent quantity of nonspecific rabbit IgGs was used. Five volumes of pre-cleared
1038 HSS or NPE were then mixed with one volume of the antibody-bound sepharose beads.
1039 For FANCI-D2 depletion of HSS and NPE, two rounds of depletion using both FANCI
1040 and FANCD2 antibodies were performed at room temperature for 20 minutes each.
1041 Depletions for other proteins were performed at 4°C, with two rounds for HSS and three
1042 rounds for NPE. For each round, a mixture of antibody-bound beads and egg extract
1043 was rotated on a wheel for 40 minutes. Immunodepleted extracts were collected and

1044 used immediately for DNA replication. Depletion efficiency was assessed by Western
1045 blotting. Western blots from depletion or plasmid/sperm chromatin pull-downs were
1046 probed using antibodies against SMC2, TRAIIP, FANCI (Duxin et al., 2014), FANCD2
1047 (Knipscheer et al., 2009), MCM7 (Dewar et al., 2017), MCM6 (Dewar et al., 2017),
1048 RAD51 (Long et al., 2011), ORC2 (Dewar et al., 2017), CDC45 (Walter and Newport,
1049 2000), SLD5 (Dewar et al., 2017), CHK1-pS345 (Cell Signaling Technology Cat
1050 #2348S), γ -H2AX (Cell Signaling Technology Cat #2577S) and Histone H3 (Cell
1051 Signaling Technology Cat #9715S).

1052

1053 **Sperm chromatin spin-down assay.** Sperm chromatin spin-down was performed as
1054 previously described (Raschle et al., 2015). Briefly, chromatin and associated proteins
1055 were isolated by centrifugation through a sucrose cushion, washed three times,
1056 resuspended in 2x SDS sample buffer (100 mM Tris pH 6.8, 4% SDS, 0.2%
1057 bromophenol blue, 20% glycerol, 10% β -mercaptoethanol) and boiled at 95°C for 3-5
1058 minutes. In Figure S3A, chromatin was spun down 20 minutes after NPE addition for the
1059 Buffer control and at 9 minutes after NPE addition for the B1-CDK1 treatment (final
1060 concentration, 16.7 ng/ μ L), at which point replication was ~50% complete for both
1061 reactions. In Figure S1D, chromatin and associated proteins were isolated from HSS.

1062

1063 **Plasmid pull-down assay.** Plasmid pull-down assays were performed as described
1064 (Budzowska et al., 2015). Briefly, streptavidin-coupled magnetic beads (Dynabeads M-
1065 280, Invitrogen; 6 μ l beads slurry per pull-down) were washed three times with wash
1066 buffer 1 (50 mM Tris pH 7.5, 150 mM NaCl, 1 mM EDTA pH 8, 0.02% Tween-20).

1067 Biotinylated LacR was incubated with the beads (12 pmol per 6 μ L beads) at room
1068 temperature for 40 min. The beads were then washed four times with pull-down buffer 1
1069 (10 mM Hepes pH 7.7, 50 mM KCl, 2.5 mM MgCl₂, 250 mM sucrose, 0.25 mg/mL BSA,
1070 0.02% Tween-20) and resuspended in 40 μ L of the same buffer. At the indicated times,
1071 4 μ L samples of the replication reaction were withdrawn and gently mixed with Biotin-
1072 LacR-coated beads. The suspension was immediately placed on a rotating wheel and
1073 incubated for 30-60 minutes at 4°C. The beads were washed three times with wash
1074 buffer 2 (10 mM Hepes pH 7.7, 50 mM KCl, 2.5 mM MgCl₂, 0.25 mg/mL BSA, 0.03%
1075 Tween-20). The beads were resuspended in 40 μ L of 2 \times SDS sample buffer and boiled
1076 at 95°C for 3-5 minutes. Chromatin-bound proteins were separated by SDS-PAGE and
1077 analyzed by Western blotting.

1078

1079 **De-ubiquitination assay** Plasmid pull-downs were performed as described above,
1080 except that after the wash steps with wash buffer 2, chromatin-bound proteins were
1081 resuspended in 20 μ L of USP21 buffer (150 mM NaCl, 10 mM DTT, 50mM Tris pH 7.5)
1082 and split into two 10 μ L aliquots. Each aliquot was incubated with the non-specific
1083 deubiquitinase USP21 or buffer at 37°C for 60 minutes. The reactions were stopped by
1084 addition of 2x SDS sample buffer and boiled at 95°C for 3-5 minutes.

1085

1086 **Restriction digestion.** 2 μ L aliquots of replication reactions were stopped in 20 μ L of
1087 stop solution B (50 mM Tris pH 7.5, 0.5% SDS, 25 mM EDTA), and replication products
1088 were purified as previously described (Raschle et al., 2008). Purified products were
1089 digested with restriction enzymes as *per* the manufacturer's instructions. Digestion

1090 reactions were stopped in 0.5 volumes of stop solution C (5% SDS, 4 mg/mL Proteinase
1091 K) and incubated for 60 minutes at room temperature. Digested products were
1092 separated on a 1% native agarose gel and visualized by autoradiography.

1093

1094 **Sequencing.** LacR-bound p[*lacO₄₈*] plasmid was replicated in the presence of mitotic
1095 B1-CDK1 for 120 minutes. Replication products were purified and digested with AlwNI
1096 (single cut on the parental DNA) for 60 minutes at 37°C, as described above. After
1097 separation on a 0.9% native agarose gel, bands smaller than the 4.6 kb full-length linear
1098 fragment were extracted and self-ligated with T4 DNA ligase. The ligation products were
1099 transformed into *E.coli* DH5α or XL1-Gold. As a control, p[*lacO₄₈*] was replicated without
1100 LacR for 120 minutes in the presence of B1-CDK1. Replication products (containing
1101 only open circular and supercoiled species) were processed as above, and the only
1102 band (4.6 kb) after AlwNI restriction was purified for cloning. Clones from both
1103 treatments were sequenced by Sanger method with Forward primer: 5'-
1104 AAGGCGATTAAGTTGGGTAA-3' and Reverse primer: 5'-
1105 CATGTTCTTTCCTGCGTTATCCCCTGA-3'.

1106

1107 **C. elegans maintenance.** The *C. elegans* strains were maintained according to
1108 standard procedures (Brenner, 1974) and were grown on 'Nematode Growth Medium'
1109 (NGM: 3 g/l NaCl; 2.5 g/l peptone; 20 g/l agar; 5 mg/l cholesterol; 1 mM CaCl₂; 1 mM
1110 MgSO₄; 2.7 g/l KH₂PO₄; 0.89 g/l K₂HPO₄). The following worm strains were used:

1111 KAL1: *psf-1(lab1[gfp::TEV::S-tag::psf-1 + loxP unc-119(+)] loxP]*

1112 KAL3: *psf-1(lab1); ItIs37[pie-1p::mCherry::his-58 + unc-119(+)]*

1113 TG1754: *unc-119(ed3) III; gtlIs65[pie-1p::gfp::cdc-45 + unc-119(+)]*; *ItIs37*

1114

1115 **RNA interference.** RNAi was performed by feeding worms with RNase III-deficient
1116 HT115 bacteria transformed with an L4440-derived plasmid that express double-
1117 stranded RNA (Timmons and Fire, 1998). For microscopy experiments, bacterial culture
1118 grown to OD600=1 was supplemented with 1mM IPTG to express dsRNA. 400 ml of
1119 bacteria were loaded onto a 6cm RNAi plates (3 g/l NaCl, 20 g/l agarose, 5 mg/l
1120 cholesterol, 1 mM CaCl₂, 1 mM MgSO₄, 2.7 g/l KH₂PO₄, 0.89 g/l K₂HPO₄, 1 mM IPTG
1121 and 100 mg/l Ampicillin) and the plate was incubated overnight at room temperature.
1122 For each immunoprecipitation, 0.5 ml of bacterial pre-culture grown overnight was used
1123 to inoculate a 400 ml culture in 'Terrific Broth' (12 g l⁻¹ tryptone, 24 g l⁻¹ yeast extract,
1124 9.4 g l⁻¹ K₂HPO₄, 2.2 g l⁻¹ KH₂PO₄, adjusted to pH 7). After 7 h of growth in a baffled
1125 flask at 37 °C with agitation, expression of dsRNA was induced overnight at 20 °C by
1126 addition of 3 mM IPTG and the bacteria were pelleted. 8 g of bacterial pellet was
1127 resuspended with 2 ml buffer (M9 medium supplemented with 75 mg l⁻¹ cholesterol;
1128 100 mg l⁻¹ ampicillin; 50 mg l⁻¹ tetracycline; 12.5 mg l⁻¹ amphotericin B; 3 mM IPTG)
1129 and spread on a 15cm plate containing NGM supplemented with 1 mM IPTG and
1130 100 mg l⁻¹ ampicillin.

1131 The plasmids expressing dsRNA were made by cloning PCR products amplified
1132 from cDNA into the vector L4440. *Irr-1* fragment was obtained with the primers
1133 ATGCGATTACCATGTGAAGTGG and CCTCGTGTGTGTATTTCGATATTATC; *npl-4*
1134 fragment with GTCCAAAAGGGCCCAACTGTC and CCAGCAGGAACATCCACCAGC;
1135 *B0432.13* (*trul-1*) with ATGACGTCACAGCCCACGTCATC and
1136 CGTATTCCGTAAGATTCGACGTA. To target *Irr-1* and *B0432.13* simultaneously, DNA

1137 fragments from each gene were cloned contiguously into a single L4440 plasmid. The
1138 empty L4440 plasmid was used as control.

1139

1140 **Microscopy.** Worms at the larval L4 stage were incubated on 6 cm RNAi feeding plates
1141 for 30-34 hours at 25°C. Embryos were dissected in M9 medium (6 g/l Na₂HPO₄, 3 g/l
1142 KH₂PO₄, 5 g/l NaCl, 0.25 g/l MgSO₄) and mounted on a 2% agarose pad. Time lapse
1143 images were then recorded at 23–24°C using an Olympus IX81 microscope (MAG
1144 Biosystems) with a CSU-X1 spinning-disk confocal imager (Yokogawa Electric
1145 Corporation), a Cascade II camera (Photometrics) and a 60X/1.40 Plan Apochromat oil
1146 immersion lens (Olympus). Images were captured every 10 seconds using MetaMorph
1147 software (Molecular Devices) and processed with ImageJ software (National Institutes
1148 of Health) as previously described (Sonneville et al., 2017).

1149

1150 **Extracts of worm embryos and immunoprecipitation of protein complexes.**

1151 Preparation of worm extracts and immunoprecipitation of GFP-PSF-1 was performed as
1152 previously described (Sonneville et al., 2017). Briefly, 1 ml of a synchronized population
1153 of L4 worms expressing GFP-PSF-1 were fed for 50 h at 20 °C on a 15 cm RNAi plate,
1154 supplemented with 8 g of bacterial pellet (see above). After feeding, the worms were
1155 washed in M9 medium and then disrupted in ‘bleaching solution’ (for 100 ml: 36.5 ml
1156 H₂O, 45.5 ml 2 N NaOH and 18 ml ClNaO 4%), before washing of the resulting embryo
1157 preparation in M9 medium.

1158 At 4 °C, embryos were washed twice with lysis buffer (100 mM HEPES-KOH pH
1159 7.9, 50 mM potassium acetate, 10 mM magnesium acetate, 2 mM EDTA), and then
1160 resuspended in three volumes of lysis buffer that was supplemented with 2 mM sodium

1161 fluoride, 2 mM sodium β -glycerophosphate pentahydrate, 1 mM dithiothreitol (DTT), 1%
1162 Protease Inhibitor Cocktail (P8215, Sigma-Aldrich), and 1 \times 'Complete Protease Inhibitor
1163 Cocktail' (05056489001, Roche). The washed embryo suspension was then snap
1164 frozen drop-wise in liquid nitrogen and stored at -80°C . Subsequently, ~ 2.5 g of frozen
1165 embryos was ground in a SPEX SamplePrep 6780 Freezer/Mill. After thawing, we
1166 added a one-quarter volume of 'glycerol-mix' buffer (lysis buffer supplemented with 50%
1167 glycerol, 300 mM potassium acetate, 0.5% detergent IGEPAL CA-630, protease
1168 inhibitors, and DTT at the concentrations mentioned above). De-ubiquitylase enzymes
1169 were inhibited by addition of $5\ \mu\text{M}$ propargylated ubiquitin (Ubi-PrG; MRC PPU,
1170 Dundee), and chromosomal DNA was digested with 1,600 U of Pierce Universal
1171 Nuclease (123991963, Fisher) for 30 min at 4°C . Extracts were centrifuged at 25,000 \times
1172 g for 30 min and then for 100,000 \times g for 1 h, before pre-incubation with agarose beads
1173 (0.4 ml slurry) for 45 min. Samples of each extract were taken and combined with
1174 Laemmli buffer, before storage at -80°C . The remainder was then incubated for 90 min
1175 with 40 μl of GFP-Trap_A beads (Chromotek). The beads were washed four times with
1176 1 ml of wash buffer (100 mM HEPES-KOH pH 7.9, 100 mM potassium acetate, 10 mM
1177 magnesium acetate, 2 mM EDTA, 0.1% IGEPAL CA-630, 2 mM sodium fluoride, 2 mM
1178 sodium β -glycerophosphate pentahydrate, plus protease inhibitors as above). Finally,
1179 the bound proteins were eluted at 95°C for 5 min in 100 μl of 1 \times Laemmli buffer and
1180 stored at -80°C .

1181 **Data quantification.** Autoradiographs and Western blots were quantified using ImageJ
1182 1.48v (National Institute of Health). The quantification methods for individual results are
1183 described in the figure legends.

1185 **SUPPLEMENTAL FIGURE LEGENDS**

1186 **Figure S1, related to Figure 1.**

1187 **(A)** To determine the concentration of mitotic B1-CDK1 that efficiently induces nuclear
1188 envelope breakdown and chromatin condensation, de-membranated *Xenopus* sperm
1189 chromatin was incubated in LSS (low speed supernatant) for 40 minutes to allow the
1190 formation of pseudo nuclei. The indicated final concentrations of B1-CDK1 were then
1191 added into the reactions for 30 minutes before Hoechst staining and imaging. 50 ng/ μ L
1192 of B1-CDK1 was sufficient to induce nuclear envelope breakdown and chromatin
1193 condensation and it was used for subsequent experiments unless otherwise indicated.
1194 Scale bar, 10 μ m.

1195 **(B)** Percentage of intact nuclei remaining at the indicated time points after treatment
1196 with the indicated concentration of B1-CDK1 (n>1,000). The '0 minute' time point refers
1197 to Buffer or B1-CDK1 addition. The value at each time point was normalized to the
1198 value at 0 minute in each treatment.

1199 **(C)** Chromatin condensation assay in membrane-free HSS. Sperm chromatin was
1200 incubated in HSS for 30 minutes, and then treated with 50 ng/ μ L of B1-CDK1 for 30
1201 minutes followed by Hoechst staining and imaging. Scale bar, 10 μ m.

1202 **(D)** Sperm chromatin spin-down assays in HSS. Sperm chromatin was incubated with
1203 HSS for 30 minutes and treated with Buffer or 50 ng/ μ L of B1-CDK1 for another 30
1204 minutes. Chromatin DNA was recovered and chromatin-bound proteins were blotted
1205 with indicated antibodies. Unrelated lanes were cropped as indicated by the gap.

1206 **(E)** Plasmid pull-down assays in HSS. pBlueScript (3 kb) was incubated with HSS at a
1207 concentration of 7.5 ng/ μ L for 30 minutes and treated with Buffer or 50 ng/ μ L of B1-

1208 CDK1 for another 30 minutes. Plasmid was recovered and chromatin-bound proteins
1209 were blotted with indicated antibodies. Unrelated lanes were cropped as indicated by
1210 the gap.

1211 **(F)** Plasmid pull-down assay to assess origin firing. pBlueScript was incubated with HSS
1212 for 30 minutes and treated with buffer or 50 ng/ μ L of B1-CDK1 for another 30 minutes
1213 before addition of NPE. The p97 inhibitor NMS-873 (p97-i) was added into NPE (final
1214 concentration, 266 μ M) and incubated for 15 minutes. Treatment of p97-i blocked the
1215 unloading of CMG helicases from chromatin and trapped ubiquitylated MCM7 on
1216 chromatin, seen as a smear. Right panel shows the quantification of the CDC45 and
1217 Histone H3 signals. Increased CDC45 loading with B1-CDK1 treatment suggested more
1218 origin firing.

1219 **(G)** LacR-bound p[*lacO*₄₈] was replicated in interphase egg extracts for 60 minutes and
1220 then treated with DMSO or CDK1 kinase inhibitor (CDK1-i, 333 μ M RO-3306) for 5
1221 minutes before the addition of Buffer or 50 ng/ μ L of B1-CDK1. At the indicated times,
1222 samples were withdrawn and replication products were tracked by electrophoresis and
1223 autoradiography. ARP, aberrant replication product; θ , theta structure.

1224 **(H)** LacR-bound p[*lacO*₄₈] was replicated in the presence of B1-CDK1, Cyclin A2 and
1225 cyclin E-CDK2, with a final concentration of 50 ng/ μ L, respectively. OC, open circle; SC,
1226 supercoil; θ , theta structure; ARP, aberrant replication product.

1227

1228 **Figure S2, related to Figure 2.**

1229 **(A)** Model for mitotic processing of replication forks stalled by *lacO*-LacR barriers,
1230 explaining the restriction analysis (Figure 2B) and sequencing data (Figure 2D). After

1231 replication fork stalling, B1-CDK1 induces fork collapse and double-strand breaks
1232 (DSBs) at the edges of the *lacO* array. The broken DNA ends, with certain number of
1233 *lacO* repeats or microhomology, lead to either intra- or inter-molecular end joining. Inter-
1234 molecular end joining generates the aberrant replication products (ARPs). The initial
1235 end joining products can also be subject to cycles of fork collapse and end joining.
1236 Outcomes other than those illustrated here are possible but may not be detected
1237 because our sequencing strategy depends on the ability to recover plasmids by cloning.
1238 Although it has not been addressed whether the leading or lagging strand templates
1239 break, the results on CMG unloading (see below and text for details) favor leading
1240 strand breakage.

1241 **(B)** Schematic of B1-CDK1-induced fork breakage at different locations in the *lacO*
1242 array. Breakage at the outer edges (left) and joining of the resulting one-ended breaks
1243 creates large deletions of the array, whereas breakage closer to the midpoint of the
1244 array causes smaller deletions (right).

1245 **(C)** Sequence and structure of the 48 *lacO* repeats in p[*lacO*₄₈]. Each *lacO* repeat is in
1246 italic. Unique spacer sequences between *lacO* repeats are labeled in red, green, purple
1247 and blue, respectively, as depicted in Figures 2D and 2E. The sequence in grey
1248 indicates a unique spacer in the middle of the *lacO* array. Sequencing primers used in
1249 Figure 2D are indicated.

1250

1251 **Figure S3, related to Figure 3.**

1252 **(A)** B1-CDK1 treatment inhibits chromatin-loading of RAD51. Sperm chromatin was
1253 replicated in egg extracts and sampled when 50% replication was completed (20

1254 minutes for Buffer and 9 minutes for B1-CDK1). To inhibit DNA replication, CDC7
1255 inhibitor (CDC7-i, 399 μ M of PHA-767491) was added to NPE and incubated for 15
1256 minutes. Chromatin-bound proteins were recovered by chromatin spin-down and
1257 detected by blotting with indicated antibodies.

1258 **(B)** Mock-depleted and RAD51-depleted egg extracts were blotted with RAD51 and
1259 MCM7 antibodies. Serial dilutions of mock-depletion were used to assess the level of
1260 RAD51 depletion. Arrowhead indicates RAD51.

1261 **(C)** LacR-bound p[*lacO₄₈*] was replicated in mock-depleted or RAD51-depleted egg
1262 extracts in the absence or presence of B1-CDK1.

1263 **(D)** pBlueScript was replicated in egg extracts with the indicated treatments. BRC
1264 peptide binds and blocks RAD51's interaction with BRCA2, which prevents HR-
1265 mediated DSB repair. BRC*** peptide harbors three mutations at RAD51 binding sites
1266 and is unable to inhibit RAD51 (Long et al., 2011).

1267 **(E)** LacR-bound p[*lacO₄₈*] was replicated with the indicated treatments. To inhibit NHEJ,
1268 a DNA-PK inhibitor (DNA-PK-i, 133 μ M NU-7441) was added to NPE.

1269 **(F)** Quantification of overall DNA replication and ARP for Figure 3B.

1270 **(G)** Quantification of overall DNA replication and ARP for Figure 3C.

1271 **(H)** Structures of clones derived from mitotic ARPs in Pol θ -depleted egg extracts (Exp.
1272 1 in Figure 3E).

1273 In (C-E), ARP, aberrant replication product; θ , theta structure; OC, open circle; SC,
1274 supercoil; RI, replication intermediate.

1275

1276 **Figure S4, related to Figure 4.**

1277 **(A)** Mock-depleted and SMC2-depleted *Xenopus* egg extracts were blotted for SMC2
1278 and MCM7 alongside a serial dilution of mock-depleted extracts.

1279 **(B)** Effect of SMC2 depletion on B1-CDK1-induced chromatin condensation in HSS.
1280 Sperm chromatin was incubated in mock-depleted or SMC2-depleted HSS with Buffer
1281 or B1-CDK1 for 30 minutes prior to Hoechst staining and imaging. Regions with boxes
1282 were magnified on the right. Note the condensed chromosome in mock-depleted HSS
1283 with B1-CDK1 treatment (upper right image). Scale bar, 10 μ m.

1284 **(C)** LacR-bound p[*lacO*₄₈] was replicated in mock-depleted or condensin SMC2-
1285 depleted extracts with or without B1-CDK1 treatment.

1286 **(D)** pBlueScript was replicated in mock-depleted or SMC2-depleted egg extracts with a
1287 low dose of aphidicolin in the absence or presence of B1-CDK1. The absence of SMC2
1288 had no effect on mitotic ARP formation.

1289 **(E)** A time course to relate the timing of CMG unloading to replication fork collapse and
1290 ARP formation during replication with B1-CDK1. LacR-bound p[*lacO*₄₈] was replicated in
1291 egg extracts for 30 minutes before the addition of Buffer or B1-CDK1. Plasmid pull-
1292 downs were performed from “cold” reactions lacking radio-labeled nucleotides in parallel
1293 with “hot” reactions containing [α -³²P]-dATP. Plasmid pull-down samples were blotted
1294 for indicated proteins. Replication products were detected by autoradiography after gel
1295 electrophoresis. The red bracket indicates ubiquitylated MCM7, which is detectable
1296 before the appearance of the ARP. The black bracket marks potential collapsed
1297 replication forks with the B1-CDK1 treatment.

1298 **(F)** Effect of p97 inhibition on stalled replication forks in the presence or absence of B1-
1299 CDK1. LacR-bound p[*lacO*₄₈] plasmid was replicated in “hot” extracts with [α -³²P]-dATP

1300 to track DNA replication products and in “cold” extracts without [α -³²P]-dATP for plasmid
1301 pull-down to track CHK1-S345 phosphorylation (CHK1-pS345), γ -H2AX. Histon H3 was
1302 included as loading control. The final concentration of p97-i was 266 μ M.

1303 **(G)** Quantification of ARP, OC+SC, and overall DNA replication during replication of
1304 pDPC in Figure 4C.

1305 **(H)** Fork restart assay using IPTG to release LacR replication barrier. LacR-bound
1306 p[*lacO*₄₈] was replicated as schemed. The final concentration of IPTG was 10 mM. Note
1307 that IPTG had no effect on the B1-CDK1-induced ARP in the presence of DMSO (lanes
1308 13-24), whereas it almost fully restarted DNA synthesis in the presence of p97-i
1309 (compare lanes 31-35 with 25-30, and 19-24).

1310 In (C) (D), (F) and (H), RI, replication intermediate; ARP, aberrant replication product;
1311 OC, open circle; SC, supercoil; θ , theta structure.

1312

1313 **Figure S5, related to Figure 5.**

1314 **(A)** LacR-bound p[*lacO*₄₈] was replicated and treated as schemed. Chromatin-bound
1315 proteins were recovered and blotted with the indicated antibodies. IPTG was used to
1316 release LacR from *lacO* array therefore induce replication termination. Cul-i was used to
1317 inhibit CRL2^{Lrr1}-dependent CMG ubiquitylation during interphase replication termination.

1318 **(B)** pDPC was replicated in mock-depleted or TRAIP-depleted egg extracts in the
1319 presence or absence of B1-CDK1.

1320 **(C)** Serial dilutions of NPE and rTRAIP^{WT} purified from *E. coli* were blotted with TRAIP
1321 and MCM7 antibodies. Arrowhead marks TRAIP signal and asterisk indicates a
1322 background band in NPE. The concentration of TRAIP in NPE is 3.0-4.5 ng/ μ L.

1323 **(D-E)** LacR-bound p[*lacO₄₈*] (D) and pDPC (E) were replicated in mitotic mock-depleted
1324 or TRAIP-depleted egg extracts with or without rTRAIP^{WT} as indicated. rTRAIP^{WT} was
1325 added to NPE at endogenous level (3.6 ng/μL). Matched buffer was added to reactions
1326 without rTRAIP^{WT}.

1327 **(F)** LacR-bound p[*lacO₄₈*] was replicated in TRAIP-depleted extracts supplemented with
1328 6xHis-SUMO tagged rTRAIP of wildtype (WT) or truncation of PIP box (Δ PIP), as
1329 indicated. Both proteins were added ~5-10 folds of endogenous TRAIP in NPE and
1330 incubated for 15 minutes before they were used to drive DNA replication.

1331 **(G)** Mock-depleted and FANCI-D2-double depleted egg extracts were blotted with
1332 indicated antibodies. Serial dilution of mock-depleted extract was used to assess the
1333 level of FANCI-D2 depletion.

1334 **(H)** LacR-bound p[*lacO₄₈*] was replicated in mock-depleted or FANCI-D2-depleted egg
1335 extracts in the absence or presence of B1-CDK1. The depletion of FANCI-FANCD2 had
1336 no effect on ARP formation.

1337 In (B), (D), (F) and (H), ARP, aberrant replication product; θ , theta structure; OC, open
1338 circle; SC, supercoil.

1339

1340 **Figure S6, related to Figure 6.**

1341 **(A)** p[*lacO₄₈*], in the absence of LacR, was replicated in egg extracts used in Figures 6A
1342 and 6B. DNA replication was complete in 20 minutes. RI, replication intermediate; OC,
1343 open circle; SC, supercoil.

1344 **(B)** A 3.1 kb plasmid (pJD152 in (Dewar et al., 2015)) was replicated in mock-depleted
1345 or TRAIP-depleted extracts in the presence or absence of p97-i (to trap terminated and

1346 ubiquitylated CMGs on chromatin) followed by Buffer or B1-CDK1 treatment.
1347 Chromatin-bound proteins were recovered and blotted with indicated antibodies. Red
1348 brackets indicate the levels of MCM7 ubiquitylation. Note the dramatic smear of MCM7
1349 ubiquitylation in the presence of B1-CDK1 in mock (compare lanes 6 and 2) and the
1350 shrinkage with TRAIP depletion (compare lanes 14 and 6).

1351 **(C)** LacR-bound p[*lacO*₄₈] plasmid was replicated in mock-depleted or TRAIP-depleted
1352 egg extracts with or without recombinant rTRAIP^{WT} (~4-fold of endogenous TRAIP), or
1353 rTRAIP^{R18C} (~9-fold of endogenous TRAIP), and treated as schemed. Chromatin-bound
1354 proteins were recovered and blotted with the indicated antibodies.

1355 **(D)** Worm embryos expressing GFP-CDC-45 and mCherry-HistoneH2B were subjected
1356 to the indicated RNAi treatment. The images correspond to metaphase of the first
1357 embryonic cell cycle, and the arrows indicate persistence of GFP-CDC-45 on
1358 condensed chromatin. Scale bar, 5 μ m.

1359 **(E)** Comparison of different CMG unloading pathways. Mitotic CMG unloading at single
1360 stalled fork (i) occurs when a single stalled CMG on ssDNA enters mitosis (or in
1361 environment with high mitotic CDK activity). TRAIP is activated by mitotic CDK to trigger
1362 CMG ubiquitylation. Mitotic termination (ii) occurs when CRL2^{Lrr1} is deficient (Sonneville
1363 et al., 2017). CMGs at terminated replication forks are ubiquitylated upon mitotic entry in
1364 a TRAIP-dependent manner. During interphase ICL repair (iii) (Wu et al., in revision),
1365 when two CMGs on ssDNA converge at ICL, TRAIP is activated, independent of CDK1
1366 activity (data not shown) and promotes CMG ubiquitylation. During replication
1367 termination in interphase (iv), two CMGs bypass each other and translocate from
1368 ssDNA to dsDNA, triggering CRL2^{Lrr1}-dependent CMG ubiquitylation (Dewar et al.,

1369 2015; Dewar et al., 2017; Sonnevile et al., 2017). The cartoons highlight the
1370 requirement of E3 ubiquitin ligase activity rather than physical localization for CMG
1371 ubiquitylation. In contrast to CRL2^{Lrr1} which is specifically recruited to replisome during
1372 interphase replication termination, TRAP may travel with the replisome.

1373

1374 **Figure S7. Related to Figure 7**

1375 When replication forks stall on either side of a hard-to-replicate region (e.g. a common
1376 fragile site), entry into mitosis causes CMG unloading and efficient fork breakage.
1377 Because CMG binds the leading strand template, we propose that CMG unloading
1378 leads to breakage of both stalled forks on the leading strand templates (left pathway).
1379 One intact sister chromatid is rapidly restored by gap filling (dashed blue line). The other
1380 chromatid is restored by alternative end joining of the two broken ends, yielding sister
1381 chromatid exchange and a deletion that encompasses the segment of unreplicated
1382 DNA. Template switching before end joining could generate duplications at the
1383 breakpoint. In contrast, if stalled forks are broken randomly (right pathway),
1384 unproductive outcomes will be frequent, including the formation of acentric and dicentric
1385 isochromosomes (shown). Furthermore, if only one fork is broken, acentric arms can be
1386 generated (not shown).

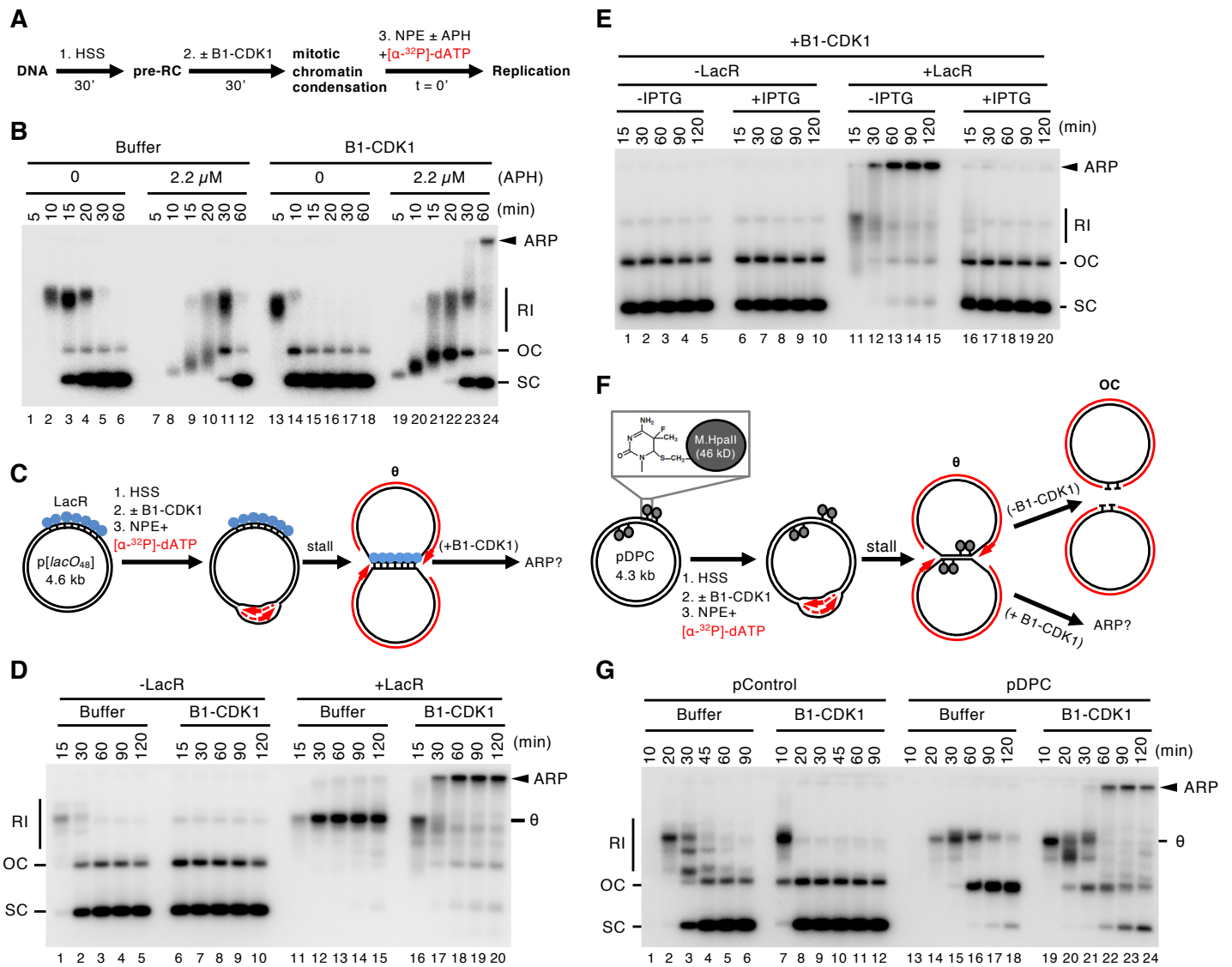


Figure 1

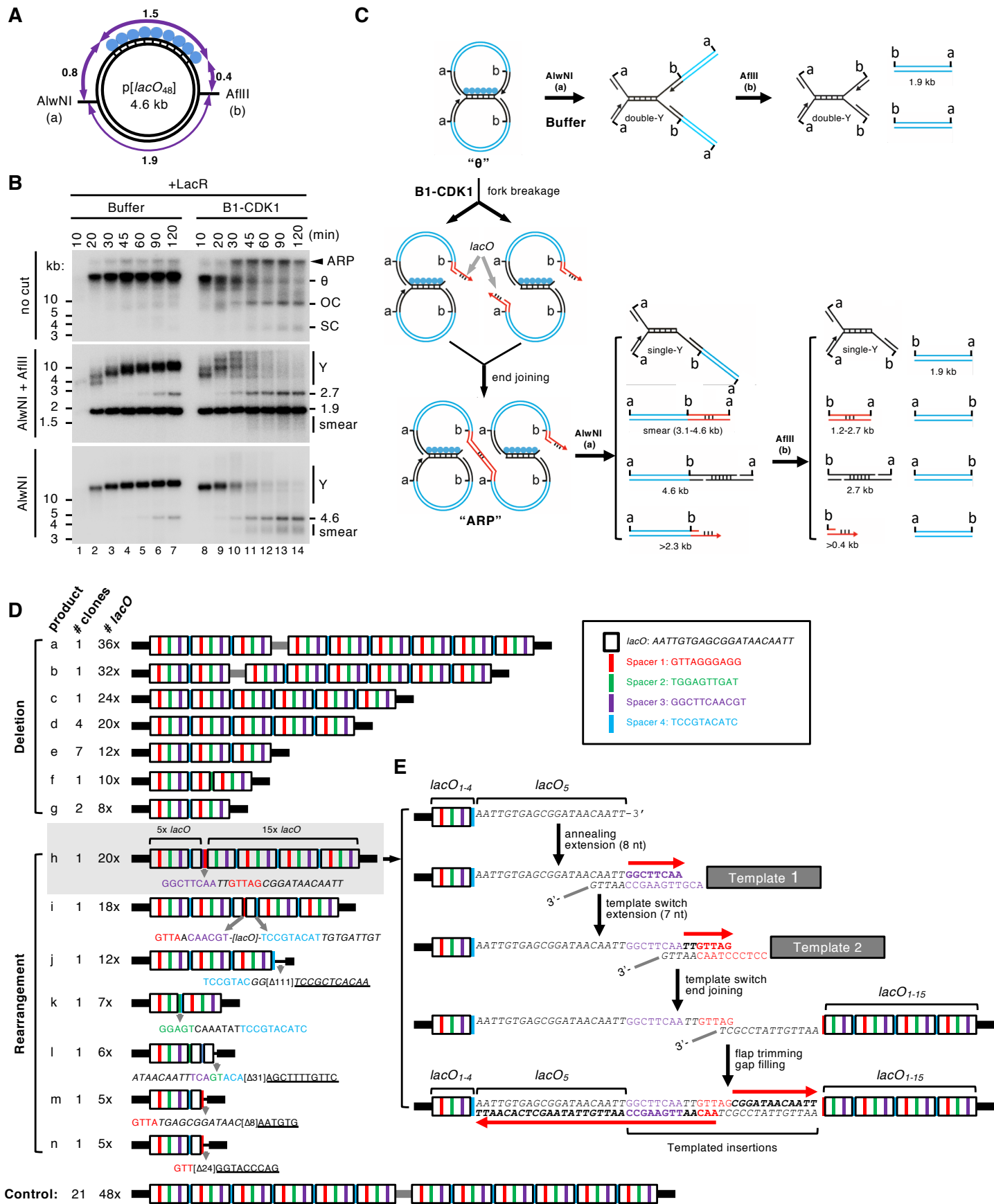


Figure 2

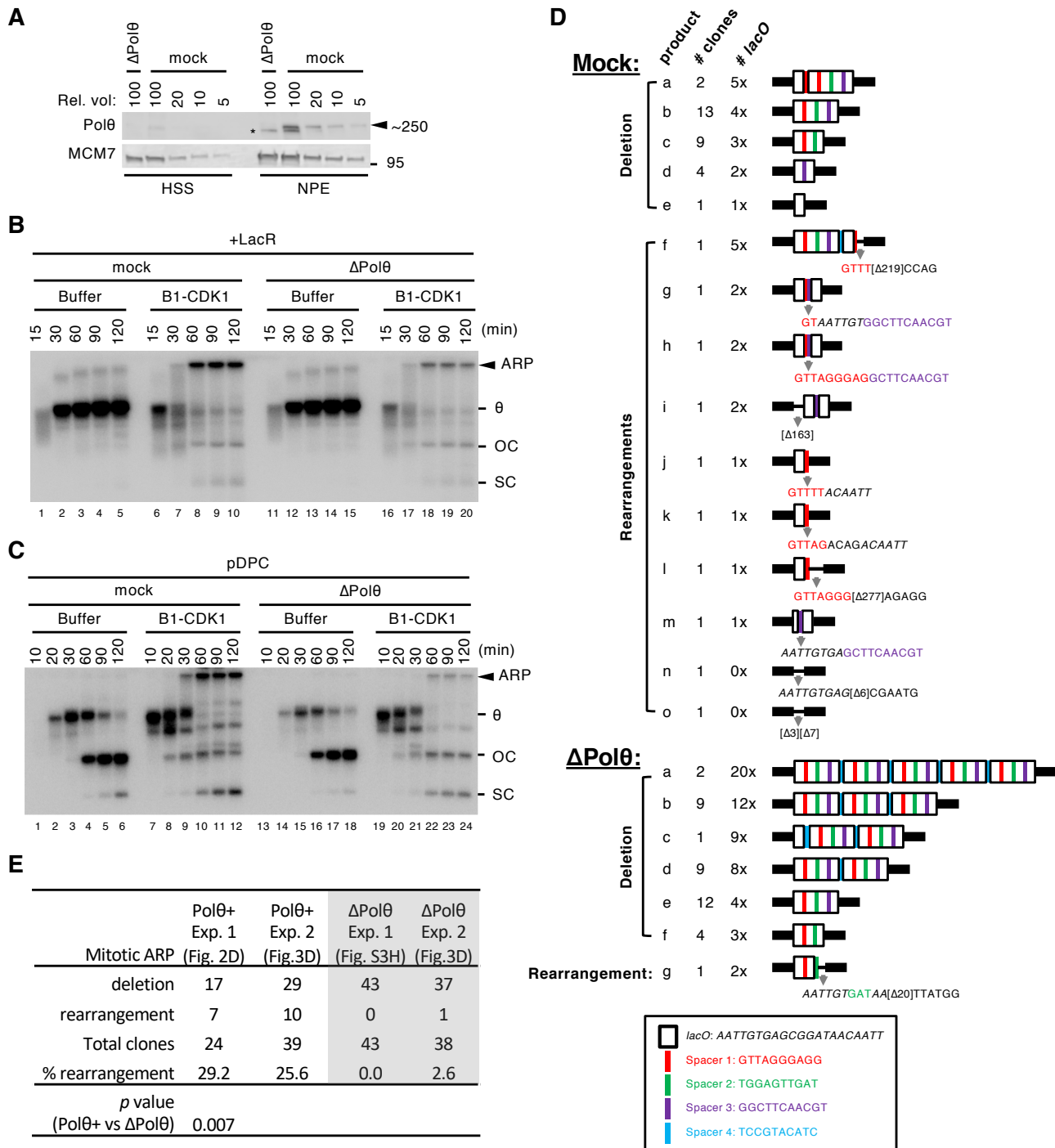


Figure 3

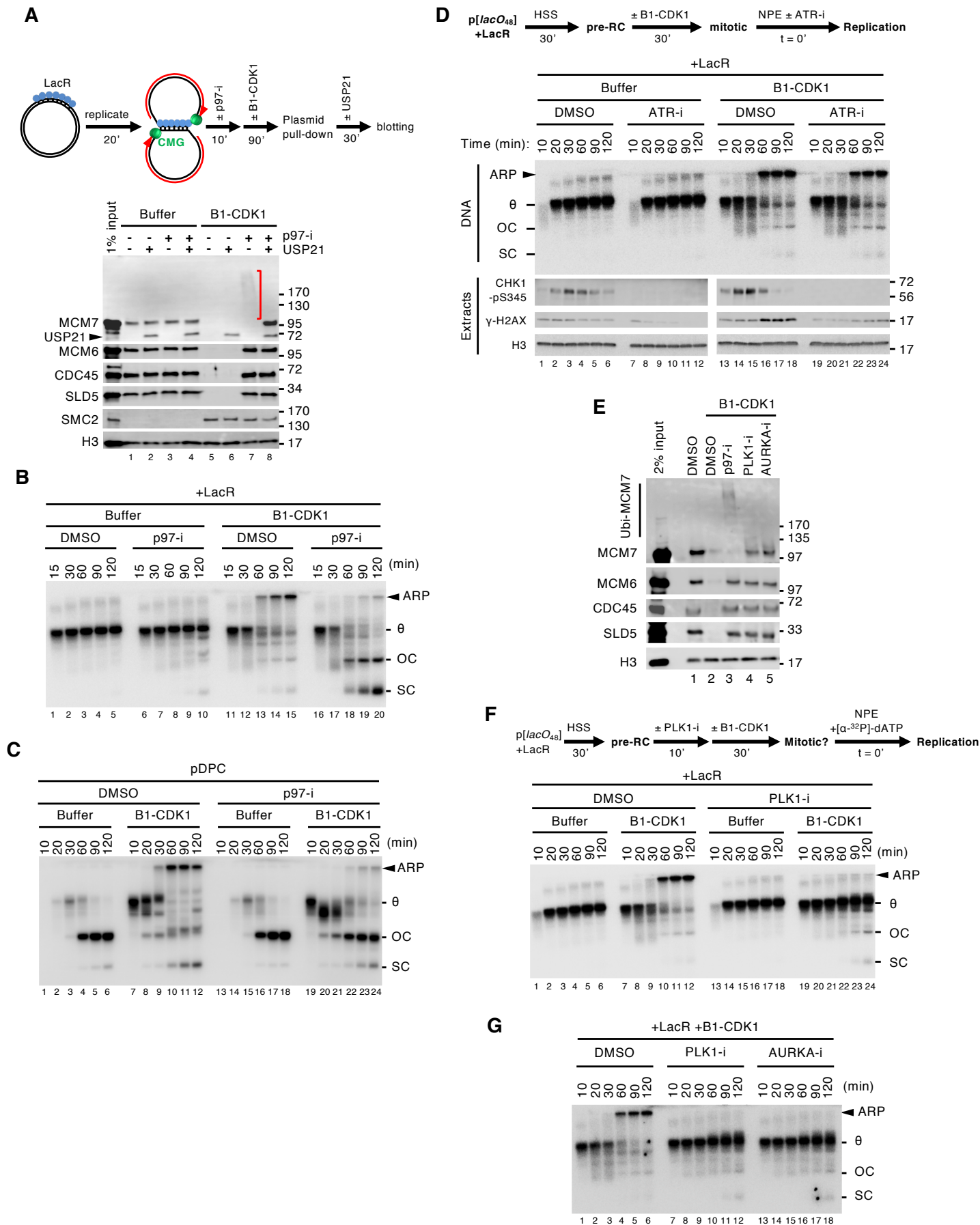


Figure 4

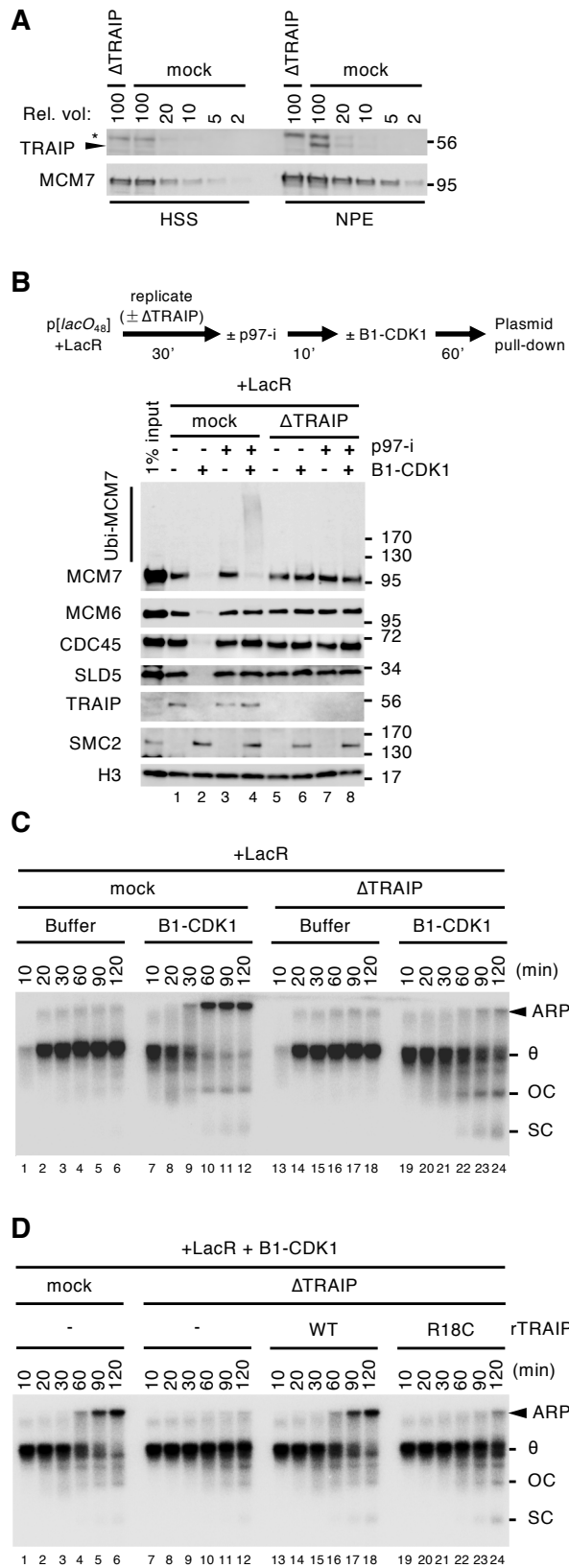


Figure 5

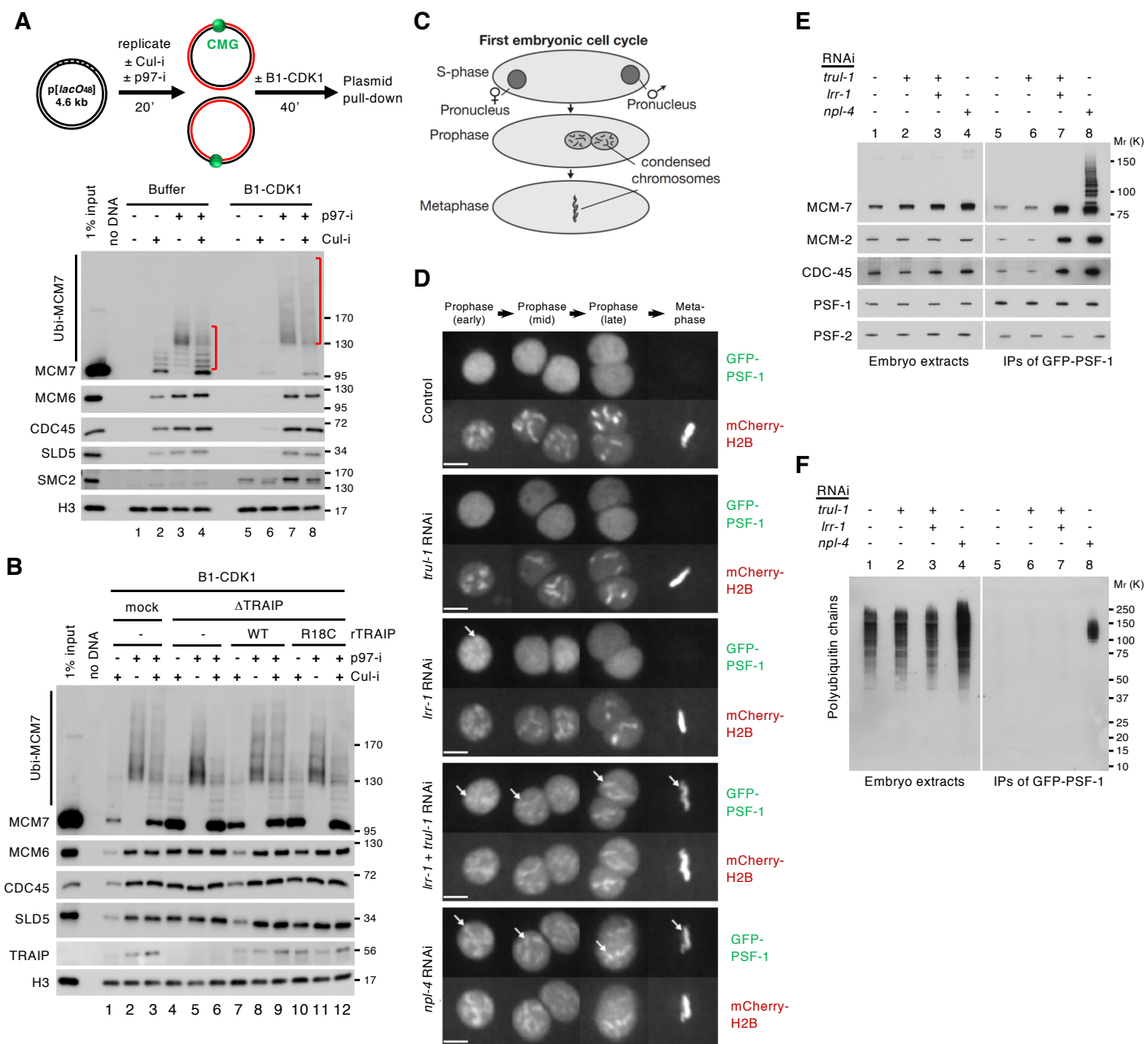


Figure 6

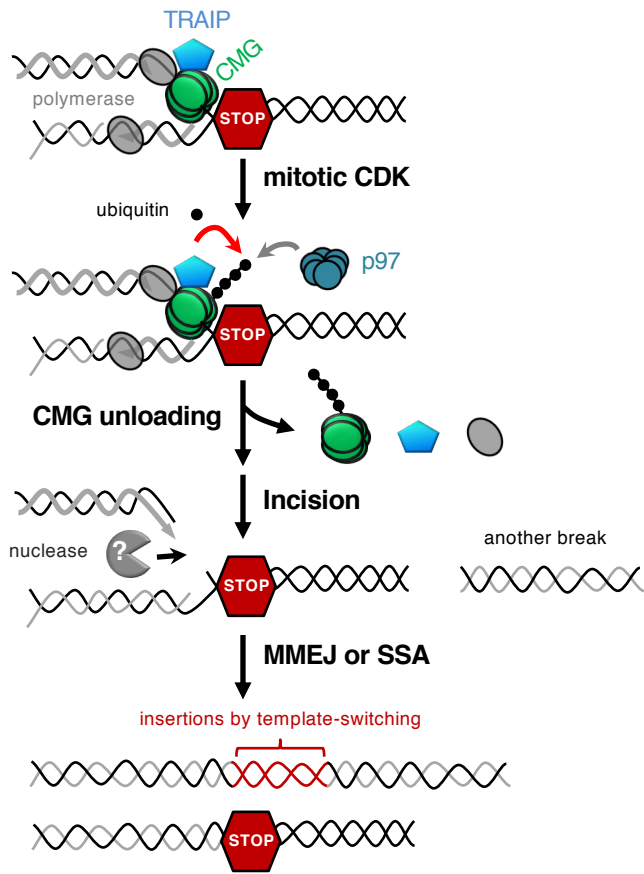


Figure 7

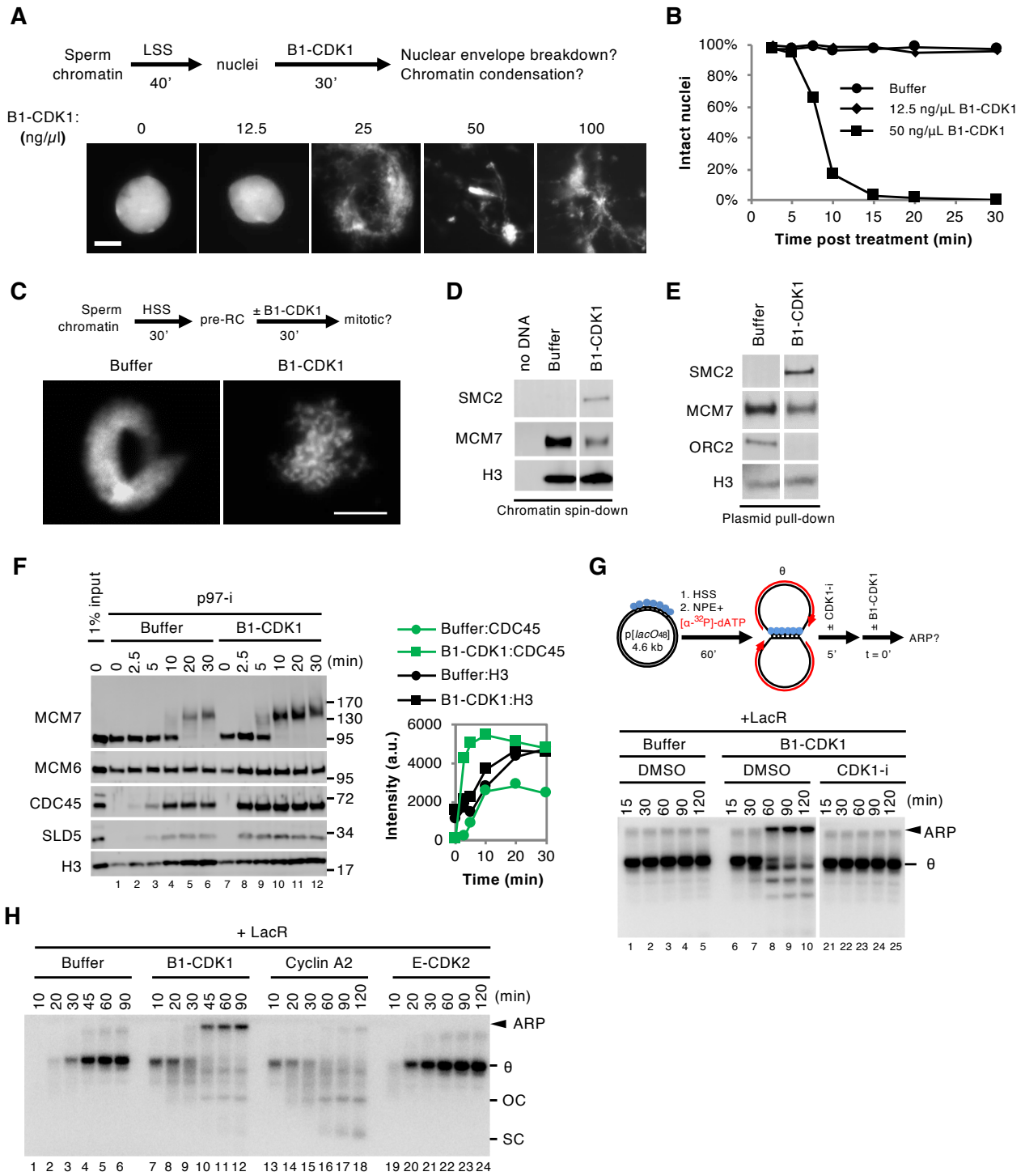


Figure S1

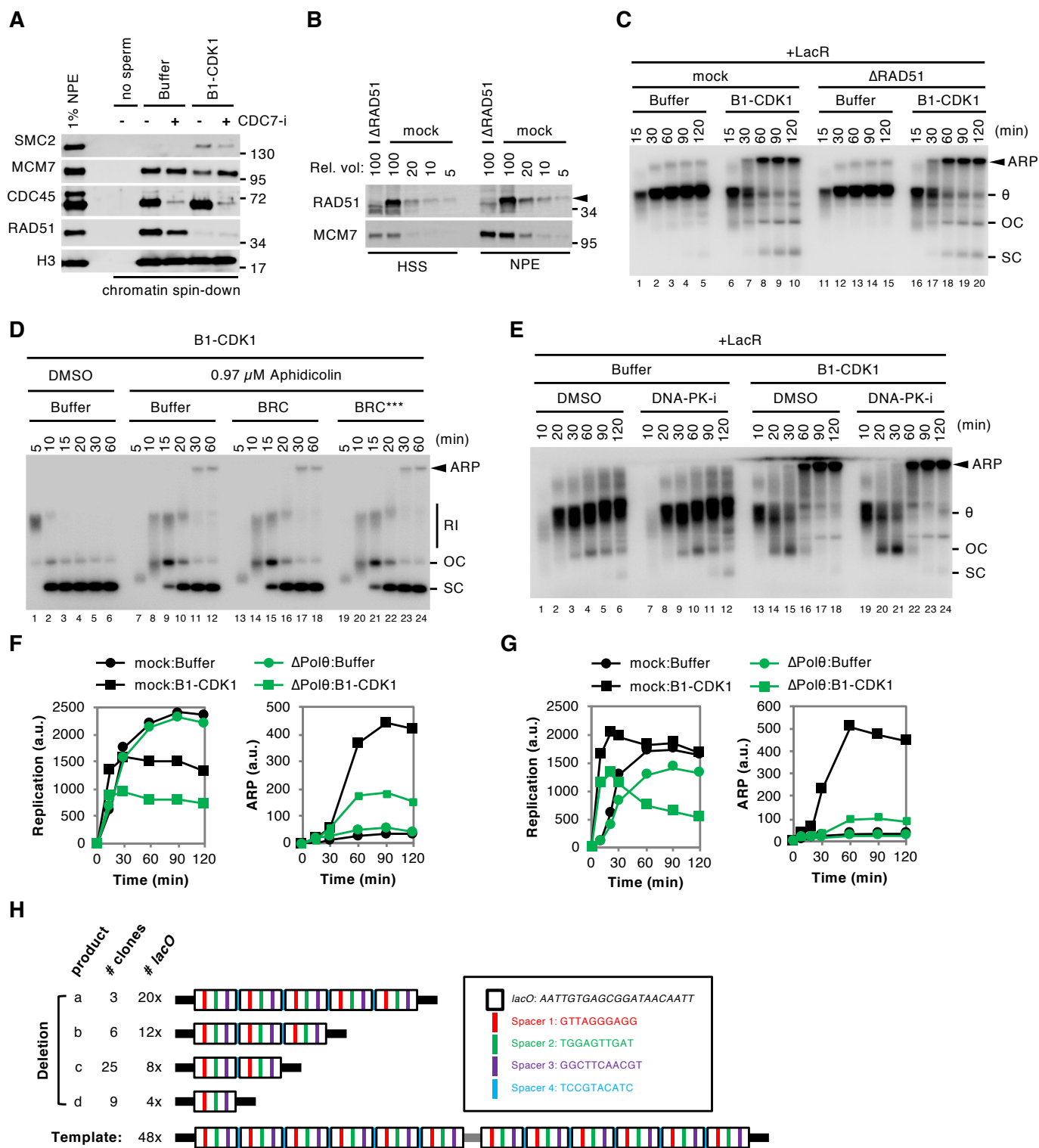


Figure S3

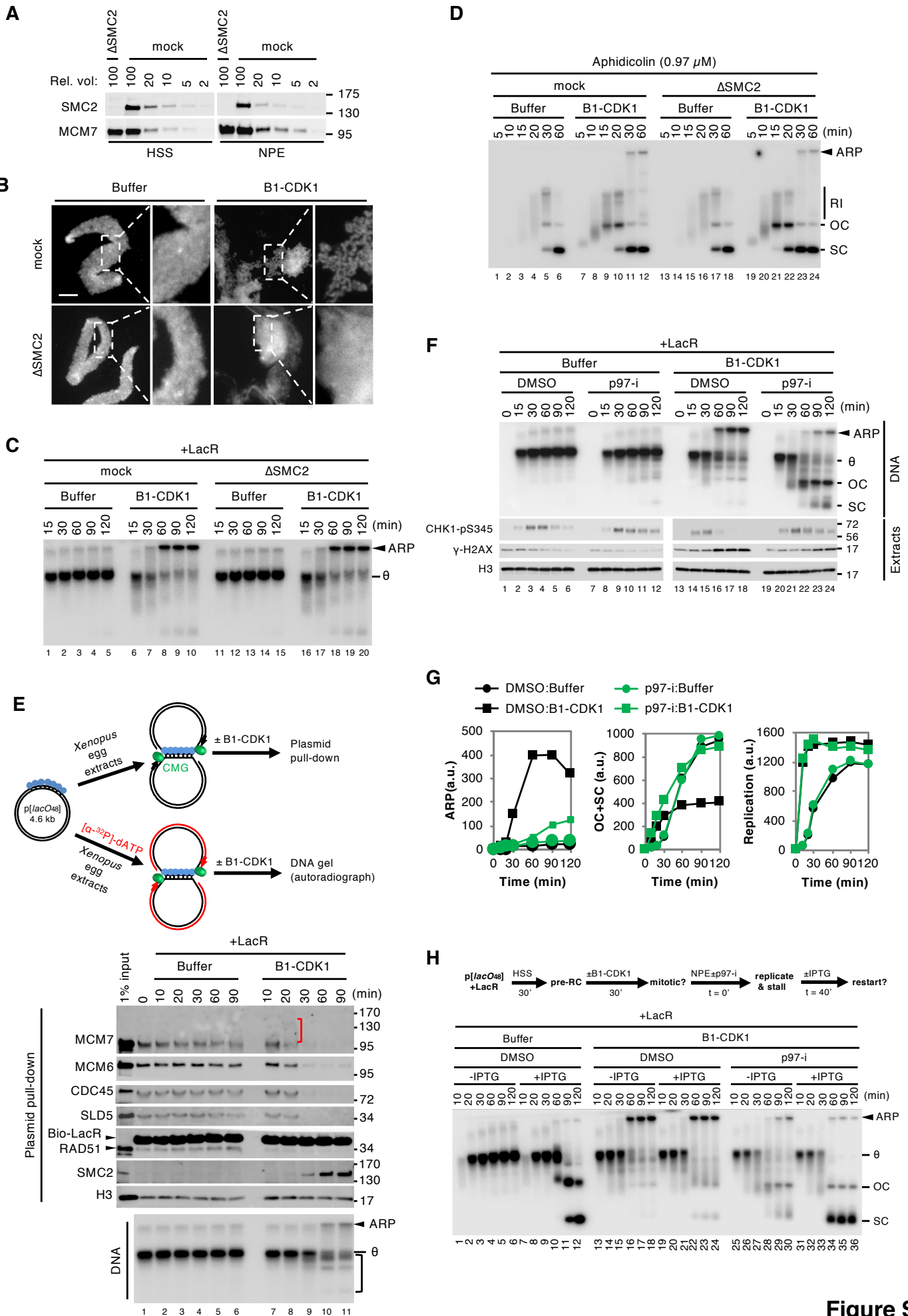


Figure S4

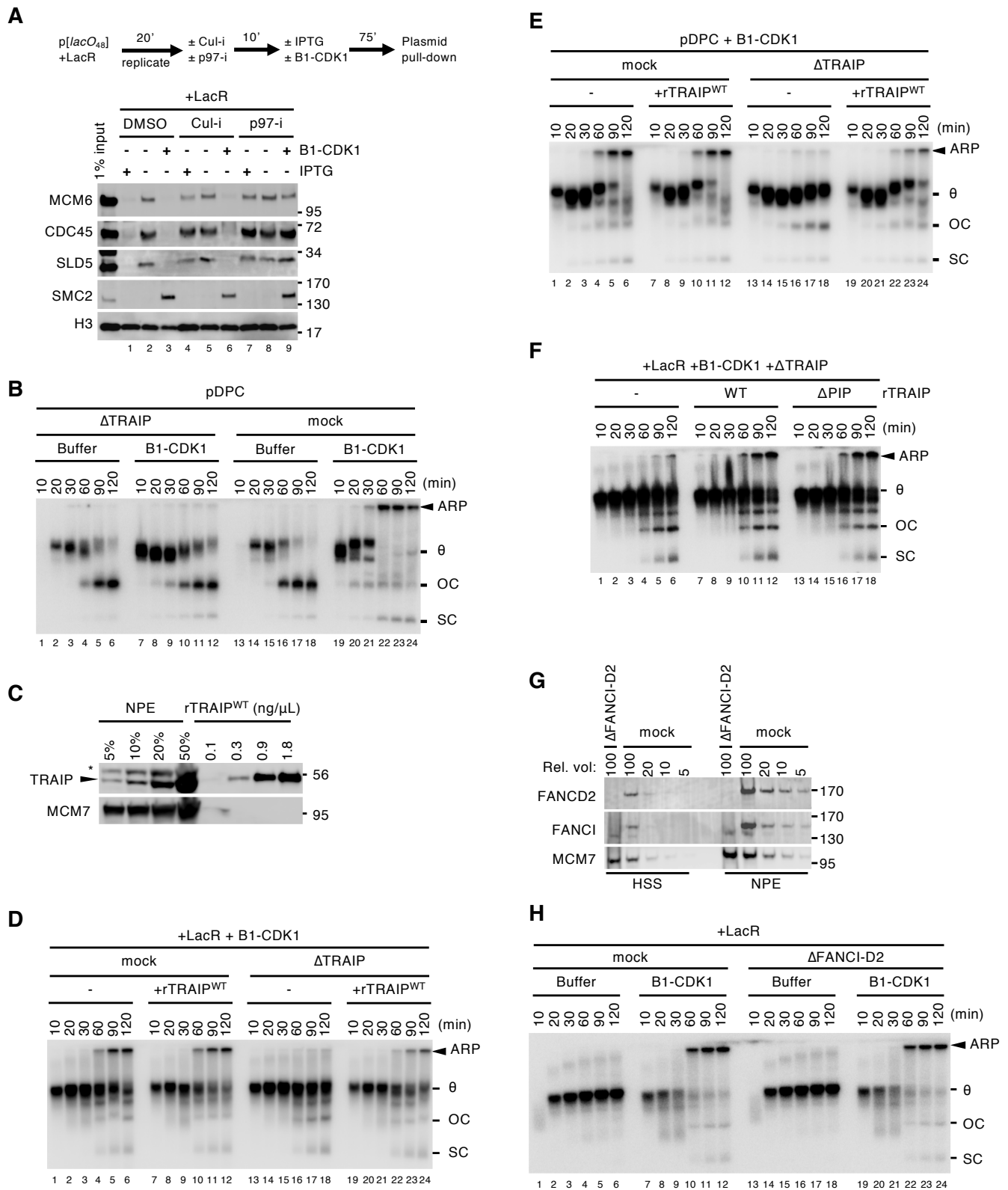


Figure S5

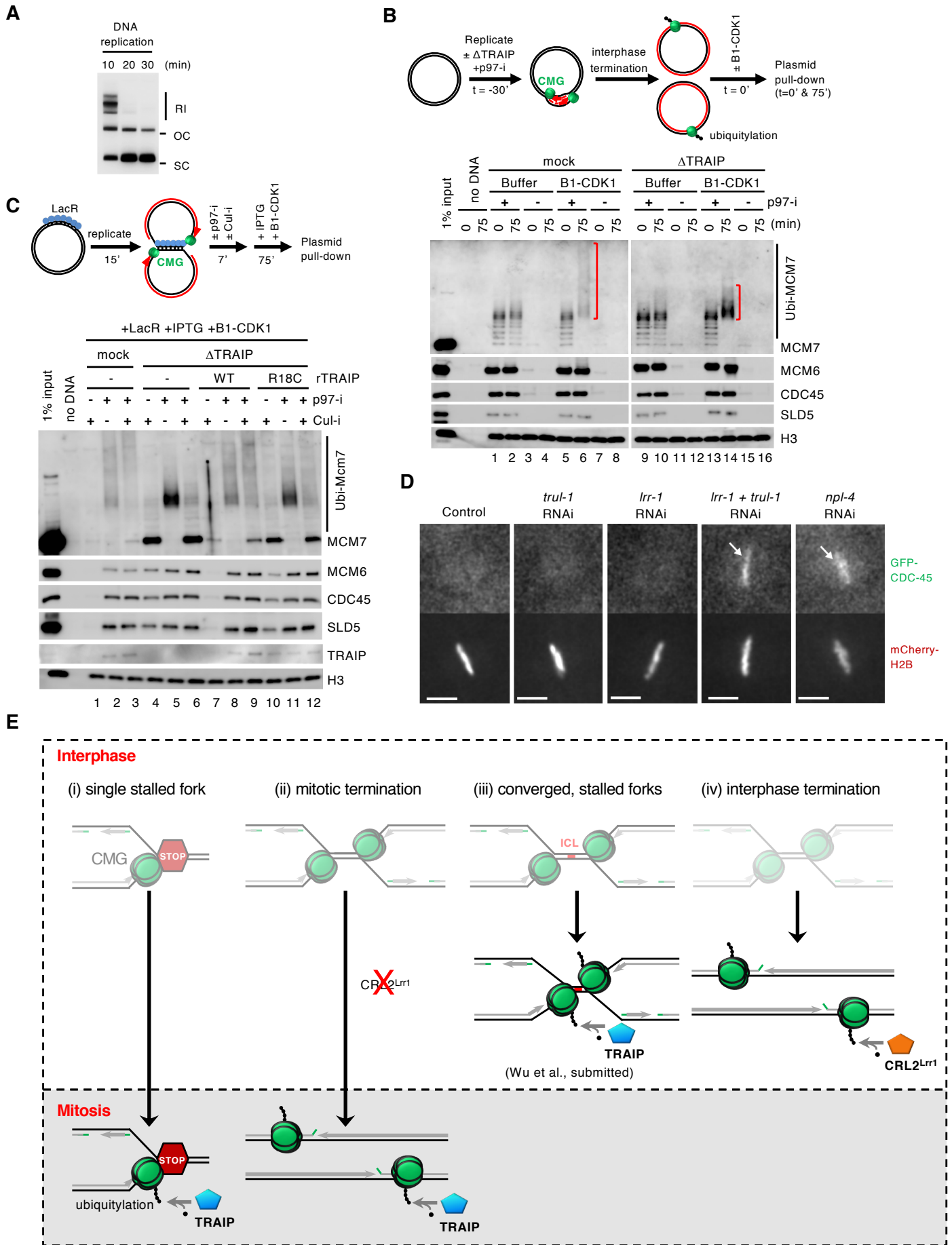


Figure S6

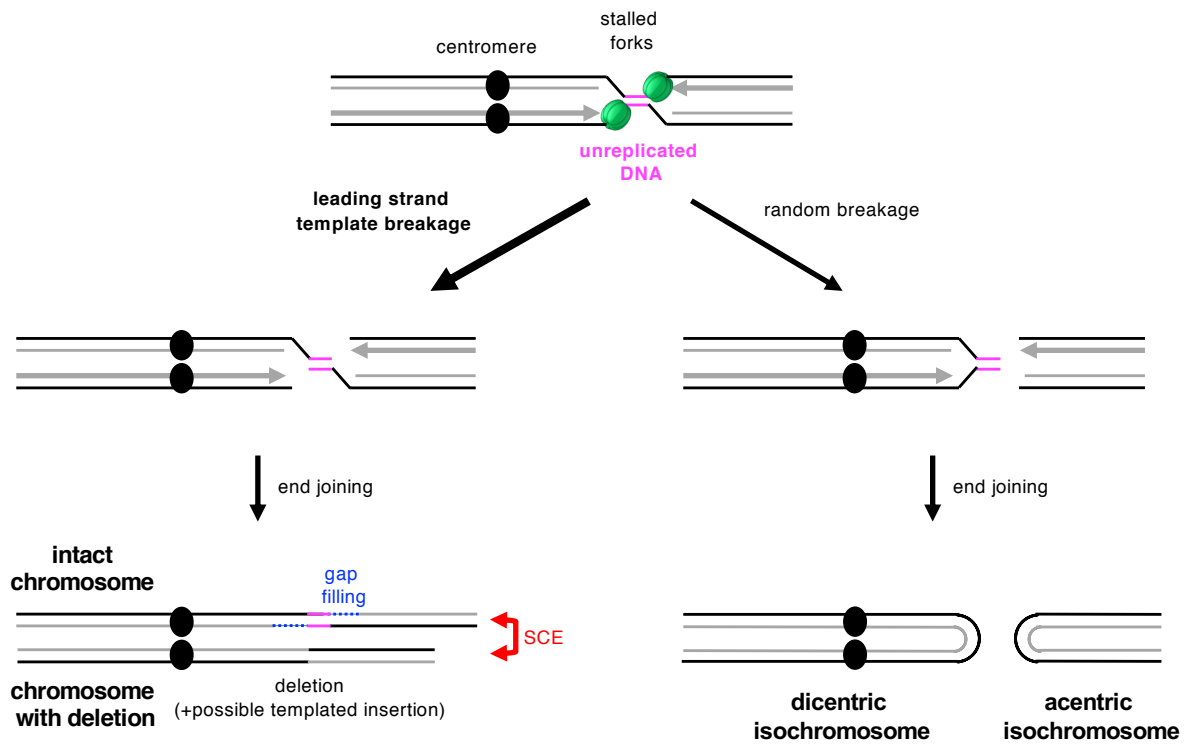


Figure S7

1 **Ubiquitylation of the CMG helicase regulates vertebrate DNA repair**

2

3 R. Alex Wu^{1*}, Daniel R. Semlow^{1*}, Ashley N. Kamimae-Lanning², Olga V. Kochenova¹,
4 Michael R. Hodkinson², Ravindra Amunugama¹, Lin Deng^{1,3,4}, Claudia A. Mimoso¹, Ketan J.
5 Patel^{2,5} & Johannes C. Walter^{1,6†}

6 ¹ Department of Biological Chemistry and Molecular Pharmacology, Harvard Medical School,
7 Boston, MA 02115, USA.

8 ² MRC Laboratory of Molecular Biology, Cambridge Biomedical Campus, Cambridge CB2 0QH, UK.

9 ³ Department of Pediatric Oncology, Dana-Farber Cancer Institute, Boston, MA 02215, USA.

10 ⁴ Department of Cell Biology, Harvard Medical School, Boston, MA 02115, USA.

11 ⁵ Department of Medicine, University of Cambridge, Addenbrooke's Hospital, Cambridge CB2 0QQ, UK.

12 ⁶ Howard Hughes Medical Institute, Boston, MA 02115, USA.

13

14 † e-mail: Johannes_Walter@hms.harvard.edu

15 * These authors contributed equally to this work

16 **Summary:** Cells often use multiple pathways to repair the same DNA lesion, and elucidating how
17 one pathway is prioritized over another is crucial to understand how cells maintain genome
18 stability. DNA interstrand cross-links (ICLs) block DNA replication and transcription by
19 covalently linking the Watson and Crick strands of DNA, and the cytotoxicity of ICLs underlies
20 numerous chemotherapeutics. Replication fork collision with ICLs initiates two distinct repair
21 pathways. The NEIL3 glycosylase can cleave the cross-link¹, but if this fails, the Fanconi anemia
22 (FA) proteins incise the phosphodiester backbone surrounding the ICL, generating a DSB
23 intermediate that is repaired by homologous recombination². How cells prioritize the simple
24 NEIL3 pathway over the FA pathway, which can cause genomic rearrangements, is unknown.
25 Here we show that the E3 ubiquitin ligase TRAIP is a master regulator of both ICL repair
26 pathways. Fork convergence at ICLs triggers TRAIP-dependent formation of ubiquitin chains on
27 the replicative DNA helicase CMG (CDC45-MCM2-7-GINS). Short chains can recruit NEIL3
28 through direct ubiquitin binding, whereas longer chains are required for CMG unloading by the
29 p97 ATPase, enabling the FA pathway. Our results identify replicative helicase ubiquitylation as
30 a new signal that dictates DNA repair pathway choice and implicate TRAIP as an attractive target
31 of cancer chemotherapy.

32
33 ICLs are formed by chemotherapeutics and endogenous reactive aldehydes^{3,4}. The classic ICL
34 repair pathway involves twenty-two “FANC” proteins, defects in which cause the human bone
35 marrow failure and cancer predisposition syndrome, FA⁵. Using *Xenopus* egg extracts, we
36 previously showed that the FA pathway is initiated by the convergence of two replication forks on
37 an ICL, which triggers CMG helicase unloading by the p97 ATPase^{1,2,6,7}. CMG unloading involves
38 polyubiquitylation of CMG’s MCM7 subunit⁷, allowing fork reversal and ICL unhooking via

39 nucleolytic incisions that convert the ICL to a DNA double stranded break^{2,8,9} (Fig. 1a, left branch).
40 A second unhooking mechanism acts on a subset of ICLs¹ (Fig. 1a, right branch). In this pathway,
41 the NEIL3 DNA glycosylase cleaves one of the two *N*-glycosyl bonds comprising the ICL, which
42 avoids DSB formation. While both pathways are triggered by fork convergence, only the FA
43 pathway requires CMG unloading¹. In mammals, FANC gene mutations cause stronger
44 phenotypes than mutations in NEIL3¹⁰⁻¹³. Therefore, while cells may first attempt the simpler
45 NEIL3 pathway, they appear to rely more heavily on the versatile FA pathway for survival. Given
46 the different mutagenic potentials of the FA and NEIL3 pathways, it is crucial to understand how
47 cells govern the choice between these two mechanisms.

48 Another critical gap in our knowledge is the identity of the E3 ubiquitin ligase that
49 ubiquitylates CMG at ICLs to activate CMG unloading and entry into the FA pathway. The RING
50 E3 ligase TRAIIP (TRAF-interacting protein) is essential for cell proliferation¹⁴, and hypomorphic
51 TRAIIP mutations cause microcephalic primordial dwarfism¹⁵. Because TRAIIP knock-down
52 sensitizes cells to mitomycin C (MMC)¹⁶ and TRAIIP associates with ICL-containing chromatin¹⁷,
53 we asked whether TRAIIP promotes CMG unloading at ICLs. To this end, *Xenopus* egg extracts
54 (Extended Data Fig. 1a) were used to replicate a plasmid containing a site-specific cisplatin-ICL.
55 In mock-depleted extract, forks converged on the ICL and stalled, generating a discrete “slow
56 Figure 8” intermediate that was converted to a “fast Figure 8” species due to CMG unloading⁸ (Fig.
57 1b, lanes 1-3, Extended Data Fig. 1b). Strikingly, depletion of TRAIIP (Extended Data Fig. 2a)
58 caused an accumulation of the slow Figure 8 intermediate (Fig. 1b, lanes 11-15), the same defect
59 observed when CMG unloading was blocked with a p97 inhibitor¹ (p97i; Fig. 1b, lanes 6-10).
60 Wild-type recombinant *Xenopus* TRAIIP (rTRAIIP^{WT}) (Extended Data Fig. 2b) restored fast Figure
61 8 formation (Fig. 1b, Extended Data Fig. 2c). In contrast, rTRAIIP^{R18C} (Extended Data Fig. 2b),

62 which harbors a primordial dwarfism-associated RING-domain mutation¹⁵ that compromises E3
63 ubiquitin ligase activity (Extended Data Fig. 2d), did not (Fig. 1b). Consistent with TRAI-
64 P-dependent CMG unloading, efficient loss of the CMG footprint at ICLs required the E3 ligase
65 activity of TRAI (Extended Data Fig. 2e, f). As shown in Fig. 1c, active TRAI was required for
66 dissociation of CDC45 and MCM7, two CMG subunits, from pICL^{Pt}. In addition, formation of
67 ubiquitylated MCM7 was dependent on TRAI (Fig. 1c). This effect was even more evident when
68 CMG unloading was blocked with p97i (Fig. 1d). rTRAI^{R18C} partially rescued MCM7
69 ubiquitylation (Fig. 1d, compare lanes 13-14 with 7-8), consistent with residual E3 ligase activity
70 in this mutant (Extended Data Fig. 2d). Our previous conclusion that BRCA1 is required for CMG
71 unloading¹⁸ was due to inadvertent depletion of TRAI with BRCA1 antiserum (Extended Data
72 Fig. 3). Importantly, active TRAI is required for replication fork reversal at an ICL (Fig. 1e), a
73 likely prerequisite for incisions⁸ (Fig. 1a), and for error-free repair of the lesion (Fig. 1f).
74 Collectively, these results demonstrate that TRAI is required for MCM7 ubiquitylation and CMG
75 unloading in the FA ICL repair pathway.

76 Consistent with CMG unloading at ICLs requiring fork convergence⁶, MCM7
77 ubiquitylation also depended on replication fork convergence (Fig. 2a). Thus, either TRAI is
78 recruited *de novo* when CMGs converge on an ICL, or it travels with the replisome but only
79 ubiquitylates CMG upon fork convergence. In agreement with the latter scenario, TRAI
80 associated with undamaged pCTRL at levels similar to those seen on pICL (Fig. 2b, compare lanes
81 2 and 5), and in mammalian cells, TRAI localizes to DNA replication forks in the absence of
82 exogenous insults^{15,16}. TRAI lacking its conserved, C-terminal PIP box (TRAI^{ΔPIP}) still
83 suppresses MMC hypersensitivity¹⁶. Similarly, recombinant *Xenopus* TRAI^{ΔPIP} suppressed the
84 accumulation of slow Figure 8 structures (Fig. 2c, Extended Data Fig. 3g). TRAI therefore travels

85 with the replisome but ubiquitylates CMG only after fork convergence at an ICL, independently
86 of its PIP box.

87 TRAIP does not participate in CMG unloading during replication termination (Extended
88 Data Fig. 4a, b), which depends on formation of K48-linked ubiquitin chains by CRL2^{LRR1} (Fig.
89 2d)^{19,20}. Conversely, MCM7 ubiquitylation and CMG unloading at ICLs does not require
90 CRL2^{LRR1} (Extended Data Fig. 4a, c-e), and the chains formed by TRAIP in this context involve
91 primarily K63-linkages, as determined by digestion with chain-specific deubiquitylating
92 enzymes²¹ (Fig. 2d). Thus, CMG unloading during ICL repair is mechanistically distinct from
93 CMG unloading during replication termination and likely involves formation of K63-linked
94 ubiquitin chains on CMG.

95 Unlike cisplatin-ICLs, psoralen-ICLs and AP-ICLs (formed between an abasic site in one
96 strand and an adenosine in the other strand) are unhooked by NEIL3 independently of CMG
97 unloading¹. However, as shown in Extended Data Fig. 5a, MCM7 was ubiquitylated with similar
98 kinetics when forks converged on an AP-ICL versus a cisplatin-ICL. We therefore asked whether
99 AP-ICL repair requires TRAIP. In mock-depleted extract, Figure 8 intermediates generated when
100 forks converge on an AP-ICL were converted directly into open circular and supercoiled products,
101 reflecting NEIL3-dependent unhooking¹ (Fig. 3a; see Extended Data Fig. 5b for a schematic of
102 pICL^{AP} repair intermediates). Strikingly, unlike p97 inhibition (Extended Data Fig. 5c, lanes 27-
103 30), immunodepletion of TRAIP caused a marked accumulation of slow Figure 8s and a strong
104 reduction in open circular and supercoiled plasmids (Fig. 3a). Furthermore, TRAIP depletion
105 greatly reduced AP-ICL repair (Fig. 3b). Addition of rTRAIP^{WT} fully reversed these defects (Fig.
106 3a, b, Extended Data Fig. 5d). Surprisingly, rTRAIP^{R18C} also mostly reversed these defects,
107 suggesting that low levels of ubiquitylation support AP-ICL repair (Fig. 3a, b, Extended Data Fig.

108 5d). Thus, TRAIP performs a critical function during AP-ICL repair that is independent of CMG
109 unloading.

110 We postulated that TRAIP-dependent MCM7 ubiquitylation recruits NEIL3 to converged
111 forks. Because endogenous NEIL3 on chromatin was undetectable by immunoblotting, we
112 supplemented extract with FLAG epitope-tagged recombinant NEIL3 (rNEIL3) and examined its
113 chromatin binding using FLAG antibody. rNEIL3 recovery was abolished by geminin,
114 demonstrating its binding was replication-dependent (Extended Data Fig. 5a). Interestingly, we
115 detected more rNEIL3 on pICL^{Pt} than on pICL^{AP} (Extended Data Fig. 5a), likely because NEIL3
116 becomes trapped on chromatin when it cannot unhook the ICL (Extended Data Fig. 5e, f). Given
117 this increased association of rNEIL3 with pICL^{Pt}, this plasmid was used for subsequent NEIL3
118 recruitment assays. Importantly, depletion of TRAIP strongly reduced the association of rNEIL3
119 with pICL^{Pt} (Fig. 3c, lanes 1-8). Recombinant TRAIP^{WT} fully rescued and rTRAIP^{R18C} partially
120 rescued this defect (Fig. 3c, Extended Data Fig. 5g). Our data indicate that TRAIP-dependent
121 CMG ubiquitylation is required to recruit NEIL3 for ICL unhooking. Consistent with this model,
122 delaying CMG unloading extends the window of time during which NEIL3 can unhook an AP-
123 ICL (Extended Data Fig. 6).

124 NEIL3 contains an N-terminal glycosylase domain and three C-terminal zinc finger
125 motifs²² (Fig. 3d). NEIL3 lacking the entire C-terminal region (rNEIL3^{Δ291}) was active as a
126 glycosylase (Extended Data Fig. 7a) but failed to unhook pICL^{AP} (Fig. 3e) or bind pICL in extract
127 (Fig. 3f), suggesting that one or more of the zinc fingers helps recruit NEIL3 to stalled forks. Using
128 biolayer interferometry, we found that the NPL4-type zinc finger (NZF) of NEIL3 binds
129 monoubiquitin dependent on a conserved TL motif (Extended Data Fig. 7b), as seen for other
130 NZFs²³. Importantly, pICL^{AP} unhooking was reduced more than two-fold by a TL motif

131 substitution (rNEIL3^{TL310-311LV}) and four-fold by substitutions of zinc-coordinating cysteines in
132 the NZF (rNEIL3^{NZF-C to A}; Fig. 3e, Extended Data Fig. 7c). Consistent with this observation,
133 rNEIL3^{NZF-C to A} and rNEIL3^{TL310-311LV} bound poorly to pICL (Fig. 3f). The other two NEIL3 zinc
134 fingers resemble the “GRF” zinc finger of the AP endonuclease APE2, which binds single-
135 stranded (ss)DNA²⁴. We found that GRF1 and GRF2 each bound specifically to ssDNA (Extended
136 Data Fig. 8a, b), and point mutations that disrupt this binding compromised the association of
137 NEIL3 with chromatin and its ability to support AP-ICL unhooking (Extended Data Fig. 8c-e).
138 Our data suggest that NEIL3 is targeted to converged CMGs through cooperation of its NZF, which
139 recognizes ubiquitylated MCM7, and its GRFs, which recognize ssDNA, possibly on the lagging
140 strand template (Extended Data Fig. 8f).

141 In egg extracts, AP-ICLs and psoralen ICLs are processed almost exclusively by NEIL3,
142 but in its absence, these lesions are unhooked by the FA pathway¹. The question arises how the
143 NEIL3 pathway is prioritized over the FA pathway. Interestingly, rTRAI^{R18C}, which only forms
144 short ubiquitin chains on MCM7 (Figs. 1c, 3c), had no detectable activity in cisplatin-ICL repair
145 (Fig. 1b, e) while promoting robust AP-ICL repair (Fig. 3a, b). These results suggest that short
146 ubiquitin chains might be sufficient to support the NEIL3 but not the FA pathway. Consistent with
147 this idea, ubiquitin that lacks lysines and therefore cannot undergo polyubiquitylation (Ub^{NoK})
148 greatly stabilized the pICL^{Pt} slow Figure 8 species (indicative of defective p97-dependent CMG
149 unloading) while having only a modest effect on pICL^{AP} slow Figure 8 disappearance, which
150 reflects NEIL3 unhooking (Fig. 4a; see graphs for quantification). As expected, Ub^{NoK} reduced the
151 length of ubiquitin chains formed on MCM7 (Fig. 4b). Consistent with its modest effect on AP-
152 ICL unhooking, Ub^{NoK} did not affect recruitment of NEIL3 to chromatin (Fig. 4b). The data
153 suggest that short ubiquitin chains on MCM7 are sufficient to recruit NEIL3. If the ICL cannot be

154 cleaved by NEIL3, as in the case of cisplatin-ICLs, the chains continue to grow, leading to
155 activation of p97-dependent CMG unloading (Fig. 4c).

156 Our results establish TRAI^P as a master regulator of ICL repair that prioritizes the NEIL3
157 pathway over the FA pathway. Consistent with redundancy between the FA and NEIL3 pathways
158 in the repair of certain lesions, both must be eliminated in mammalian cells to observe
159 hypersensitivity to psoralen-ICLs while removal of the FA pathway suffices to sensitize cells to
160 cisplatin (Fig. 4d, Extended Data Fig. 9). In interphase, TRAI^P ubiquitylates CMG only upon fork
161 convergence, which avoids inadvertent CMG unloading from forks that have not completed
162 synthesis. Given the extreme ICL sensitivity of cells lacking TRAI^P¹⁶, our data strongly imply that
163 a significant number of ICL repair events in cells require CMG convergence, even though a single
164 fork may be able to trigger repair²⁵. The regulation of TRAI^P is different in mitosis, where Cdk1-
165 Cyclin B promotes TRAI^P activity in the absence of fork convergence (Deng et al., submitted,
166 Extended Data Fig. 10).

167 Patients expressing TRAI^P^{R18C} present with primordial dwarfism, which is caused by
168 reduced cell proliferation¹⁵. We show that TRAI^P^{R18C} promotes residual ubiquitylation and robust
169 unhooking by NEIL3. We propose that in vivo, TRAI^P^{R18C} suppresses the symptoms of Fanconi
170 anemia by supporting the FA pathway, albeit with slower kinetics. Thus, endogenous ICLs may
171 lead to a temporary G2 arrest, leading to reduced cell proliferation and dwarfism. Consistent with
172 this model, cells from both FA and TRAI^P patients exhibit slow progression through G2 in the
173 absence of exogenous crosslinking agents^{15,26}, and FA patients often exhibit short stature⁵.

174

175 **References:**

176 1 Semlow, D. R., Zhang, J., Budzowska, M., Drohat, A. C. & Walter, J. C. Replication-
177 Dependent Unhooking of DNA Interstrand Cross-Links by the NEIL3 Glycosylase. *Cell*
178 **167**, 498-511, doi:10.1016/j.cell.2016.09.008 (2016).

179 2 Raschle, M. *et al.* Mechanism of replication-coupled DNA interstrand crosslink repair.
180 *Cell* **134**, 969-980 (2008).

181 3 Deans, A. J. & West, S. C. DNA interstrand crosslink repair and cancer. *Nat Rev Cancer*
182 **11**, 467-480, doi:10.1038/nrc3088 (2011).

183 4 Price, N. E., Catalano, M. J., Liu, S., Wang, Y. & Gates, K. S. Chemical and structural
184 characterization of interstrand cross-links formed between abasic sites and adenine
185 residues in duplex DNA. *Nucleic Acids Res* **43**, 3434-3441, doi:10.1093/nar/gkv174
186 (2015).

187 5 Kottemann, M. C. & Smogorzewska, A. Fanconi anaemia and the repair of Watson and
188 Crick DNA crosslinks. *Nature* **493**, 356-363, doi:10.1038/nature11863 (2013).

189 6 Zhang, J. *et al.* DNA interstrand cross-link repair requires replication-fork convergence.
190 *Nat Struct Mol Biol* **22**, 242-247, doi:10.1038/nsmb.2956 (2015).

191 7 Fullbright, G., Rycenga, H. B., Gruber, J. D. & Long, D. T. p97 Promotes a Conserved
192 Mechanism of Helicase Unloading during DNA Cross-Link Repair. *Mol Cell Biol* **36**,
193 2983-2994, doi:10.1128/MCB.00434-16 (2016).

194 8 Amunugama, R. *et al.* Replication Fork Reversal During DNA Interstrand Crosslink
195 Repair Requires CMG Unloading. *Cell Rep* **23**, 3419-3428 (2018).

196 9 Knipscheer, P. *et al.* The Fanconi anemia pathway promotes replication-dependent DNA
197 interstrand cross-link repair. *Science* **326**, 1698-1701 (2009).

198 10 Massaad, M. J. *et al.* Deficiency of base excision repair enzyme NEIL3 drives increased
199 predisposition to autoimmunity. *J Clin Invest* **126**, 4219-4236, doi:10.1172/JCI85647
200 (2016).

201 11 Parmar, K., D'Andrea, A. & Niedernhofer, L. J. Mouse models of Fanconi anemia. *Mutat*
202 *Res* **668**, 133-140, doi:10.1016/j.mrfmmm.2009.03.015 (2009).

203 12 Sejersted, Y. *et al.* Endonuclease VIII-like 3 (Neil3) DNA glycosylase promotes
204 neurogenesis induced by hypoxia-ischemia. *Proc Natl Acad Sci U S A* **108**, 18802-18807,
205 doi:10.1073/pnas.1106880108 (2011).

206 13 Torisu, K., Tsuchimoto, D., Ohnishi, Y. & Nakabeppu, Y. Hematopoietic tissue-specific
207 expression of mouse Neil3 for endonuclease VIII-like protein. *J Biochem* **138**, 763-772,
208 doi:10.1093/jb/mvi168 (2005).

209 14 Chopard, C., Hohl, D. & Huber, M. The role of the TRAF-interacting protein in
210 proliferation and differentiation. *Exp Dermatol* **21**, 321-326, doi:10.1111/j.1600-
211 0625.2012.01477.x (2012).

212 15 Harley, M. E. *et al.* TRAIIP promotes DNA damage response during genome replication
213 and is mutated in primordial dwarfism. *Nat Genet* **48**, 36-43, doi:10.1038/ng.3451
214 (2016).

215 16 Hoffmann, S. *et al.* TRAIIP is a PCNA-binding ubiquitin ligase that protects genome
216 stability after replication stress. *J Cell Biol* **212**, 63-75, doi:10.1083/jcb.201506071
217 (2016).

218 17 Raschle, M. *et al.* DNA repair. Proteomics reveals dynamic assembly of repair complexes
219 during bypass of DNA cross-links. *Science* **348**, 1253671, doi:10.1126/science.1253671
220 (2015).

- 221 18 Long, D. T., Joukov, V., Budzowska, M. & Walter, J. C. BRCA1 promotes unloading of
222 the CMG helicase from a stalled DNA replication fork. *Mol Cell* **56**, 174-185,
223 doi:10.1016/j.molcel.2014.08.012 (2014).
- 224 19 Moreno, S. P., Bailey, R., Campion, N., Herron, S. & Gambus, A. Polyubiquitylation
225 drives replisome disassembly at the termination of DNA replication. *Science* **346**, 477-
226 481, doi:10.1126/science.1253585 (2014).
- 227 20 Dewar, J. M., Low, E., Mann, M., Raschle, M. & Walter, J. C. CRL2(Lrr1) promotes
228 unloading of the vertebrate replisome from chromatin during replication termination.
229 *Genes Dev* **31**, 275-290, doi:10.1101/gad.291799.116 (2017).
- 230 21 Mevissen, T. E. *et al.* OTU deubiquitinases reveal mechanisms of linkage specificity and
231 enable ubiquitin chain restriction analysis. *Cell* **154**, 169-184 (2013).
- 232 22 Liu, M. *et al.* Expression and purification of active mouse and human NEIL3 proteins.
233 *Protein Expr Purif* **84**, 130-139, doi:10.1016/j.pep.2012.04.022 (2012).
- 234 23 Wang, B. *et al.* Structure and ubiquitin interactions of the conserved zinc finger domain
235 of Npl4. *J Biol Chem* **278**, 20225-20234, doi:10.1074/jbc.M300459200 (2003).
- 236 24 Wallace, B. D. *et al.* APE2 Zf-GRF facilitates 3'-5' resection of DNA damage following
237 oxidative stress. *Proc Natl Acad Sci U S A* **114**, 304-309, doi:10.1073/pnas.1610011114
238 (2017).
- 239 25 Huang, J. *et al.* The DNA Translocase FANCM/MHF Promotes Replication Traverse of
240 DNA Interstrand Crosslinks. *Mol Cell* **52**, 434-446, doi:10.1016/j.molcel.2013.09.021
241 (2013).
- 242 26 Dutrillaux, B., Aurias, A., Dutrillaux, A. M., Buriot, D. & Prieur, M. The cell cycle of
243 lymphocytes in Fanconi anemia. *Hum Genet* **62**, 327-332 (1982).
- 244

245 **Acknowledgements:**

246 We thank David Pellman and members of the Walter lab for comments on the manuscript. We
247 thank Kelly Arnett of the Center for Macromolecular Interactions for help with BLI experiments.
248 Work on ICL repair in the Walter laboratory is supported by NIH grant HL098316 and a gift from
249 the Wiseman family. R.A.W. is supported by postdoctoral fellowship 131415-PF-17-168-01-DMC
250 from the American Cancer Society. D.R.S. is supported by a Jane Coffin Childs postdoctoral
251 fellowship. J.C.W is a Howard Hughes Medical Institute Investigator and an American Cancer
252 Society Research Professor.

253

254 **Author contributions:**

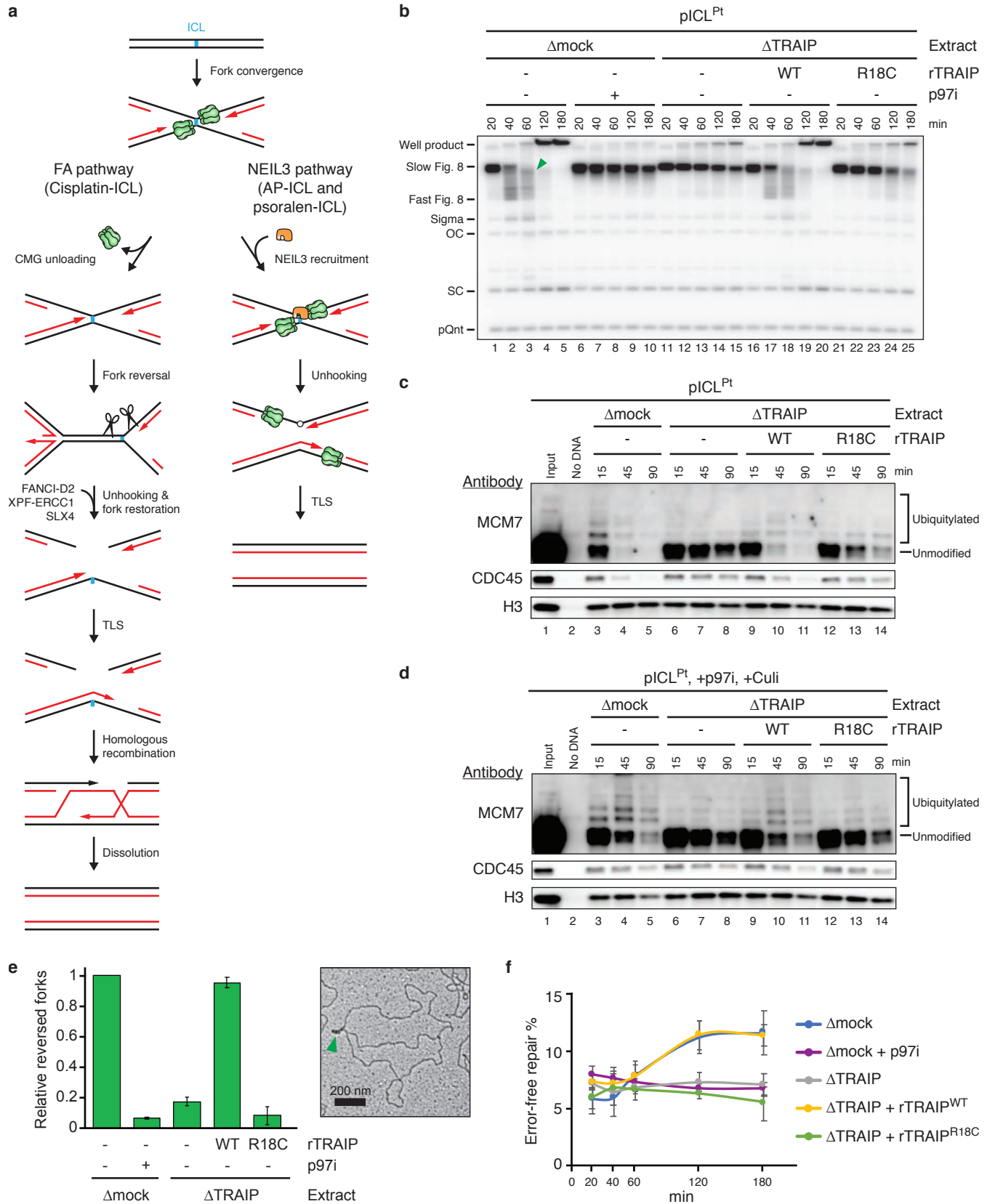
255 R.A.W. identified TRAIP as the E3 ligase that ubiquitylates CMG and characterized the role of
256 TRAIP in cisplatin-ICL repair. D.R.S. characterized the role of CMG ubiquitylation in AP-ICL
257 repair and performed NEIL3 structure-function analysis. A.N.K.-L. and M.R.H. performed the
258 experiments in Fig. 4d and Extended Data Fig. 9 under the supervision of K.J.P. O.V.K. performed
259 the experiments in Fig. 1c, d and Extended Data Fig. 5a and c. R.A. performed EM analysis in
260 Extended Data Fig. 1e. L.D. performed the experiment in Extended Data Fig. 10. C.A.M. assisted
261 with the experiments in Extended Data Figs. 7b, 8a and b. J.C.W., R.A.W., and D.R.S. designed
262 experiments, analyzed the data, and wrote the paper with input from the other authors.

263

264 **Author information:**

265 Reprints and permissions information is available at www.nature.com/reprints. The authors
266 declare no competing financial interests. Correspondence and requests for materials should be
267 addressed to J.C.W. (Johannes_Walter@hms.harvard.edu).

Fig. 1



268 **Fig. 1 | CMG unloading at ICLs requires the E3 ubiquitin ligase TRAIP**

269 **a**, Models of ICL repair by the FA (left branch) and NEIL3 (right branch) pathways. Black lines,
270 parental DNA strands; Red lines, nascent strands; Cyan, ICL; TLS, translesion DNA synthesis.

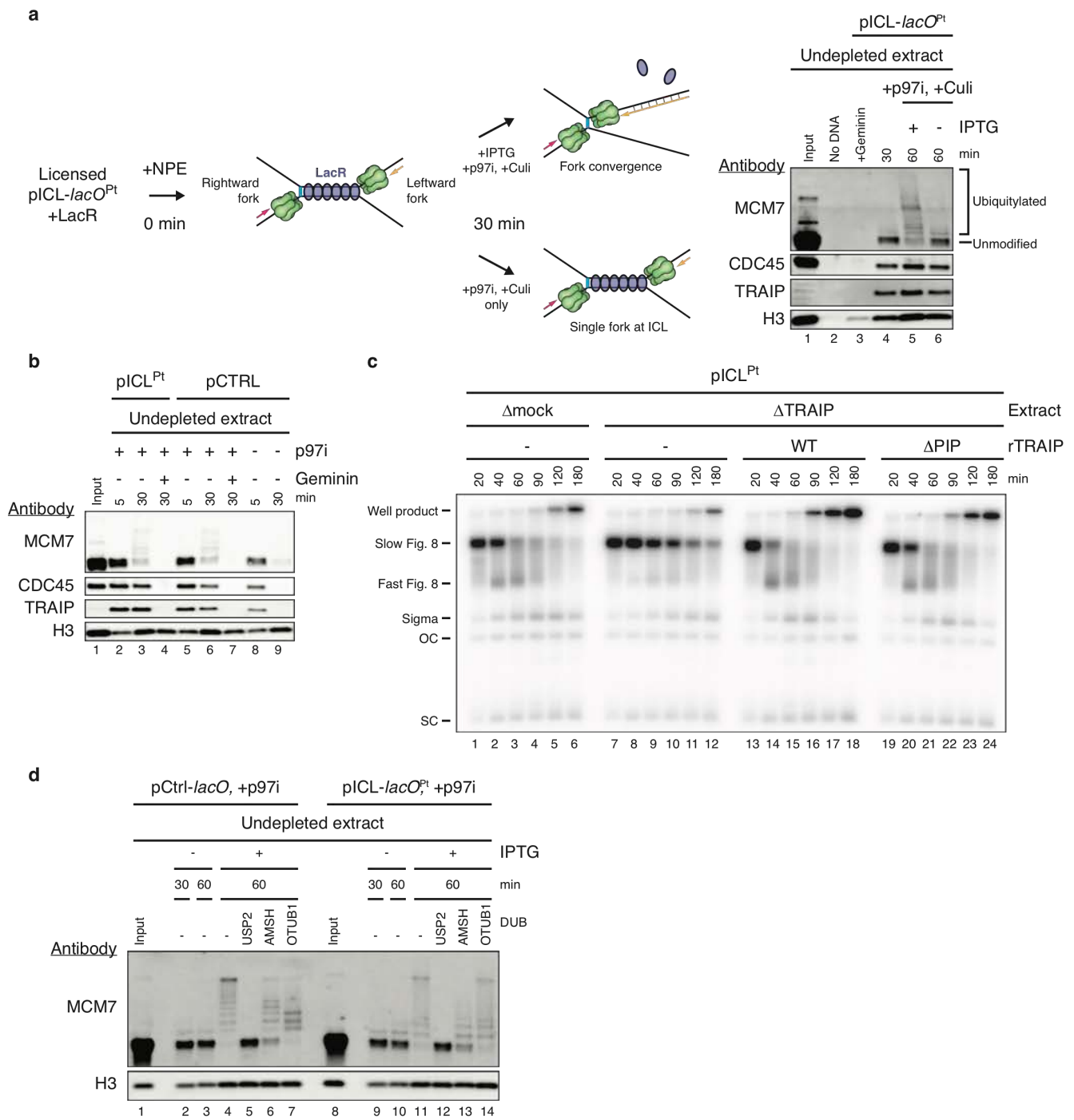
271 **b**, pICL^{Pt} was replicated in egg extracts containing [α -³²P]dATP. Replication intermediates were
272 resolved on a native agarose gel and visualized by autoradiography. Recombinant TRAIP^{WT},
273 rTRAIP^{R18C}, and p97i were added as indicated. OC, open circular; SC, supercoiled; pQnt,
274 undamaged control plasmid; Green arrowhead, reversed fork (see Extended Data Fig. 1b for
275 discussion).

276 **c and d**, Analysis of proteins associated with pICL^{Pt} during replication in the indicated extracts in
277 the absence (**c**) or presence (**d**) of p97i and cullin ubiquitin ligase inhibitor (Culi), which was added
278 to prevent confounding effects of cullin RING E3 ubiquitin ligases.

279 **e**, Left, pICL^{Pt} was replicated for 90 minutes in the indicated extracts, and the relative abundance
280 of reversed forks, as determined by electron microscopy, was quantified and graphed. Values were
281 normalized to the mock-depleted extract. Error bars represent the range from two independent
282 experiments. Right, representative electron micrograph of a reversed fork (green arrowhead) from
283 TRAIP-depleted extract supplemented with rTRAIP^{WT}.

284 **f**, Error-free repair in the indicated extracts as measured by regeneration of a SapI restriction site.
285 The ~7% basal SapI cutting is due to contaminating undamaged plasmid⁹. Error bars, standard
286 error of the mean from three independent experiments.

Fig. 2



287 **Fig. 2 | TRAIP travels with the fork and is activated upon fork convergence**

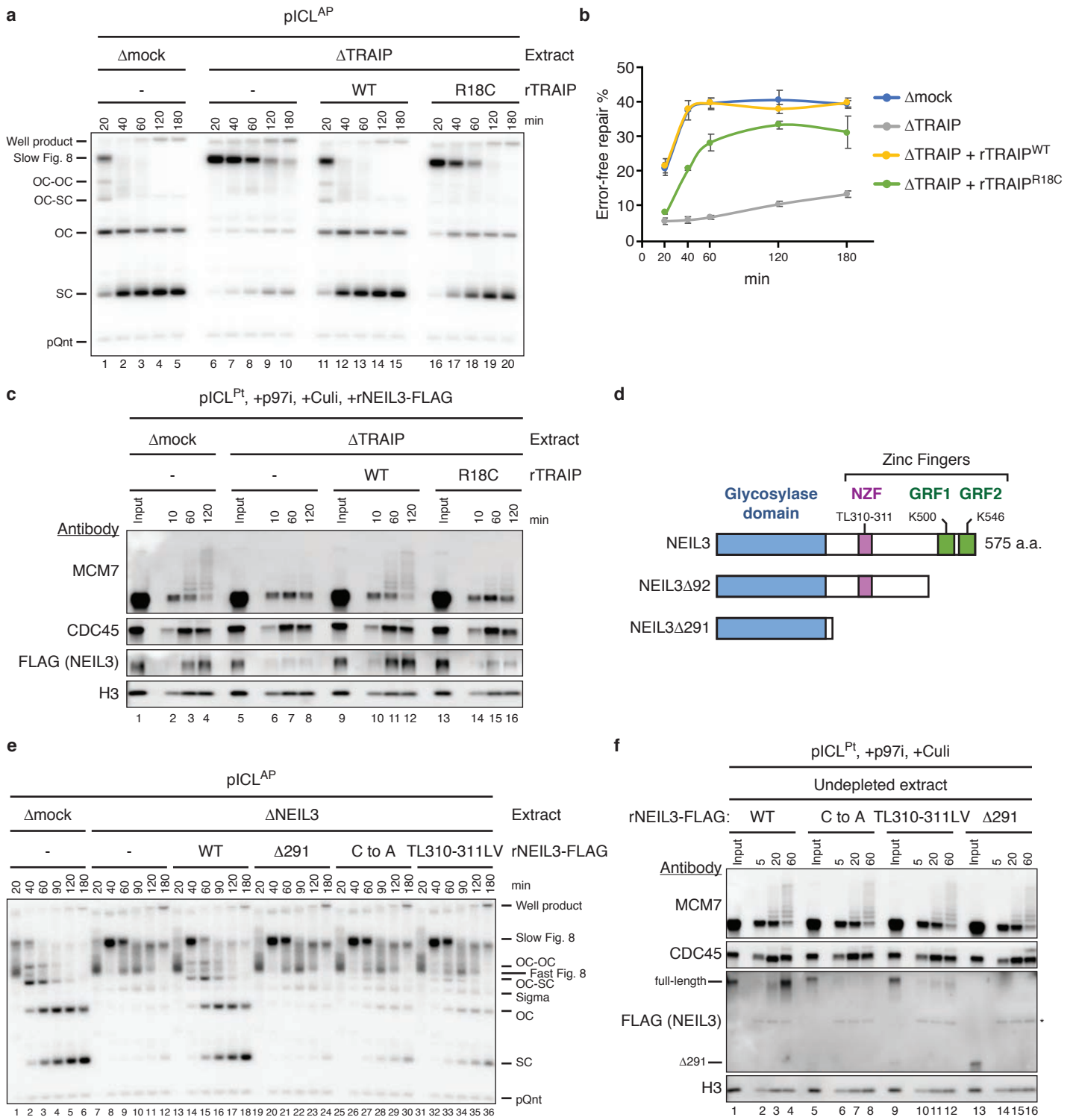
288 **a**, Left, experimental scheme. Plasmid containing an ICL flanked by 48 copies of the *lac* operator
289 (*lacO*) (pICL-*lacO*^{Pt}) was incubated with Lac repressor (LacR) prior to replication in egg extracts.
290 After 30 min, IPTG addition dissociated LacR and allowed fork convergence. Right, at the
291 indicated times, pICL-*lacO*^{Pt} was recovered and blotted for the indicated proteins. Culi suppressed
292 CRL2^{LRR1}-dependent ubiquitylation.

293 **b**, Chromatin-associated proteins during replication of pICL^{Pt} or pCTRL in the presence or absence
294 of the licensing inhibitor geminin and p97i.

295 **c**, pICL^{Pt} was replicated in the indicated extracts and analyzed as in Fig. 1b. TRAIP^{ΔPIP} comprises
296 residues 1-455.

297 **d**, pCtrl-*lacO* and pICL-*lacO*^{Pt} were replicated and recovered as in (a). Samples were then treated
298 with the DUBs USP2 (linkage non-specific), AMSH (K63-linkage specific), or OTUB1 (K48-
299 linkage specific) and blotted for the indicated proteins.

Fig. 3



300 **Fig. 3 | TRAIP promotes NEIL3-dependent ICL repair**

301 **a**, pICL^{AP} was replicated in the indicated extracts and analyzed as in Fig. 1b.

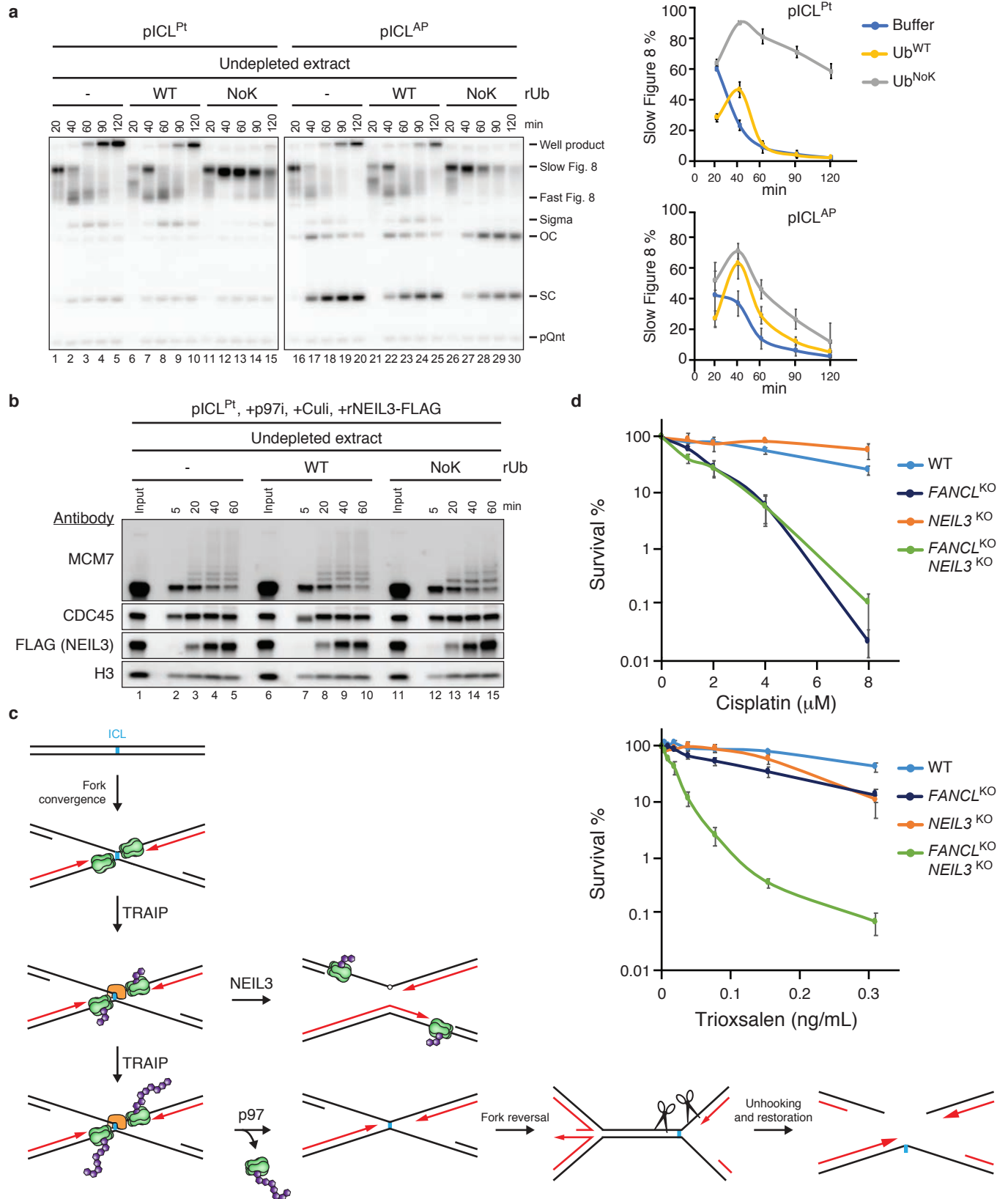
302 **b**, Error-free repair of pICL^{AP} in the indicated extracts, quantified as in Fig. 1e. Error bars, standard
303 error of the mean from three independent experiments.

304 **c and f**, Analysis of proteins associated with pICL^{Pt} during replication in the indicated extracts in
305 the presence of p97i and Culi. A non-specifically detected protein is marked with an asterisk.

306 **d**, Schematic of WT and mutant *Xenopus* NEIL3 proteins.

307 **e**, pICL^{AP} was replicated in the indicated extracts and analyzed as in Fig. 1b.

Fig. 4



308 **Fig 4 | MCM7 ubiquitin chain length influences ICL repair pathway choice**

309 **a**, Left, replication of pICL^{Pt} or pICL^{AP} in the presence of buffer, Ub^{WT}, or Ub^{NoK} was analyzed as
310 in Fig. 1b. Right, quantification of slow Figure 8 structures as a percentage of total replication
311 products. Note that Ub^{WT} and Ub^{NoK} delayed replication by ~20 minutes. Error bars, standard error
312 of the mean from three independent experiments.

313 **b**, Proteins associated with pICL^{Pt} during replication in the presence of p97i and Culi and Ub^{WT} or
314 Ub^{NoK}, as indicated.

315 **c**, Model for hierarchical activation of the NEIL3 and FA pathways by TRAIIP. Green,
316 CMG helicase; purple, ubiquitin; orange, NEIL3.

317 **d**, Clonogenic survival of wild-type, *FANCL*, *NEIL3*, or *FANCL/NEIL3* CRISPR knockout HAP1
318 cells after exposure to cisplatin (top) or trioxsalen and UV-A irradiation (bottom). Error bars,
319 standard error of the mean from at least three independent experiments.

320 **Methods:**

321 All experiments were performed at least twice, with a representative result shown.

322 **Preparation of pICL**

323 Preparations of the following plasmids containing site-specific crosslinks were performed as
324 previously described: pICL^{Pt}; ², pICL-*lacO*^{Pt}; ⁶, and pICL^{AP} and pICL-*lacO*^{AP}; ¹. Briefly, purified
325 cisplatin- or AP-crosslinked oligonucleotide duplexes comprising Pt_Top and PT_Bottom or
326 AP_Top and AP_Bottom, respectively, were ligated into a parental plasmid linearized with BbsI,
327 and the resulting supercoiled plasmid was isolated by cesium chloride gradient.

328 ***Xenopus* Egg Extracts and DNA Replication**

329 *Xenopus* egg extracts were prepared essentially as described²⁷. For DNA replication, plasmids
330 were licensed by incubation in high-speed supernatant (HSS) of egg cytoplasm at room
331 temperature for 30 min at a final concentration of 7.5 ng pICL/ μ l extract (for replication
332 intermediate and nascent strand analyses) or 15 ng pICL/ μ l extract (for plasmid pull-down and
333 electron microscopy analyses) and, where indicated, 0.375 ng pQnt/ μ l extract. For reactions using
334 pICL-*lacO* plasmids with a pre-assembled LacR array, the plasmid was incubated for 1 hr at room
335 temperature with purified biotinylated LacR²⁸ at a final concentration of 14 μ M prior to licensing
336 as described above. To inhibit licensing, geminin was added to HSS at a final concentration of 10
337 μ M and incubated for 10 min at room temperature prior to addition of DNA. Replication was
338 initiated by addition of two volumes of nucleoplasmic egg extract (NPE). In all figures except
339 Extended Data Fig. 10, the addition of NPE corresponds to the 0 min time point. For nascent strand
340 radiolabeling, reactions were supplemented with trace amounts of [α -³²P]dATP. Where indicated,
341 reactions were supplemented with 200 μ M NMS-873 p97 inhibitor (Sigma), 200 μ M MLN4924
342 cullin RING ligase inhibitor (Active Biochem), 111 μ M RO-3306 CDK1 inhibitor (EMD

343 Millipore), and/or 100 μ M recombinant His₆-tagged ubiquitin (Boston Biochem). Reactions were
344 supplemented with approximately 30 to 50 nM recombinant NEIL3-FLAG and 50 to 500 nM
345 recombinant TRAIIP, where indicated.

346 **Antibodies and Immunodepletions**

347 Rabbit polyclonal antibodies raised against the following *X. laevis* proteins were previously
348 described: BRCA1²⁹, CDC45³⁰, CUL2, LRR1, and TRAIIP²⁰, MCM6 and NEIL3¹, MCM7³⁰.
349 Rabbit polyclonal FLAG antibody raised against FLAG peptide was prepared by New England
350 Peptide. Rabbit polyclonal antibody raised against human FANCD2 was previously described³¹.
351 Histone H3 antibody 9715 was purchased from Cell Signaling, histidine tag antibody AD1.1.10
352 was purchased from Bio-Rad, human NEIL3 antibody 11621-1-AP was purchased from
353 ProteinTech Europe, ubiquitin antibody sc-8017 was purchased from Santa Cruz Biotechnology,
354 and vinculin V284 antibody 05-386 was purchased from EMD Millipore. Immunodepletions of
355 BRCA1¹⁸ and LRR1²⁰ were performed as previously described. For TRAIIP depletions, 2.5
356 volumes of 1 mg/mL protein A Sepharose-purified antibodies against TRAIIP were gently rotated
357 with 1 volume of protein A Sepharose beads overnight at 4°C. Five volumes of egg extract were
358 depleted by three rounds of gentle rotation with one volume of antibody-bound beads for 1 hr at
359 4°C. For NEIL3 depletions, 2.5 volumes of 1 mg/mL affinity-purified antibodies against NEIL3
360 were gently rotated with 1 volume of protein A Sepharose beads overnight at 4°C. Five volumes
361 of egg extract were depleted by three rounds of gentle rotation with one volume of antibody-bound
362 beads for 20 min at room temperature. For FANCD2 and NEIL3 double depletion, 3 volumes of
363 1 mg/mL affinity-purified antibodies against NEIL3 were gently rotated with 1 volume of protein
364 A Sepharose beads for 2 hr at 4°C. Three volumes FANCD2 anti-serum were then added to the
365 protein A Sepharose beads and incubation was continued at 4°C overnight. Five volumes of egg

366 extract were depleted by three rounds of gentle rotation with one volume of antibody-bound beads
367 for 20 min at room temperature.

368 **Replication Intermediate Analysis**

369 Replication reactions were stopped at the indicated time points with 10 volumes of Stop Solution
370 A (5% SDS, 80 mM Tris-HCl [pH 8], 0.13% phosphoric acid, 10% Ficoll, and 0.5% bromophenol
371 blue). The reactions were treated with 4 mg/ml Proteinase K (Roche) for 1 hr at 37°C and resolved
372 by 0.8% native agarose gel electrophoresis. The gels were then dried and visualized by
373 phosphorimaging on a Typhoon FLA 7000 (GE Healthcare).

374 **Nascent Strand Analysis**

375 Replication reactions were stopped at the indicated time points with 10 volumes of Stop Solution
376 B (0.5% SDS, 50 mM Tris-HCl [pH 7.5], and 25 mM EDTA [pH 8.0]). The reactions were treated
377 with 0.16 mg/ml RNase A for 1 hr at 37°C, followed by 0.75 mg/ml Proteinase K overnight at
378 room temperature. The reactions were then phenol/chloroform extracted, precipitated, and digested
379 with AflIII for 3 hr at 37°C. After addition of denaturing PAGE Gel Loading Buffer II (Life
380 Technologies), the radiolabeled nascent strands were resolved on a 7% denaturing polyacrylamide
381 gel, transferred to filter paper, dried, and visualized by phosphorimaging on a Typhoon FLA 7000
382 (GE Healthcare). Sequencing gel markers were generating using the Thermo Sequenase Cycle
383 Sequencing Kit (USB Corporation) with primer pICL_Seq that anneals with the pICL plasmids
384 149 nucleotides upstream of the crosslink.

385 **Plasmid Pull-down**

386 Plasmid pull-downs were performed essentially as described³². Briefly, streptavidin-coupled
387 magnetic beads (Invitrogen) were gently rotated with biotinylated LacR²⁸ for 40 min at room

388 temperature. The beads were washed three times with 20 mM HEPES-KOH (pH 7.7), 100 mM
389 KCl, 5 mM MgCl₂, 250 mM sucrose, 0.25 mg/ml BSA, and 0.02% Tween-20, then resuspended
390 in the same buffer. Replication reactions were mixed with the beads at the indicated times and
391 gently rotated for 30 min at 4°C. The beads were washed three times with 20 mM HEPES-KOH
392 (pH 7.7), 100 mM KCl, 5 mM MgCl₂, 0.25 mg/ml BSA, and 0.03% Tween-20, then resuspended
393 in 2x Laemmli buffer for analysis by immunoblotting.

394 **Ubiquitin linkage analysis**

395 Analysis of ubiquitin chains on MCM7 was performed using UbiCrest deubiquitinase enzyme set
396 (Boston Biochem). Plasmid pull downs were performed as described above, except that the beads
397 were resuspended in 1x DUB reaction buffer and then incubated with 1x USP2, 2x GST-AMSH,
398 or ~8 μM Otubain1 (OTUB1) for 2 h at 37 °C. Reactions were quenched with an equal volume 2x
399 Laemmli buffer and analyzed by immunoblotting.

400 **Immunoblotting**

401 Samples were resolved on Mini-PROTEAN or Criterion TGX precast gels (Bio-Rad) and
402 transferred to PVDF membranes (Perkin Elmer). Membranes were blocked in 5% nonfat milk in
403 1x PBST for 60 min at room temperature, then incubated with antibody diluted in 1x PBST
404 containing 1% BSA overnight at 4°C. After extensive washing in 1x PBST at room temperature,
405 the membranes were incubated with goat anti-rabbit horseradish peroxidase-conjugated antibodies
406 (Jackson ImmunoResearch) diluted in 5% nonfat milk in 1x PBST for 1 hr at room temperature.
407 Membranes were washed extensively in 1x PBST, briefly incubated with HyGLO
408 chemiluminescent HRP antibody detection reagent (Denville), and imaged using an Amersham
409 Imager 600 (GE Healthcare).

410 **Error-Free Repair Assay**

411 The error-free repair assay was performed as previously described³³. Briefly, replication reactions
412 were stopped at the indicated time points with 10 volumes of Stop Solution B. The reactions were
413 treated with 0.16 mg/ml RNase A for 1 hr at 37°C, followed by 0.75 mg/ml Proteinase K overnight
414 at room temperature. The reactions were then phenol/chloroform extracted, precipitated, and
415 digested with HincII or HincII and SapI for 3 hr at 37°C. After addition of 0.17 volumes of DNA
416 loading buffer (10 mM Tris-HCl [pH 7.5], 60% glycerol, and 0.5% bromophenol blue), the
417 digestion products were resolved by 0.8% native agarose gel electrophoresis, dried, and visualized
418 by phosphorimaging on a Typhoon FLA 7000 (GE Healthcare). Repair products were quantified
419 using ImageJ (NIH).

420 **Purification of Recombinant *Xenopus* NEIL3 and TRAIP**

421 *X. laevis* NEIL3 was purified as previously described¹. Briefly, constructs for expression of
422 rNEIL3^{NZF-C to A}, rNEIL3^{TL310-311LV}, rNEIL3^{K500E}, rNEIL3^{K546E}, rNEIL3^{K500E K546E}, and rNEIL3^{Δ92}
423 were prepared by digesting Integrated DNA Technologies gene blocks encompassing the C-
424 terminal domain of NEIL3 (with FLAG epitope tag) and containing the indicated mutations with
425 BbvCI and XhoI and then ligating the fragments into similarly digested pFastBac1-NEIL3-FLAG¹.
426 The rNEIL3^{Δ291} expression construct was prepared by PCR amplifying the NEIL3 glycosylase
427 domain from a *X. laevis* cDNA library (a gift from T.G.W. Graham) using primers NEIL3_291_A
428 and NEIL3_291_B. The fragment was then digested with EcoRI and XhoI and ligated into
429 similarly digested pFastBac1 (Thermo Fisher Scientific). All mutations and truncations were
430 confirmed by Sanger sequencing. Baculoviruses expressing rNEIL3 were then prepared using
431 the Bac-to-Bac system (Thermo Fisher Scientific) according to the manufacturer's protocols.
432 rNEIL3 protein was expressed in 250 ml suspension cultures of Sf9 insect cells (Expression

433 Systems) by infection with baculovirus expressing NEIL3-FLAG for 48 to 72 hr. Sf9 cells were
434 collected and suspended in 10 ml NEIL3 Lysis Buffer (50 mM Tris-HCl [pH 7.5], 300 mM NaCl,
435 10% glycerol, 1x Roche EDTA-free cOmplete protease inhibitor cocktail, 0.5 mM PMSF, and
436 0.2% Triton X-100). Cells were lysed by sonication, and the soluble fraction was collected by
437 spinning the lysate at 25,000 rpm in a Beckman SW41 rotor for 1 hr. The soluble lysate was
438 incubated with 200 μ l anti-FLAG M2 affinity resin (Sigma) for 90 min at 4°C. The resin was
439 washed once with 10 ml Lysis Buffer, twice with NEIL3 Wash Buffer (50 mM Tris-HCl [pH 7.5],
440 300 mM NaCl, 10% glycerol, and 0.2% Triton X-100), and three times with Buffer A (50 mM
441 Tris-HCl [pH 7.5], 300 mM NaCl, and 10% glycerol). NEIL3-FLAG protein was eluted from the
442 resin with Buffer A containing 100 μ g/ml 3x FLAG peptide (Sigma). Elution fractions containing
443 NEIL3-FLAG protein were pooled and dialyzed against 50 mM HEPES-KOH (pH 7.0), 300 mM
444 NaCl, 1 mM DTT, and 20% glycerol at 4°C for 12 hr and then dialyzed against 50 mM HEPES-
445 KOH (pH 7.0), 150 mM NaCl, 1 mM DTT, and 15% glycerol at 4°C for 3 hr. Aliquots of protein
446 were stored at -80°C. Constructs for expression of GST-TEV-NZF fusion proteins were prepared
447 by PCR amplifying the NEIL3 NZF from pFastBac1-NEIL3-FLAG and pFastBac1-NEIL3^{TL310-}
448 ^{311LV}-FLAG using primers NEIL3_NZF_A and NEIL3_NZF_B. The pGEX-6P-1 backbone (with
449 GST-TEV tag) was PCR amplified from pGEX-6P-1-GST-TEV-FLAG-UBXN7 with primers
450 GST_A and GST_B. The resulting fragments were then assembled using the NEBuilder HiFi DNA
451 assembly cloning kit (New England Biolabs) according to the manufacturer's instructions.
452 Expression of GST-TEV-NZF proteins was induced in 1 L Rosetta 2 (DE3) pLysS cells (Novagen)
453 with 0.5 mM IPTG for 3 hr at 37°C. Bacterial cell pellets were suspended in Buffer A (10 mM
454 Sodium Phosphate [pH 7.4], 150 mM NaCl, 5 mM β -mercaptoethanol, 10 μ M ZnCl₂ and 1x Roche
455 cOmplete protease inhibitor cocktail) and sonicated. The soluble lysate was collected following

456 centrifugation at 25,000 rpm in SW40.1 rotor for 1 hr and bound to Glutathione Sepharose 4B (GE
457 Healthcare) for 1.5 hr at 4°C. The bound resin was then washed five times with Buffer A and
458 protein was eluted with Buffer B (50 mM Tris-HCl [pH 8.0], 150 mM NaCl, 10 µM ZnCl₂, 5 mM
459 β-mercaptoethanol, and 20 mM glutathione). Fractions containing GST-TEV-NZF fusion proteins
460 were dialyzed against 50 mM Tris-HCl (pH 8.0), 150 mM NaCl, 10 µM ZnCl₂, 5 mM β-
461 mercaptoethanol, and 10% glycerol at 4°C and aliquots were stored at -80°C. Constructs for
462 expression of MBP-TEV-GRF ZF fusion proteins were prepared by amplifying the NEIL3 GRF
463 ZF1 or GRF ZF2 from pFastBac1-NEIL3-FLAG or pFastBac1-NEIL3^{K500E K546E}-FLAG using
464 primers GRFZF1_A and GRFZF1_B or GRFZF2_A and GRFZF2_B, respectively. The MBP tag
465 was PCR amplified using the primers MBP_A and MBP_B or MBP_A and MBP_C for GRF ZF1
466 and GRF ZF2 respectively. The pGEX-6P-1 backbone was PCR amplified from pGEX-6P-1-GST-
467 TEV-FLAG-UBXN7 with primers pGEX_A and pGEX_B. The resulting fragments were then
468 assembled using the NEBuilder HiFi DNA assembly cloning kit (New England Biolabs) according
469 to the manufacturer's instructions. Expression of MBP-TEV-GRF ZF proteins was induced in 1 L
470 Rosetta 2 (DE3) pLysS cells (Novagen) with 0.5 mM IPTG for 3 hr at 37°C. Bacterial cell pellets
471 were suspended in Buffer C (20 mM Tris-HCl [pH 7.5], 300 mM NaCl, 1 mM DTT, and 1x Roche
472 cOmplete protease inhibitor cocktail) and sonicated. The soluble lysate was collected following
473 centrifugation at 25,000 rpm in a SW40.1 rotor for 1 hr and bound to amylose resin (New England
474 Biolabs) for 1.5 hr at 4°C. The bound resin was then washed six times with Buffer C and protein
475 was eluted with Buffer C containing 10 mM maltose. Fractions containing MBP-TEV-GRF ZF
476 fusion proteins were dialyzed against 20 mM Tris-HCl (pH 8.0), 200 mM NaCl, 1 mM DTT, and
477 10% glycerol at 4°C and aliquots were stored at -80°C.

478 The *X. laevis* TRAIP ORF was PCR amplified from a *X. laevis* cDNA library (a gift from
479 T.G.W. Graham) using primers TRAIP_A and TRAIP_B. The amplified product was gel isolated,
480 digested with BamHI, and ligated into pH₆-SUMO³⁴ linearized with BamHI. The R18C
481 substitution was introduced by “around-the-horn” PCR³⁵ using primers R18C_A and R18C_B.
482 pH₆-SUMO-TRAIP^{ΔPIP} (residues 1-455) was constructed by “around-the-horn” PCR using primers
483 PIP_A and PIP_B. His₆-SUMO-TRAIP was expressed in Rosetta 2 (DE3) pLysS (Novagen) by
484 induction with 0.1 mM IPTG overnight at 16°C in growth media supplemented with 50 μM ZnSO₄.
485 Bacterial pellets were resuspended in TRAIP Lysis Buffer (20 mM HEPES-NaOH [pH 7.5], 400
486 mM sodium acetate, 10% glycerol, 20 mM imidazole, 10 μM ZnSO₄, 0.1% NP-40, 1 mM DTT,
487 and 1x Roche cOmplete protease inhibitor cocktail). Following sonication, ammonium sulfate and
488 polyethyleneimine were added to the lysate to final concentrations of 300 mM and 0.45%,
489 respectively and incubated for 15 min at 4°C. The soluble fraction was collected after
490 centrifugation at 40,000g for 45 min at 4°C, and precipitated with saturating ammonium sulfate.
491 The precipitated fraction was collected after centrifugation at 40,000g for 45 min at 4°C,
492 resuspended in Lysis Buffer, and then rotated with NiNTA resin (Qiagen) for 30 min at room
493 temperature. The resin was washed three times with Wash Buffer (20 mM HEPES-NaOH [pH
494 7.5], 400 mM sodium acetate, 10% glycerol, 20 mM imidazole, 10 μM ZnSO₄, 0.01% NP-40, 1
495 mM DTT, and 1x Roche cOmplete protease inhibitor cocktail). His₆-SUMO-TRAIP was eluted
496 from the resin with Elution Buffer (20 mM HEPES-NaOH [pH 7.5], 400 mM sodium acetate, 10%
497 glycerol, 250 mM imidazole, 0.01% NP-40, and 1 mM DTT). Elution fractions containing His₆-
498 SUMO-TRAIP were pooled and dialyzed against Dialysis Buffer (20 mM HEPES-NaOH [pH 7.5],
499 400 mM sodium acetate, 10% glycerol, 120 mM imidazole, 0.01% NP-40, and 1 mM DTT)
500 overnight at 4°C. With the exception of the proteins used in Fig. 2c and Extended Data Fig. 6, the

501 His₆-SUMO was simultaneously cleaved by addition of 0.03 mg/mL Ulp1 during dialysis.
502 Aliquots were flash frozen and stored at -80°C.

503 **Ubiquitin Ligase Activity Assay**

504 The ubiquitin ligase activity assay using an equimolar mixture of the E2 ubiquitin conjugating
505 enzymes UbcH5a, UbcH5b, and UbcH5c and recombinant TRAIP^{WT} or TRAIP^{R18C} at an
506 approximate final concentration of 70 nM was performed using the Enzo BML-UW9920
507 Ubiquitylation Kit according to manufacturer's instructions (Enzo Life Sciences).

508 **Electron Microscopy**

509 Electron microscopy analysis of the replication intermediates was performed as previously
510 described⁸. Briefly, replication reactions were stopped at 90 min with 10 volumes of Stop Solution
511 C (100 mM Tris-HCl [pH 7.5], 6.7 mM MgCl₂, 1 mM EDTA [pH 8.0], and 1% SDS). The DNA
512 was crosslinked with trimethylpsoralen (Sigma) and irradiation with UV light at 365 nm prior to
513 protein extraction and DNA purification. Purified DNA was incubated with E. coli single-stranded
514 DNA binding protein (SSB), fixed with 0.3% glutaraldehyde, then purified by size-exclusion
515 chromatography. Eluted complexes were mounted onto grids, which were then subjected to rotary
516 shadowing with platinum and carbon coating using a Leica Ace600 coating system. Samples were
517 imaged using a JEOL 1200EX transmission electron microscope equipped with a 2k CCD camera
518 (Advanced Microscopy Techniques). After blinding the scorer to the conditions, reversed forks
519 were counted and expressed as a percentage of pre-incision structures, which was then normalized
520 to the mock-depleted condition.

521 **Electrophoretic Mobility Shift Assay**

522 MBP-TEV-GRF ZF fusion protein was incubated with 10 nM 5' end radiolabeled 25mer ssDNA
523 (EMSA_Top) or dsDNA (EMSA_Top + EMSA_Bottom) in buffer containing 1 mM MgCl₂, 100
524 μM ZnSO₄, 10 mM Tris-HCl (pH 8.0), 50 mM NaCl, 0.2 mM TCEP, and 5% glycerol for 30 to
525 60 min at 4 °C. Binding reactions were separated on native 5% acrylamide (37.5:1), 45 mM Tris,
526 45 mM borate, 1 mM MgCl₂, 100 μM ZnSO₄ gels and visualized by phosphorimaging on a
527 Typhoon FLA 7000 (GE Healthcare).

528 **NEIL3 Glycosylase Assay**

529 AP-ICLs between complementary DNA and DNA/RNA chimeric oligonucleotides AP_assay_A
530 and AP_assay_B were cross-linked, RNase digested, and gel purified as described¹. To monitor
531 unhooking of AP-ICLs, 2.5 nM 5' radiolabeled cross-linked substrate was incubated with 20 nM
532 rNEIL3-FLAG in 20 mM HEPES-KOH (pH 7.0), 50 mM NaCl, 1 mM DTT, 0.1 mg/ml BSA at
533 37°C³⁶. Reactions were quenched with 1 volume of 2x formamide buffer (86% formamide, 2x
534 TBE, 20 mM EDTA [pH 8.0]), separated on a denaturing polyacrylamide and visualized by
535 phosphorimaging on a Typhoon FLA 7000 (GE Healthcare).

536 **Biolayer Interferometry**

537 All measurements were obtained using an OctetRED384 instrument (Pall ForteBio). Samples in
538 0.2 mL BLI buffer (1x PBS, 0.1 mg/mL BSA, and 0.05% Tween 20) were dispensed into
539 polypropylene 96-well black flat-bottom plates (Greiner Bio-One). GST-TEV-NZF or GST
540 control protein (30 μg/mL) was captured on pre-wet anti-GST biosensors (Pall ForteBio).
541 Biosensors were then transferred to wells containing BLI buffer to allow dissociation of non-
542 specifically bound GST-TEV-NZF protein and establish a measurement base-line. Biosensors
543 were next transferred to wells containing serial dilutions of monoubiquitin (Boston Biochem) to
544 monitor association of ubiquitin with the immobilized GST-TEV-NZF protein. Finally, biosensors

545 were transferred to wells containing BLI buffer to monitor dissociation of ubiquitin from GST-
546 TEV-NZF protein. For each ubiquitin concentration, the steady state ubiquitin binding response
547 (R_{eq}) was determined from a five second window at the end of the association phase. R_{eq} values
548 were subsequently corrected for non-specific binding of ubiquitin to the GST epitope by
549 subtracting R_{eq} values obtained for the GST control protein. Steady-state responses were plotted
550 as a function of ubiquitin concentration ([Ub]) and K_d was determined using the Prism software
551 suite by fitting the data to the non-linear regression equation $R_{eq} = \frac{R_{max} \times [Ub]}{[Ub] + K_d}$ where R_{max} is the
552 globally-constrained maximum association response.

553 **Cell Lines**

554 Wild-type and $NEIL3^{KO}$ HAP1 near-haploid human cells were purchased from Horizon Discovery
555 and cultured at 37°C and 5% CO₂ in IMDM (Gibco) supplemented with 10% fetal calf serum
556 (Gibco) and penicillin/streptomycin (Gibco). $NEIL3^{KO}$ cells were confirmed by immunoblotting
557 against NEIL3. For targeting of *FANCL*, WT and $NEIL3^{KO}$ cells were transfected with Turbofectin
558 8.0 (Origene) and the following plasmids: pX461, *FANCL*_left and *FANCL*_right CRISPR guides
559 in U6 BsaI backbone, and *FANCL*-Puro targeting construct (Extended Data Fig. 13b). *FANCL*
560 plasmids were obtained from the Wellcome Trust Sanger Institute. Two days post-transfection, 3.5
561 µg/mL puromycin (Gibco) was added, and two days later, cells were plated in 96-well plates with
562 puromycin. After 14 days of incubation, individual clones were picked and analyzed for *FANCL*
563 targeting using the SequalPrep Long PCR kit (Applied Biosystems) (see Supplementary Table 1
564 for primer sequences). Targeted clones were then plated with 100 ng/mL mitomycin C (Sigma)
565 overnight and analyzed by immunoblotting for FANCD2. *FANCL* knockouts were identified by
566 failure to ubiquitinate FANCD2. All cell lines were tested to be mycoplasma negative using the
567 MycoAlert Mycoplasma Detection Kit (Lonza).

568 **Colony Survival Assay**

569 For the cisplatin colony survival assay (CSA), HAP1 cells were prepared at 2×10^5 cells/mL. Cells
570 and cisplatin (diluted in culture media) were mixed in 96-well blocks (Greiner Bio-One
571 Masterblock) and foil seals (Bio-Rad Microseal 'F') were applied before culturing cells at 37°C
572 for 2 hr. Cells were then serially diluted in PBS using a multi-channel pipette to obtain 1:10 and
573 1:100 dilutions, and 100 μL of each of three concentrations were plated in duplicate in 24-well
574 plates filled with 1.5 mL of culture media per well. Cells were cultured for 6 days before being
575 stained with crystal violet³⁷ and colonies were quantified by a GelCount colony counter (Oxford
576 Optronix).

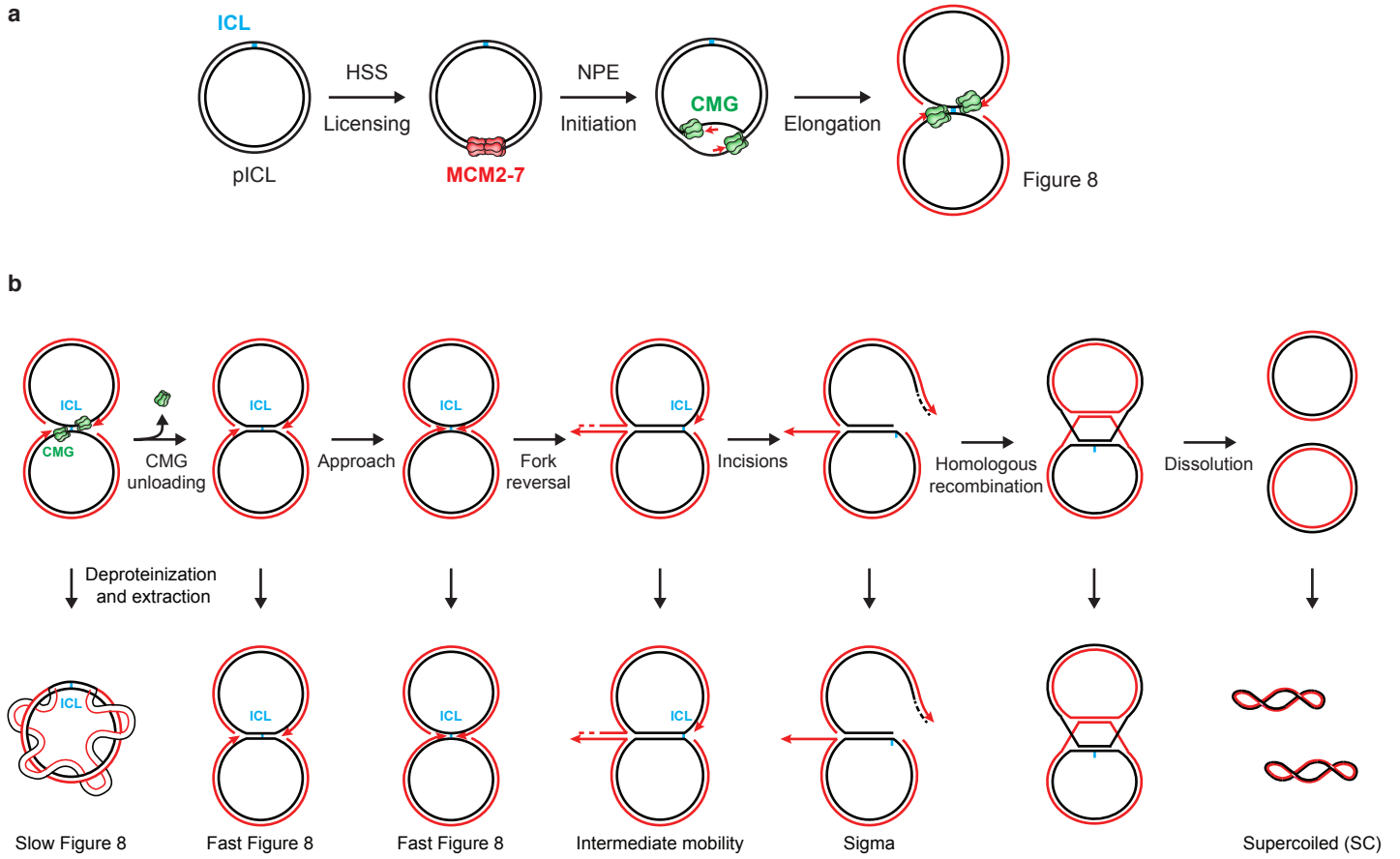
577 For the trioxsalen CSA, cells were seeded in 24-well plates at 1.2×10^5 cells per well 5 hr
578 prior to adding trioxsalen (Sigma) and cultured for 1 hr. Cells were then exposed to 6 kJ/m^2 of
579 UV-A light (365 nm, VL-6.L lamp) through the bottom of the tissue culture plate to photoactivate
580 trioxsalen. The cells were washed twice with culture media, incubated at 37°C for 10 min to offload
581 unbound trioxsalen, then washed again and treated with 12 kJ/min/m^2 UV-A to convert trioxsalen
582 monoadducts into ICLs^{38,39}. Cells were then trypsinized, diluted, plated, cultured, and

583 **References:**

- 584 27 Lebofsky, R., Takahashi, T. & Walter, J. C. DNA replication in nucleus-free *Xenopus*
585 egg extracts. *Methods Mol Biol* **521**, 229-252 (2009).
586 28 Dewar, J. M., Budzowska, M. & Walter, J. C. The mechanism of DNA replication
587 termination in vertebrates. *Nature* **525**, 345-350, doi:10.1038/nature14887 (2015).
588 29 Joukov, V., Chen, J., Fox, E. A., Green, J. B. & Livingston, D. M. Functional
589 communication between endogenous BRCA1 and its partner, BARD1, during *Xenopus*
590 laevis development. *Proc Natl Acad Sci U S A* **98**, 12078-12083 (2001).
591 30 Walter, J. & Newport, J. Initiation of eukaryotic DNA replication: origin unwinding and
592 sequential chromatin association of Cdc45, RPA, and DNA polymerase alpha. *Mol Cell*
593 **5**, 617-627 (2000).
594 31 Rosado, I. V., Langevin, F., Crossan, G. P., Takata, M. & Patel, K. J. Formaldehyde
595 catabolism is essential in cells deficient for the Fanconi anemia DNA-repair pathway.
596 *Nat. Struct. Mol. Biol* **18**, 1432-1434, doi:10.1038/nsmb.2173 (2011).

- 597 32 Budzowska, M., Graham, T. G., Soback, A., Waga, S. & Walter, J. C. Regulation of the
598 Rev1-pol zeta complex during bypass of a DNA interstrand cross-link. *EMBO J* **34**,
599 1971-1985, doi:10.15252/embj.201490878 (2015).
- 600 33 Knipscheer, P., Raschle, M., Scharer, O. D. & Walter, J. C. Replication-coupled DNA
601 interstrand cross-link repair in *Xenopus* egg extracts. *Methods Mol Biol* **920**, 221-243,
602 doi:10.1007/978-1-61779-998-3_16 (2012).
- 603 34 Graham, T. G., Walter, J. C. & Loparo, J. J. Two-Stage Synapsis of DNA Ends during
604 Non-homologous End Joining. *Mol Cell* **61**, 850-858, doi:10.1016/j.molcel.2016.02.010
605 (2016).
- 606 35 Hemsley, A., Arnheim, N., Toney, M. D., Cortopassi, G. & Galas, D. J. A simple method
607 for site-directed mutagenesis using the polymerase chain reaction. *Nucleic Acids Res* **17**,
608 6545-6551 (1989).
- 609 36 Liu, M. *et al.* The mouse ortholog of NEIL3 is a functional DNA glycosylase in vitro and
610 in vivo. *Proc Natl Acad Sci U S A* **107**, 4925-4930, doi:10.1073/pnas.0908307107 (2010).
- 611 37 Franken, N. A., Rodermond, H. M., Stap, J., Haveman, J. & van Bree, C. Clonogenic
612 assay of cells in vitro. *Nat Protoc* **1**, 2315-2319, doi:10.1038/nprot.2006.339 (2006).
- 613 38 Vos, J. M. & Hanawalt, P. C. Processing of psoralen adducts in an active human gene:
614 repair and replication of DNA containing monoadducts and interstrand cross-links. *Cell*
615 **50**, 789-799 (1987).
- 616 39 Derheimer, F. A., Hicks, J. K., Paulsen, M. T., Canman, C. E. & Ljungman, M. Psoralen-
617 induced DNA interstrand cross-links block transcription and induce p53 in an ataxia-
618 telangiectasia and rad3-related-dependent manner. *Mol Pharmacol* **75**, 599-607,
619 doi:10.1124/mol.108.051698 (2009).

Extended Data Fig. 1

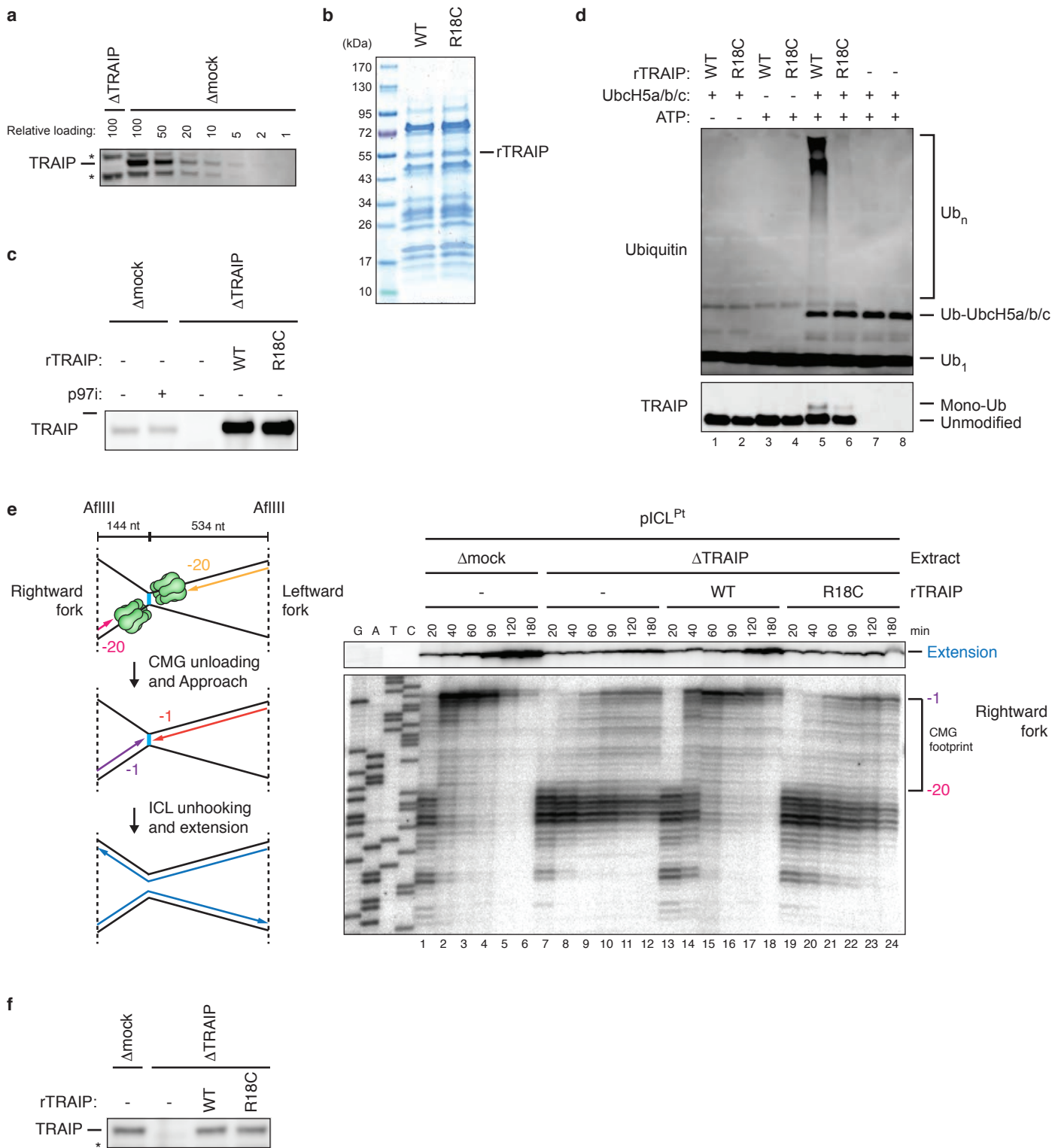


1 **Extended Data Fig. 1 | DNA replication and cisplatin-ICL repair in *Xenopus* egg extracts**

2 **a**, Schematic of pICL replication in the nucleus-free *Xenopus* egg extract system⁴⁰. Incubation of
3 the plasmid in HSS supports the recruitment of inactive MCM2-7 double hexamers (red hexamers;
4 “Licensing”). Addition of NPE activates replication initiation, including the assembly of active
5 CMG helicases (green hexamers), and elongation of nascent strands (red lines).

6 **b**, Intermediates generated during replication-coupled repair of a cisplatin-ICL. Top, progression
7 through the incision-dependent Fanconi anemia repair pathway generates distinct intermediates
8 resulting from fork convergence, CMG unloading, leading strand approach to the ICL, fork
9 reversal, incisions, and repair of the double strand break by homologous recombination. Bottom,
10 deproteinization of the DNA intermediates depicted along the top yields DNA structures that travel
11 with characteristic mobilities during native agarose gel electrophoresis, as indicated along the side
12 of the gel in Fig. 1b. The slow Figure 8 arises upon fork convergence on the ICL. Conversion of
13 slow to fast Figure 8s results from CMG unloading and an accompanying change in plasmid
14 topology⁸. Next, a species of intermediate mobility appears (Fig. 1b, green arrowhead), which
15 represents reversed forks, as shown by electron microscopy⁸. Following XPF-dependent
16 unhooking of the reversed structure^{8,41}, double-strand DNA break repair generates joining products
17 that barely enter the gel¹⁸ (Fig, 1b, Well product). Some of these species are resolved into
18 monomeric, supercoiled plasmids that represent the final, fully repaired product (Fig. 1b, SC) that
19 is sensitive to SapI digestion.

Extended Data Fig. 2



20 **Extended Data Fig. 2 | Recombinant TRAIP supports the disappearance of the CMG**
21 **footprint at cisplatin-ICLs**

22 **a**, NPE immunodepleted of TRAIP was loaded alongside a dilution series of mock-depleted NPE
23 and blotted for TRAIP. A relative loading amount of 100 corresponds to 2 μ l of NPE. Non-
24 specifically detected proteins are marked with asterisks.

25 **b**, Bacterially-expressed rTRAIP^{WT} and rTRAIP^{R18C}. The recombinant proteins were partially
26 purified, resolved by SDS-PAGE, and visualized with Coomassie Brilliant Blue staining.

27 **c**, Mock- and TRAIP-depleted extracts supplemented with rTRAIP^{WT} or rTRAIP^{R18C} used in the
28 replication reaction shown in Fig. 1b were analyzed as in **a**. The lack of non-specific bands may
29 be due to shorter incubation with the TRAIP antibody.

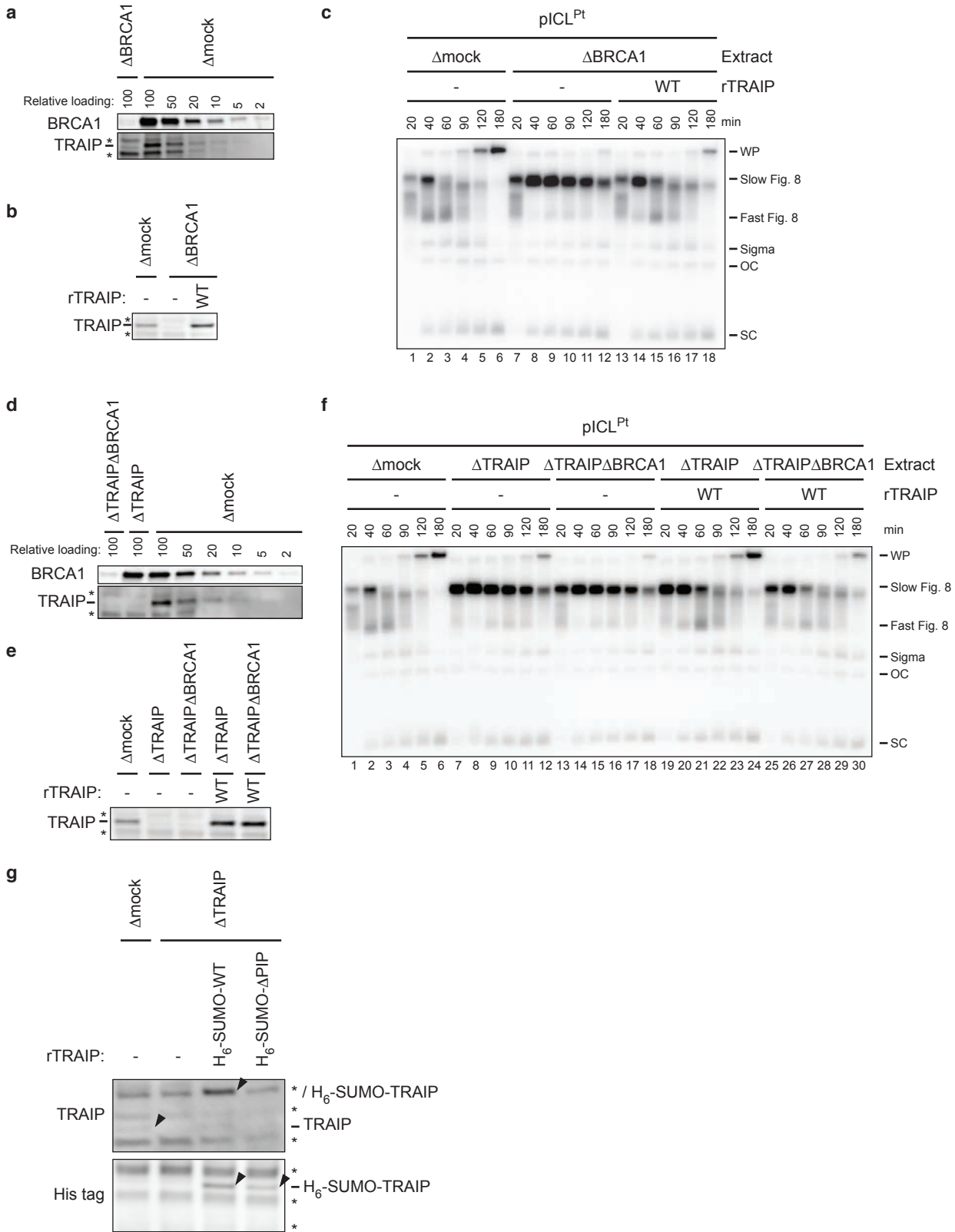
30 **d**, Ubiquitin ligase activity of the rTRAIP shown in **b**. Recombinant TRAIP^{WT} or rTRAIP^{R18C} was
31 combined with ubiquitin, E1, three E2s (UbcH5a, UbcH5b, and UbcH5c), and ATP as indicated.
32 Polyubiquitin chain synthesis (top gel) and TRAIP autoubiquitylation (bottom gel) were detected
33 by immunoblotting the reactions with ubiquitin and TRAIP antibody, respectively.

34 **e**, Left, schematic of nascent strands generated at ICLs. When forks converge on an ICL, nascent
35 strands stall ~20 nt from the ICL on either side of the lesion due to the footprint of CMG (green
36 hexamer). AflIII cuts 144 nt to the left of the ICL and 534 nt to the right of the ICL, generating
37 characteristic products for the leftward and rightward leading strands upon fork convergence,
38 CMG unloading, and leading strand extension. Right, nascent strand analysis of pICL^{Pt} replication
39 in the indicated extracts. After replication with [α -³²P]dATP and AflIII digestion, nascent strands
40 were extracted and resolved on a denaturing polyacrylamide gel alongside a sequencing ladder and
41 visualized by autoradiography. Top, extension products. Bottom, nascent strands of the rightward
42 fork. As seen previously^{2,42}, when replication forks converged on the ICL in mock-depleted egg

43 extracts, leading strands initially stalled 20-40 nucleotides (nt) from the lesion (lane 1) and then
44 advanced to the -1 position (lanes 2-6), which depends on CMG dissociation^{18,42}. In contrast, in
45 TRAIIP-depleted egg extracts, the -20 footprint persisted for three hours (lanes 7-12). The same
46 defect was seen for the leftward fork (data not shown). This effect was rescued with rTRAIIP^{WT}
47 but not rTRAIIP^{R18C} (lanes 13-24).

48 **f**, Mock- and TRAIIP-depleted extracts supplemented with rTRAIIP^{WT} or rTRAIIP^{R18C} used in the
49 replication reaction shown in **e** were analyzed as in **a**.

Extended Data Fig. 3



50 **Extended Data Fig. 3 | BRCA1 and the TRAIPI PIP box do not contribute to CMG unloading**
51 **at ICLs**

52 We previously showed that the immunodepletion of BRCA1 from egg extracts inhibits CMG
53 unloading at ICLs, but this defect could not be rescued with recombinant BRCA1-BARD1
54 complex^{7,18}.

55 **a**, To test whether TRAIPI is co-depleted with BRCA1, NPE was immunodepleted of BRCA1,
56 loaded alongside a dilution series of mock-depleted NPE, and blotted for BRCA1 and TRAIPI. A
57 relative loading amount of 100 corresponds to 2 μ l of NPE. Non-specifically detected proteins are
58 marked with asterisks. This analysis revealed that immunodepletion of BRCA1 co-depletes TRAIPI
59 from NPE.

60 **b**, Mock- or BRCA1-depleted extracts supplemented with rTRAIPI^{WT} were blotted for TRAIPI.

61 **c**, pICL^{Pt} was replicated in the indicated egg extracts with [α -³²P]dATP and analyzed as in Fig.
62 1b. rTRAIPI^{WT} suppressed the stabilization of the slow Figure 8 species seen in BRCA1-depleted
63 extract, consistent with the restoration of CMG unloading.

64 **d**, To determine whether TRAIPI-dependent CMG unloading is enhanced by BRCA1, NPE was
65 immunodepleted of TRAIPI or TRAIPI and BRCA1. A dilution series of mock-depleted NPE was
66 loaded alongside the depleted extracts, and extracts were blotted for BRCA1 and TRAIPI. A
67 relative loading amount of 100 corresponds to 2 μ l of NPE.

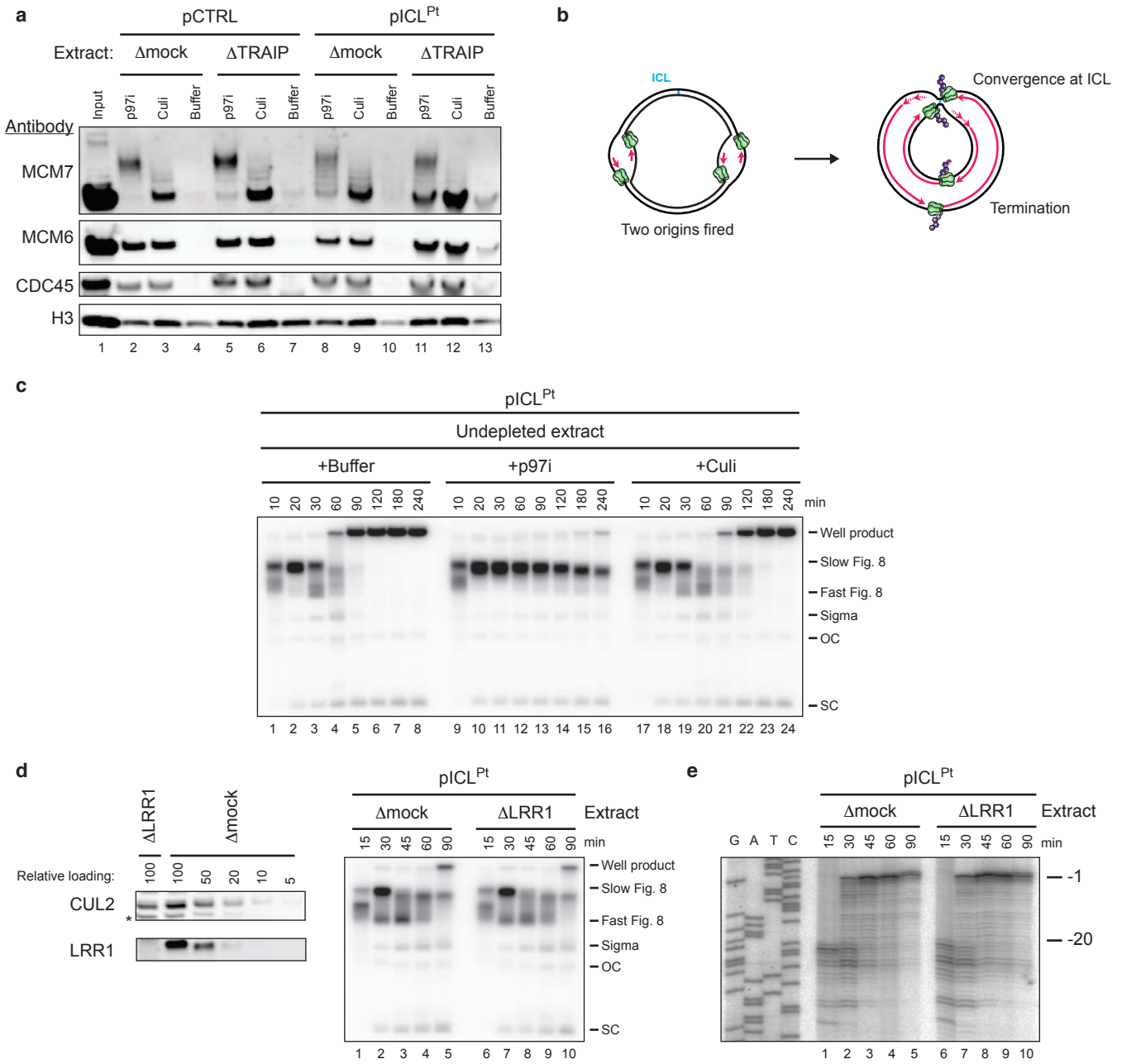
68 **e**, Extracts in **d** were supplemented with rTRAIPI^{WT}, as indicated, and blotted for TRAIPI.

69 **f**, pICL^{Pt} was replicated in the indicated egg extracts with [α -³²P]dATP and analyzed as in Fig. 1b.
70 rTRAIPI^{WT} suppressed the accumulation of slow Figure 8s to a similar extent in the presence and
71 absence of BRCA1 (lanes 19-30), indicating that BRCA1 is not needed to support TRAIPI function.

72 Notably, we have observed that TRAIP is co-depleted with other proteins (data not shown),
73 suggesting it interacts non-specifically with different antibodies.

74 **g**, Mock- and TRAIP-depleted egg extracts supplemented with His₆-SUMO-rTRAIP^{WT} or His₆-
75 SUMO-rTRAIP^{ΔPIP}, used in replication reaction shown in Fig. 2c, were blotted for TRAIP (top)
76 or the His₆-tag (bottom). Black arrowheads, TRAIP-specific bands. His₆-SUMO-rTRAIP co-
77 migrates with a non-specific band in the TRAIP blot. His₆-SUMO-rTRAIP^{ΔPIP} is not detectable by
78 the TRAIP antibody because it lacks the C-terminal epitope used to generate the antibody. Blotting
79 for the N-terminal His₆ tag detected both forms of rTRAIP. Non-specifically detected proteins are
80 marked with asterisks.

Extended Data Fig. 4



81 **Extended Data Fig. 4 | TRAIP and CRL2^{LRR1} promote distinct CMG unloading pathways**

82 **a**, To determine whether TRAIP is required for CMG unloading during replication termination,
83 we analyzed proteins associated with pICL^{Pt} or pCTRL 60 min after replication initiation in mock-
84 or TRAIP-depleted extracts containing p97i or Culi, as indicated. Chromatin was recovered and
85 blotted for the indicated proteins. In the absence of TRAIP, CMG unloading from pICL^{Pt} was
86 inhibited compared to the mock-depleted control (compare lanes 10 and 13), as shown in Fig. 1c.
87 In contrast, CMG unloading from pCTRL was unaffected by TRAIP depletion (compare lanes 4
88 and 7). Similarly, in the presence of p97i, TRAIP was not required for MCM7 ubiquitylation on
89 pCTRL (compare lanes 2 and 5), while it was essential for efficient MCM7 ubiquitylation on
90 pICL^{Pt} (compare lanes 8 and 11, note the greater level of unmodified MCM7 in lane 11). The
91 residual MCM7 ubiquitylation observed on pICL^{Pt} in the absence of TRAIP was likely the result
92 of termination events that occurred elsewhere on the plasmid (see **b**).

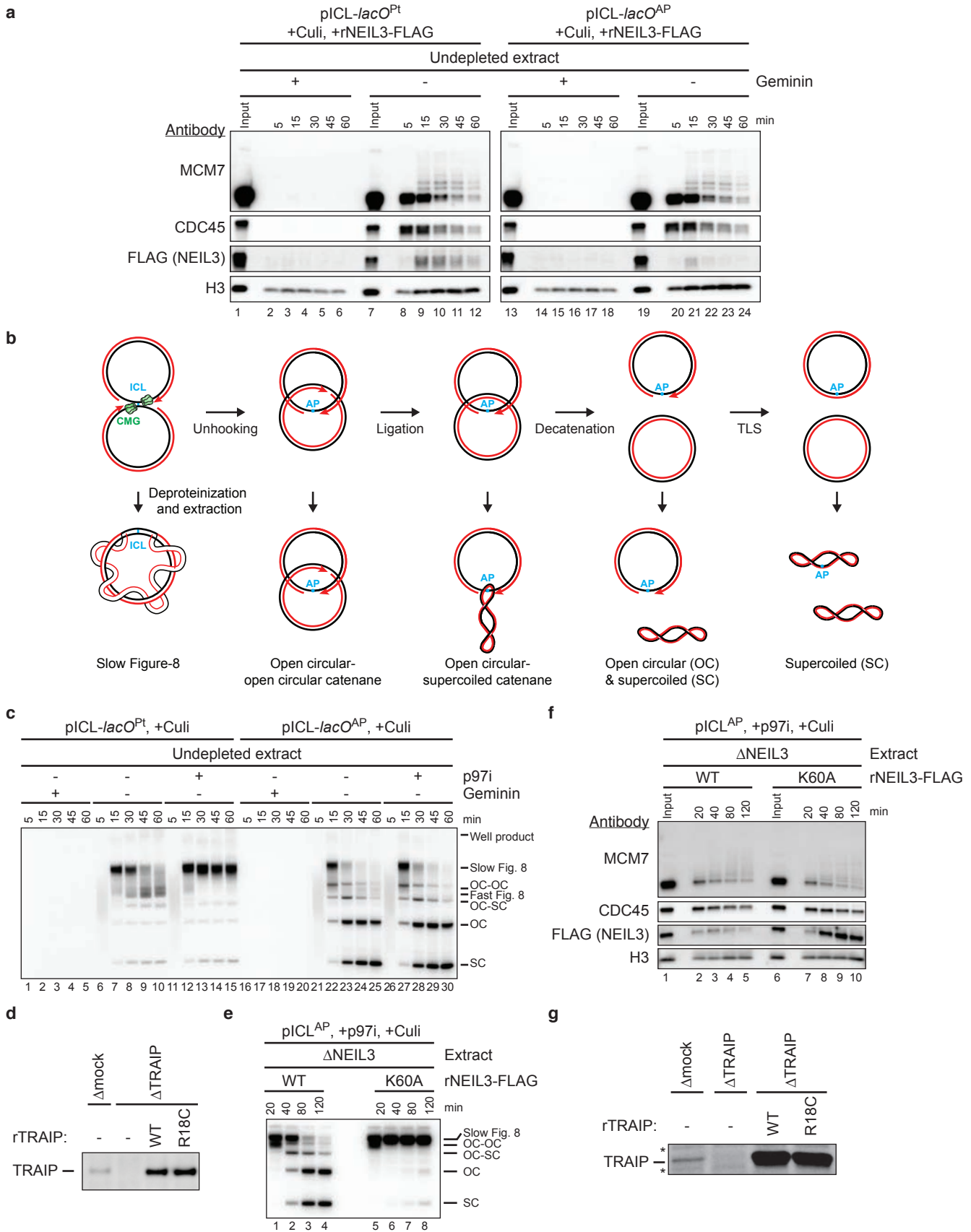
93 **b**, If two origins fire on a single plasmid, one pair of replication forks converges at the ICL and
94 undergoes TRAIP-dependent CMG unloading whereas a second pair undergoes normal replication
95 termination where CMG unloading depends on CRL2^{LRR1}. Both pairs of CMGs (green) should
96 undergo ubiquitylation (purple).

97 **c**, pICL^{Pt} was replicated in extract with p97i or Culi and analyzed as in Fig. 1b. Culi had no
98 significant effect on the accumulation of fast Figure 8 structures, consistent with CRL2^{LRR1} being
99 dispensable for CMG unloading at ICLs.

100 **d**, Left, to assess the effect of LRR1 depletion on CMG unloading, NPE was immunodepleted of
101 LRR1, loaded alongside a dilution series of mock-depleted NPE, and blotted for LRR1 and CUL2.
102 A relative loading amount of 100 corresponds to 2 μ l of NPE. Non-specifically detected protein is
103 marked with an asterisk. Right, pICL^{Pt} was replicated in mock- or LRR1-depleted egg extracts and

104 analyzed as in Fig. 1b. The absence of LRR1 had no effect on the formation of fast Figure 8
105 structures, supporting the idea that CRL2^{LRR1} is dispensable for CMG unloading at ICLs.
106 e, Nascent strand analysis of pICL^{Pt} replicating in mock- or LRR1-depleted extracts was performed
107 as in Extended Data Fig. 2e. The CMG footprint disappeared with normal kinetics at the ICL in
108 LRR1-depleted egg extract, consistent with CRL2^{LRR1} not being required for CMG unloading at
109 ICLs.

Extended Data Fig. 5



110 **Extended Data Fig. 5 | AP-ICL repair by NEIL3 in *Xenopus* egg extracts**

111 **a**, Analysis of chromatin-associated proteins during replication of pICL-*lacO*^{Pt} or pICL-*lacO*^{AP} in
112 the indicated extract. At different times after replication initiation, chromatin was recovered and
113 blotted for the indicated proteins.

114 **b**, Intermediates generated during replication-coupled repair of an AP-ICL. Top, progression
115 through the NEIL3 repair pathway generates intermediates resulting from fork convergence,
116 NEIL3-dependent *N*-glycosyl bond cleavage, nascent strand ligation, decatenation, and translesion
117 synthesis (TLS). Bottom, deproteinization of the DNA intermediates depicted along the top yields
118 DNA structures that travel with characteristic mobilities during native gel electrophoresis, as
119 indicated alongside of the gel in Fig. 3a.

120 **c**, pICL-*lacO*^{Pt} and pICL-*lacO*^{AP} were replicated in extract supplemented with geminin, p97i, and
121 Culi and analyzed as in Fig. 1b.

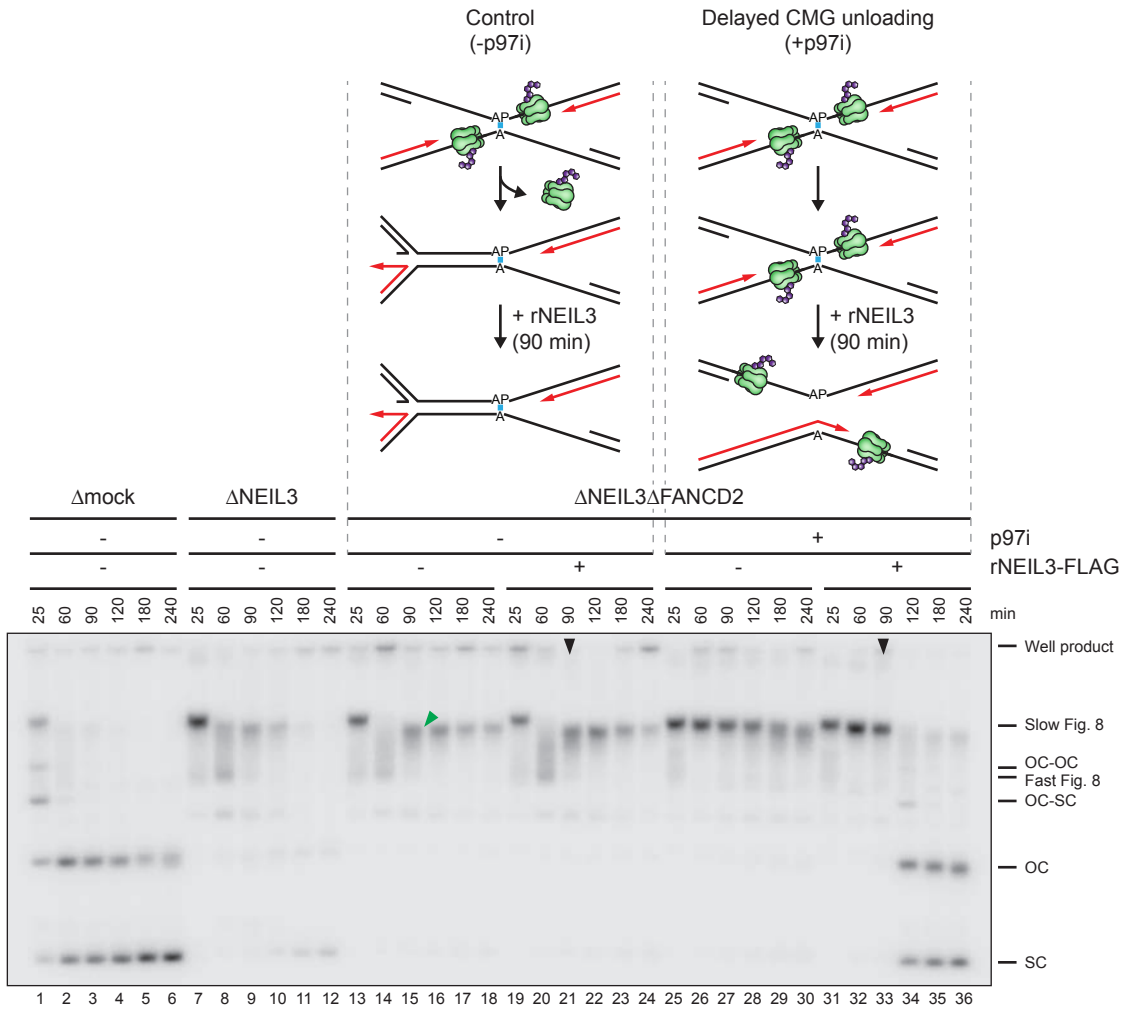
122 **d and g**, The extracts used in the replication reactions shown in Fig. 3, a (**d**) and c (**g**), were blotted
123 for TRAIP. Non-specifically detected proteins are marked with asterisks. The lack of non-specific
124 bands in **d** may be due to shorter incubation with the TRAIP antibody

125 **e**, pICL^{AP} was replicated with NEIL3-depleted extract supplemented with rNEIL3^{WT} or
126 rNEIL3^{K60A}, p97i, and Culi, as indicated, and analyzed as in Fig. 1b. OC, open circular; SC,
127 supercoiled.

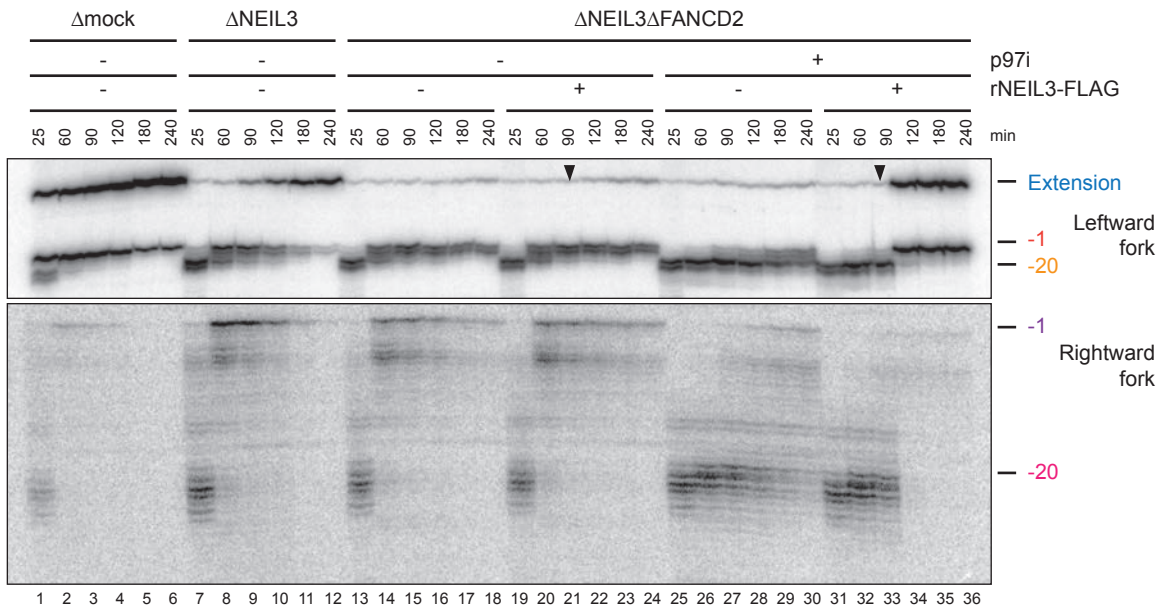
128 **f**, Analysis of proteins associated with pICL^{AP} during replication with NEIL3-depleted extract
129 supplemented with rNEIL3^{WT} or rNEIL3^{K60A}, p97i, and Culi. At the indicated times after
130 replication initiation, chromatin was recovered and blotted for the indicated proteins. Consistent
131 with NEIL3 dissociating rapidly after unhooking, catalytically inactive rNEIL3 (rNEIL3^{K60A}; **e**),
132 was recovered more efficiently with pICL^{AP} than rNEIL3^{WT}.

Extended Data Fig. 6

a



b



133 **Extended Data Fig. 6 | ICL repair by NEIL3 requires CMG association with chromatin**

134 If NEIL3 activity is coupled to ubiquitylated CMG, NEIL3 should only function before CMG has
135 been unloaded. To test this prediction, we depleted egg extracts of NEIL3 and FANCD2 to block
136 all unhooking events. At a late timepoint, we added back rNEIL3 to extract where CMG had
137 previously been allowed to unload (-p97i), or extract where CMG unloading was prevented
138 (+p97i). Our model predicts that rNEIL3 should function only in the latter setting.

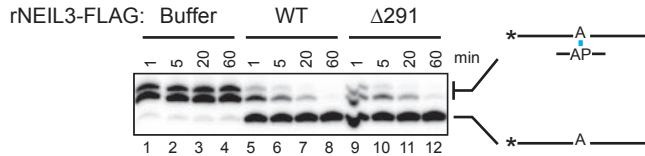
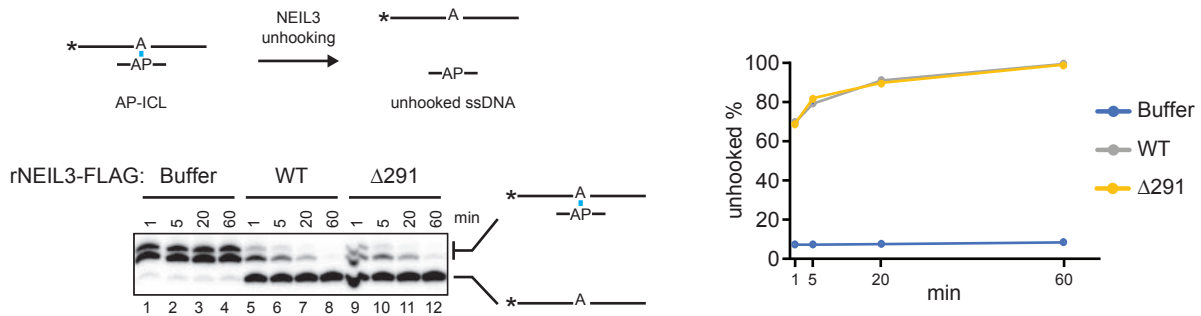
139 **a**, Top, schematic illustrating late addition of rNEIL3 to NEIL3- and FANCD2-depleted egg
140 extracts in the absence (left) or presence (right) of p97i. Bottom, replication of pICL^{AP} in mock-,
141 NEIL3-, or NEIL3- and FANCD2- depleted extracts in the presence of [α -³²P]dATP. Extracts were
142 supplemented with p97i as indicated and rNEIL3 was added at 90 min as indicated (black
143 arrowheads). Replication intermediates were resolved and visualized as in Fig. 1b. Depletion of
144 NEIL3 and FANCD2 blocked all unhooking of the AP-ICL, resulting in an accumulation of
145 reversed forks (lane 15, green arrowhead). Addition of rNEIL3 at 90 min. in the absence of p97i
146 (after CMG unloading) failed to induce unhooking, based on the persistence of the reversed forks
147 (lanes 21-24). In contrast, when CMG unloading was prevented with p97i (lanes 25-30; note the
148 persistence of slow Figure 8 intermediates), late rNEIL3 addition led to efficient ICL unhooking,
149 as seen from the rapid conversion of slow Figure 8s to open circular and supercoiled species (lanes
150 34-36).

151 **b**, To confirm the presence or absence CMG at the AP-ICL, DNA was recovered from the reactions
152 described in **a** and subjected to nascent strand analysis as in Extended Data Fig. 2e. Top, extension
153 products and nascent strands of the leftward fork. Bottom, nascent strands of the rightward fork.
154 Black arrowheads, rNEIL3 addition. Depletion of NEIL3 and FANCD2 did not affect loss of the
155 CMG footprint at -20 and caused persistence of nascent DNA strands at -1 (lanes 13-24), indicative

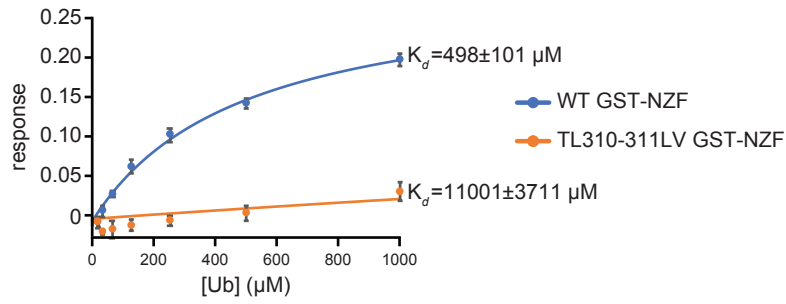
156 of failure to unhook the ICL. Late addition of NEIL3 failed to stimulate further nascent strand
157 extension (lanes 21-24), indicating that unhooking did not occur. Treatment with p97i caused
158 persistence of the CMG footprint at -20 (lanes 25-30), consistent with a retention of CMG at the
159 ICL, and late addition of NEIL3 stimulated formation of full-length nascent strand extension
160 products (lanes 34-36), indicative of efficient unhooking. Taken together, the data in **a** and **b**
161 strongly suggest that NEIL3 activity is coupled to the presence of CMG at the site of the ICL,
162 although we cannot rule out that NEIL3 activity is suppressed by downstream events, such as fork
163 reversal, that depend on CMG unloading.

Extended Data Fig. 7

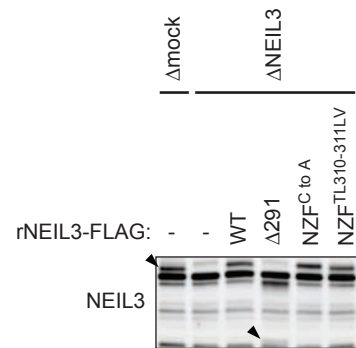
a



b



c



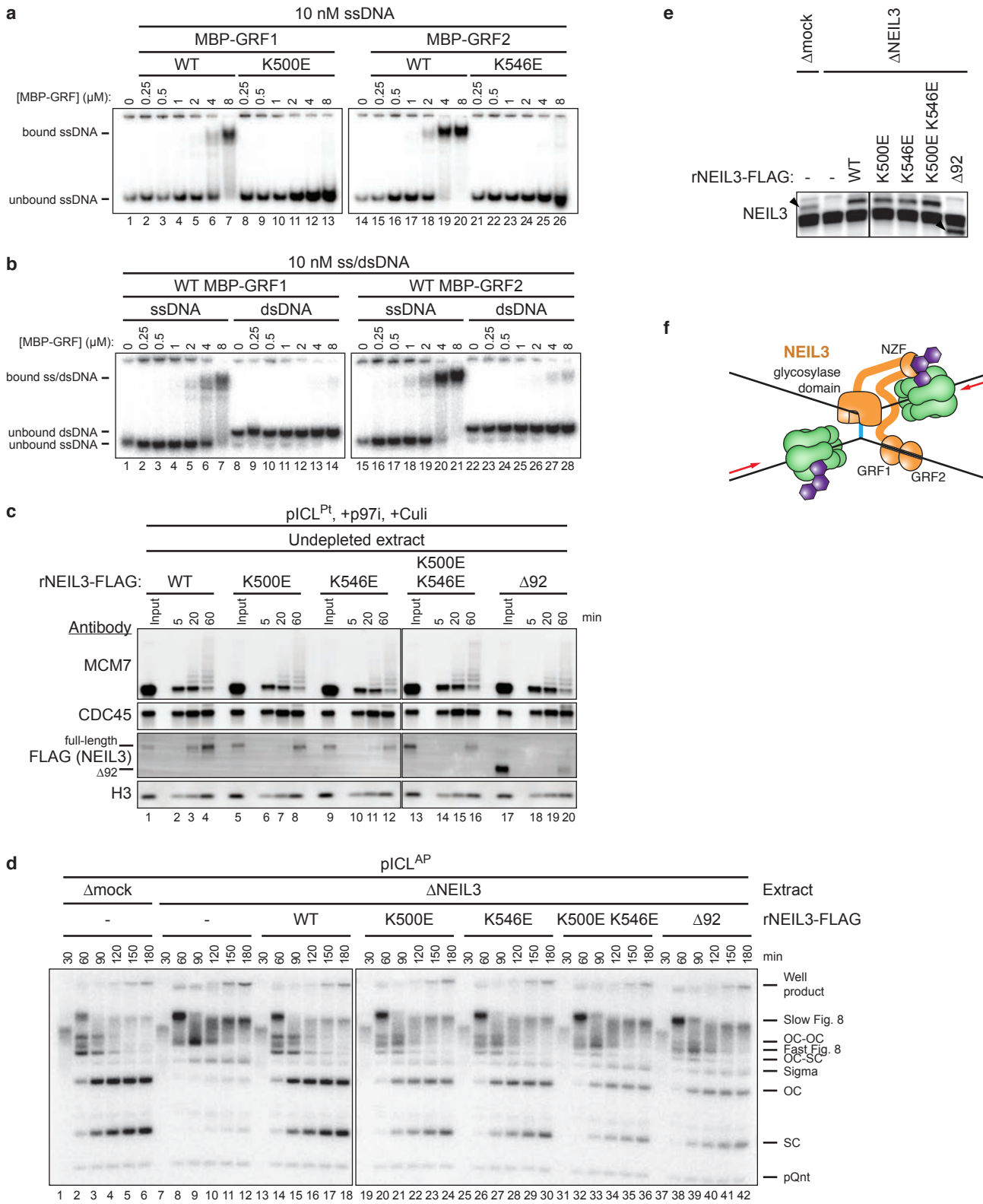
164 **Extended Data Fig. 7 | The NZF domain of NEIL3 contributes to ubiquitin binding but not**
165 **catalysis**

166 **a**, Left, to determine whether rNEIL3^{Δ291} is catalytically active, a model AP-ICL substrate
167 comprising a synthetic 5'-radiolabeled 24mer oligonucleotide cross-linked to a ~3mer was mixed
168 with rNEIL3^{Δ291} or rNEIL3^{WT}. Cross-linked and unhooked species were resolved by denaturing
169 polyacrylamide gel electrophoresis and visualized by autoradiography. Asterisks indicate the ³²P
170 radiolabel. Note that the cross-linked species migrates as a doublet due to heterogeneity in the
171 bottom strand following RNase digestion (see Methods for details). Right, quantification of
172 unhooking. Equivalent results were obtained in three independent experiments, which show that
173 rNEIL3^{Δ291} retains full activity.

174 **b**, Interaction of the NEIL3 NPL4-type zinc finger (NZF; residues 300 to 328) with ubiquitin.
175 GST-NEIL3 NZF fusion protein (WT or TL, LV substituted) was immobilized on a biosensor tip
176 and monoubiquitin binding was measured by biolayer interferometry (BLI). The ubiquitin binding
177 response was corrected for non-specific binding to GST and plotted as a function of ubiquitin
178 concentration. Error bars represent standard error of the mean from three independent experiments.

179 **c**, Mock- and NEIL3-depleted extracts supplemented with wild-type or substituted rNEIL3, used
180 in the replication reactions shown in Fig. 3e, were blotted for NEIL3. Black arrowheads, NEIL3-
181 specific bands. rNEIL3^{Δ291} is not efficiently detected by the NEIL3-specific primary antibody.

Extended Data Fig. 8



182 **Extended Data Fig. 8 | The GRF domains of NEIL3 mediate interactions with ssDNA at the**
183 **replication fork**

184 **a and b**, To test whether the two GRF zinc fingers in NEIL3 interact with ssDNA, we expressed
185 each individually and performed electrophoretic mobility shift assays. rMBP-NEIL3 GRF zinc
186 finger fusion proteins (wild-type or substituted) were incubated with 5'-radiolabeled 25-mer
187 ssDNA or dsDNA. Bound and unbound DNAs were resolved by native polyacrylamide gel
188 electrophoresis and visualized by autoradiography. This analysis reveals that both GRF domains
189 bind specifically to ssDNA.

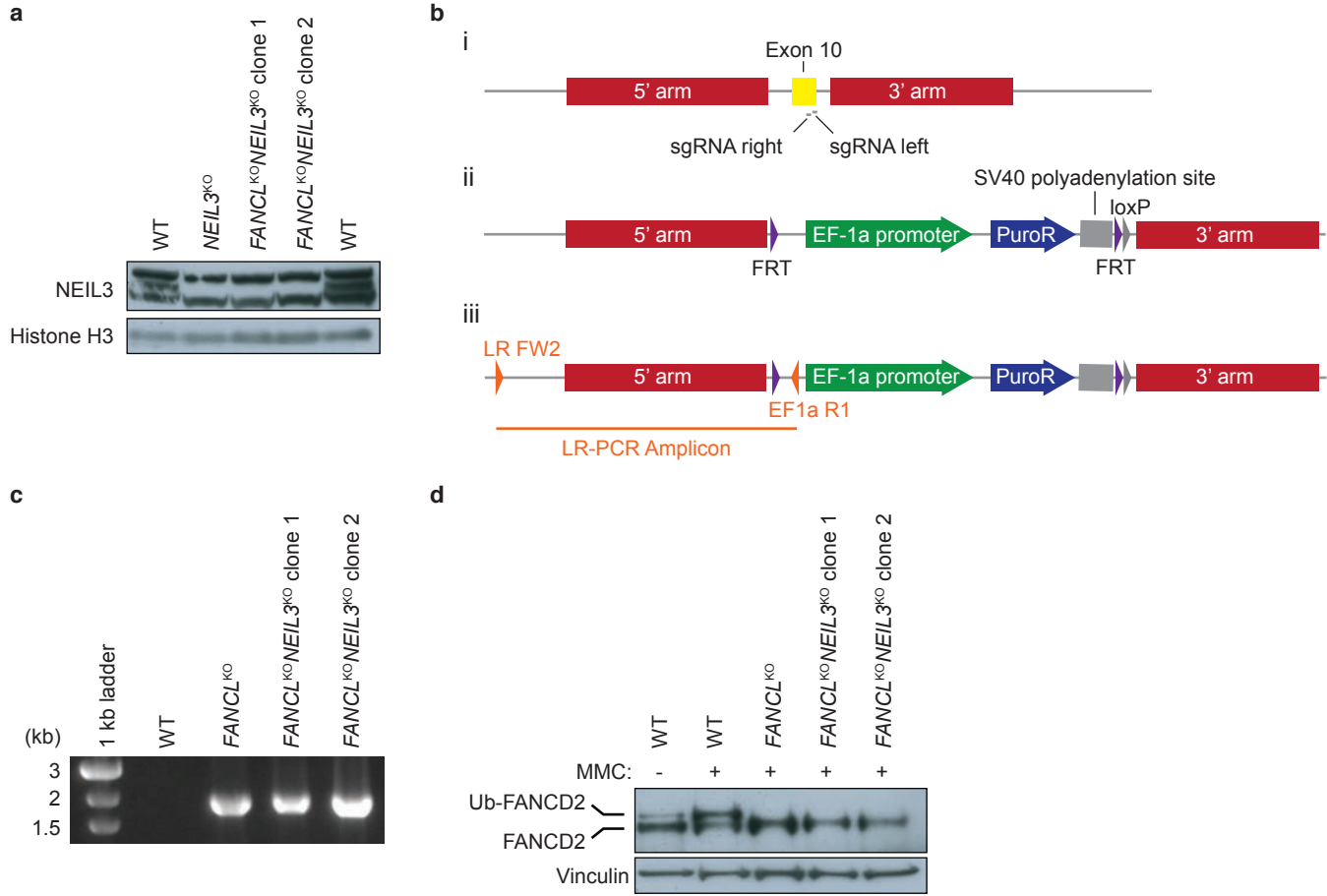
190 **c**, Analysis of proteins associated with pICL^{Pt} during replication in the presence of p97i and Culi.
191 Extracts were supplemented with wild-type or substituted rNEIL3. At different times, chromatin
192 was recovered and blotted for the indicated proteins. The individual GRF substitutions modestly
193 affected recovery of rNEIL3 upon pICL pull-down while combination of the substitutions or
194 deletion of both GRF zinc fingers strongly reduced rNEIL3 recovery, indicating that interactions
195 mediated by the GRF zinc fingers promote recruitment of NEIL3 to an ICL.

196 **d**, pICL^{AP} was replicated in mock- or NEIL3-depleted extracts supplemented with wild-type or
197 mutated NEIL3 as indicated and analyzed as in Fig. 1b. pQnt, undamaged control plasmid.
198 Relative to rNEIL3^{WT}, rNEIL3 with substitutions in either GRF zinc finger that abolish ssDNA
199 binding (K500E and K546E) exhibited modest defects in pICL^{AP} unhooking that were exacerbated
200 when the substitutions were combined, indicating that interactions between the GRF zinc fingers
201 and ssDNA contribute to ICL repair.

202 **e**, Mock- and NEIL3-depleted extracts supplemented with wild-type or substituted rNEIL3, used
203 in the replication reactions shown in **d**, were blotted for NEIL3.

204 **f**, Model for recruitment of NEIL3 to chromatin by zinc finger-mediated interactions. Upon
205 replication fork convergence at an ICL, TRAIP-dependent CMG ubiquitylation recruits NEIL3
206 through direct interactions between NEIL3's NZF domain and ubiquitin. Association of NEIL3
207 with chromatin is further enhanced by interactions between the tandem GRF zinc fingers and
208 single stranded DNA, possibly on the lagging strand template.

Extended Data Fig. 9



209 **Extended Data Fig. 9 | CRISPR targeting and validation of HAP1 cells**

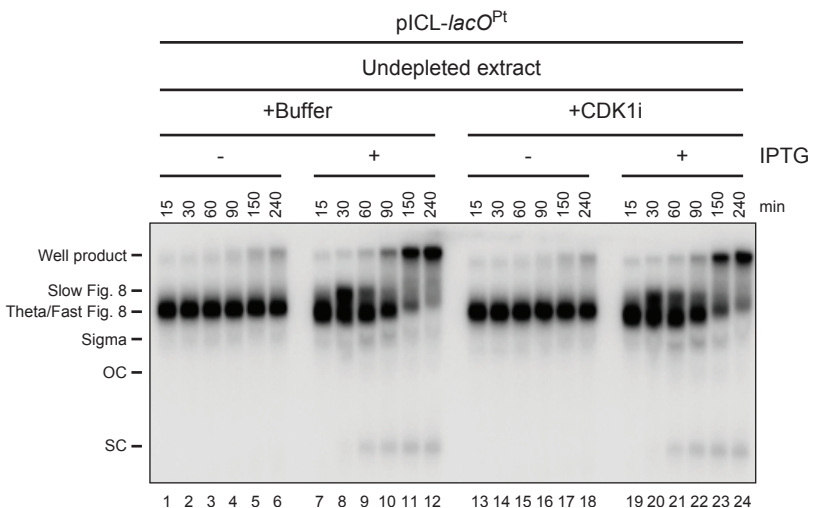
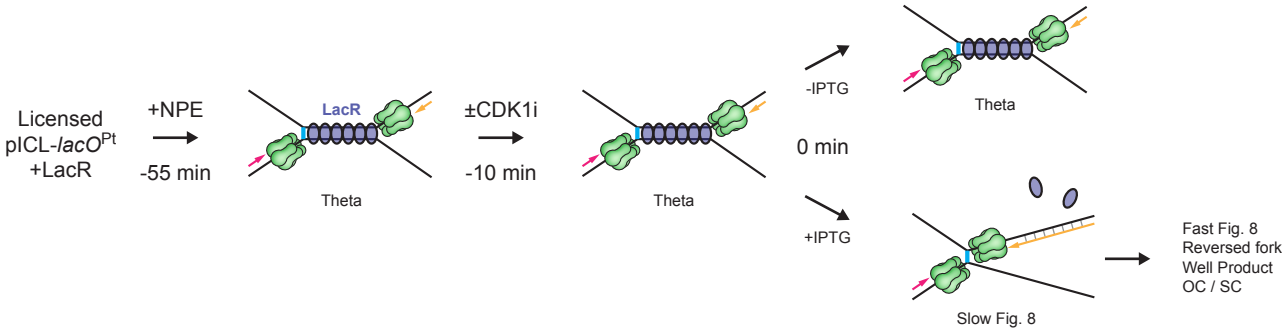
210 **a**, Immunoblot analysis of NEIL3 expression in wild-type, *NEIL3*, and *FANCL/NEIL3* knockout
211 HAP1 cell lines. Histone H3 was detected as a loading control.

212 **b**, Schematic of *FANCL* CRISPR targeting. (i) Human *FANCL* exon 10, sgRNA binding sites, and
213 homology arm targets, (ii) *FANCL*-Puro targeting construct with homology arms flanking exon
214 10, (iii) Targeted *FANCL* allele with integrated puromycin resistance cassette.

215 **c**, Detection of the integrated puromycin resistance cassette in HAP1 cells by *FANCL* long-range
216 PCR.

217 **d**, Analysis of FANCD2 ubiquitylation in mitomycin C (MMC)-treated wild-type, *FANCL*, and
218 *FANCL/NEIL3* knockout HAP1 cell lines to confirm *FANCL* knockout. Vinculin was detected as
219 a loading control. FANCL is the catalytic subunit of the FA core complex, which ubiquitylates
220 FANCD2.

Extended Data Fig. 10



221 **Extended Data Fig. 10 | ICL repair does not require M-CDK**

222 In interphase egg extracts, TRAIIP travels with DNA replication forks but ubiquitylates CMGs
223 only when forks converge. In the presence of mitotic cyclin-dependent kinase (M-CDK), TRAIIP
224 is activated in the absence of fork convergence (Deng et al., *submitted*). We therefore wanted to
225 know whether TRAIIP-dependent CMG unloading in interphase egg extract depends on residual
226 M-CDK activity. Top, the reaction scheme. Replication of pICL-*lacO*^{Pt} with a pre-assembled LacR
227 array was initiated at -55 min. Forty-five min after initiation (-10 min), reactions were
228 supplemented with buffer or the CDK1 inhibitor RO-3306 (CDK1i) and allowed to incubate for
229 an additional 10 min. The LacR array was then released with addition of IPTG to trigger fork
230 convergence and ICL repair (0 min). In a control, we added buffer instead of IPTG to retain the
231 LacR array. CDK1i was added late to avoid inhibition of replication initiation. Bottom, at the
232 indicated times after IPTG addition, samples were collected and analyzed as in Fig. 1B. Fork
233 stalling at the boundaries of the LacR array leads to a theta structure. The conversion of theta to
234 slow Figure 8, fast Figure 8 (co-migrating with theta), and well product in the presence of CDK1i
235 implies that M-CDK is not required for CMG unloading or ICL repair. This demonstrates that
236 TRAIIP activation at ICLs does not depend on residual M-CDK activity. Therefore, TRAIIP
237 activation at converged forks and in mitosis are mechanistically distinct.

238

239 **References:**

- 240 40 Walter, J., Sun, L. & Newport, J. Regulated chromosomal DNA replication in the
241 absence of a nucleus. *Mol Cell* **1**, 519-529 (1998).
- 242 41 Klein Douwel, D. *et al.* XPF-ERCC1 acts in Unhooking DNA interstrand crosslinks in
243 cooperation with FANCD2 and FANCP/SLX4. *Mol Cell* **54**, 460-471,
244 doi:10.1016/j.molcel.2014.03.015 (2014).
- 245 42 Fu, Y. V. *et al.* Selective Bypass of a Lagging Strand Roadblock by the Eukaryotic
246 Replicative DNA Helicase. *Cell* **146**, 931-941, doi:10.1016/j.cell.2011.07.045 (2011).

Supplementary Table 1 | Oligonucleotide Sequences**Oligonucleotides for preparation of pICLs**

Name	Sequence (Cross-linked positions are indicated in bold)
Pt_Top	CCCTCTTCC GG CTCTTCTTTTC
Pt_Bottom	GCACGAAAGAAGAGCGGAAG
AP_Top	CCCTCTTCC GdUT CTTTTC
AP_Bottom	GCACGAAAGAAGAGCGGAAG

Oligonucleotides for preparation of AP-ICL glycosylase assay substrates

Name	Sequence (Cross-linked positions are indicated in bold)
AP_assay_A	GCCATAGTAAGA A AGAGCCGAATGC
AP_assay_B	rGrCrArUrUrCrGrGrCrUC dUT rCrUrArCrUrArUrGrGrC

Oligonucleotides for preparation of EMSA assay substrates

Name	Sequence
EMSA_Top	AGACCGTGCCAGCCTAAATTTCAAT
EMSA_Bottom	ATTGAAATTTAGGCTGGCACGGTCT

Primer for preparation of Sequencing Ladder

Name	Sequence
pICL_Seq	CATGTTTTACTAGCCAGATTTTTCTCCTCTCCTG

Primers for preparation of Expression Vectors

Name	Sequence
NEIL3_291_A	GCGCGCGGAATTCACCATGGTGGAGGGTCCGGGCTG
NEIL3_291_B	CCAGCCCTCGAGCGTCTACTTGTGTCATCGTCTTTGTAGTCCCATCCAATAAGGCTATT
NEIL3_NZF_A	CTGGAAGTTCTGTTCCAGGG
NEIL3_NZF_B	TCACCGAAACGCGCGAGGCAGATCGTCAGTCAGTCACGATCTATGGTCTCAGAGTAAGAC
GST_A	ATCGTGACTGACTGACGATC
GST_B	CCCAGTGCTCTTCTTTGGGCCCTGGAACAGAACTTCCAGATCCGATTTTGGAGGATGGT
GRFZF1_A	ACTGGTAACCCACAGTGCAG
GRFZF1_B	TCACCGAAACGCGCGAGGCAGATCGTCAGTCAGTCACGAT
GRFZF2_A	TTGCATTTCCATTCTGCAA
GRFZF2_B	TCACCGAAACGCGCGAGGCAGATCGTCAGTCAGTCACGAT
MBP_A	ATGGGTTCTTCTCACCATCA
MBP_B	CACATGGAACATTGTGTGCACTGCACTGTGGTTACCACT
MBP_C	CAATACACCGTTTCCCATGGTTGCAGAATGGGAAATGCAA
pGEX_A	ATCGTGACTGACTGACGATC
pGEX_B	TAGAAGAACCATGGTGATGGTGATGGTGAGAAGAACCATGAATACTGTTTCCTGTGTGA
TRAI_P_A	ATTAGTACTGGATCCATGCCATACGCGCCTACTGTACG
TRAI_P_B	TCGTAGTAATGGATCCTTATTTCAAGAAGTCTTCGAGCCTGGGCTGG
R18C_A	ACACGTATTGTGCAAGAAGTCCGAGCAAATCGTAC
R18C_B	GATGTGGCCGCGATTACCTGTGGGC
PIP_A	GTTGGCAAGTGAGGAAGTACAAGCTGTG
PIP_B	TAAGGATCCGAGCTCCTCGAGTAATAAGCTTG

CRISPR Guide Sequences

Name	Sequence
FANCL_left	CCTAATGCAATTCTGCGTGCTGT
FANCL_right	TTTTTCTGGCTCAAGTACCCAGG

Primers for PCR Clonal Analysis

Name	Sequence
FANCL_LR_FW2	TGTCTACCCCTAAGTTCGTTGA
EF1a_R1	GCGATCTCTGGGTTCTACGTTAGTG